

RECORD 2020/3

# THE GEODYNAMIC CONTEXT OF ARCHEAN VOLCANISM IN THE WESTERN YILGARN CRATON

by  
I Koutsoubis



Government of **Western Australia**  
Department of Mines, Industry Regulation  
and Safety



THE UNIVERSITY OF  
**SYDNEY**

Geological Survey of  
Western Australia





Government of **Western Australia**  
Department of **Mines, Industry Regulation and Safety**

RECORD 2020/3

# THE GEODYNAMIC CONTEXT OF ARCHEAN VOLCANISM IN THE WESTERN YILGARN CRATON

by  
I Koutsoubis  
The University of Sydney

PERTH 2020



**Geological Survey of  
Western Australia**

**MINISTER FOR MINES AND PETROLEUM**  
**Hon Bill Johnston MLA**

**DIRECTOR GENERAL, DEPARTMENT OF MINES, INDUSTRY REGULATION AND SAFETY**  
**David Smith**

**EXECUTIVE DIRECTOR, GEOLOGICAL SURVEY AND RESOURCE STRATEGY**  
**Jeff Haworth**

**REFERENCE**

**The recommended reference for this publication is:**

Koutsoumbis, I 2020, The geodynamic context of Archean volcanism in the western Yilgarn Craton: Geological Survey of Western Australia, Record 2020/3, 114p.

**ISBN** 978-1-74168-882-5

**ISSN** 2204-4345

Grid references in this publication refer to the Geocentric Datum of Australia 1994 (GDA94). Locations mentioned in the text are referenced using Map Grid Australia (MGA) coordinates, Zone 50. All locations are quoted to at least the nearest 100 m.

**About this publication**

This Record is an Honours thesis researched, written and compiled as part of an ongoing collaborative project between Geological Survey and Resource Strategy (GSRS) and the University of Sydney, New South Wales. Although GSRS has provided field support for this project, the scientific content of the Record, and the drafting of figures, was the responsibility of the author. No editing has been undertaken by GSRS.



**Disclaimer**

This product was produced using information from various sources. The Department of Mines, Industry Regulation and Safety (DMIRS) and the State cannot guarantee the accuracy, currency or completeness of the information. Neither the department nor the State of Western Australia nor any employee or agent of the department shall be responsible or liable for any loss, damage or injury arising from the use of or reliance on any information, data or advice (including incomplete, out of date, incorrect, inaccurate or misleading information, data or advice) expressed or implied in, or coming from, this publication or incorporated into it by reference, by any person whatsoever.

**Published 2020 by the Geological Survey of Western Australia**

This Record is published in digital format (PDF) and is available online at <[www.dmp.wa.gov.au/GSWApublications](http://www.dmp.wa.gov.au/GSWApublications)>.



© State of Western Australia (Department of Mines, Industry Regulation and Safety) 2020

With the exception of the Western Australian Coat of Arms and other logos, and where otherwise noted, these data are provided under a Creative Commons Attribution 4.0 International Licence. (<http://creativecommons.org/licenses/by/4.0/legalcode>)

**Further details of geoscience products are available from:**

Information Centre  
Department of Mines, Industry Regulation and Safety  
100 Plain Street  
EAST PERTH WESTERN AUSTRALIA 6004  
Telephone: +61 8 9222 3459 Facsimile: +61 8 9222 3444  
[www.dmirs.wa.gov.au/GSWApublications](http://www.dmirs.wa.gov.au/GSWApublications)

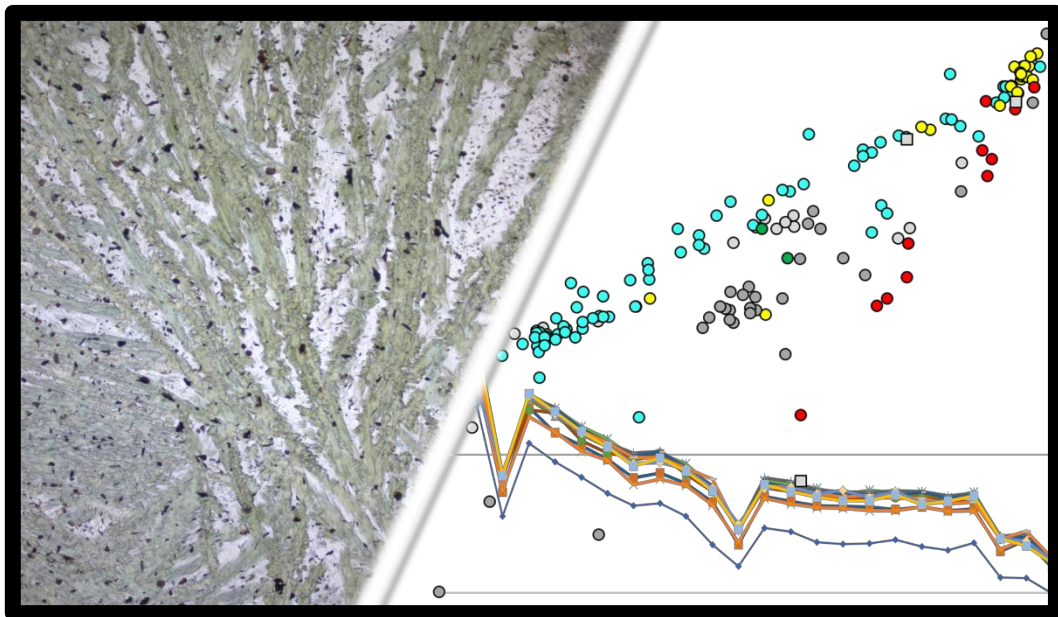
**Cover image:** Packing up the campsite in a claypan about 5 km south of Minilya in the southern Pilbara (photo by Olga Blay)

# The Geodynamic Context of Archean Volcanism in the Western Yilgarn Craton

Irene Koutsoumbis

Supervisor: A/Prof. Derek Wyman

Thesis submitted in partial fulfilment of the requirements for the degree of Bachelor of  
Liberal Arts and Science (Honours), Geology and Geophysics



The University of Sydney  
Faculty of Science  
School of Geosciences

Submitted on: 25/10/2019

Word Count: 18,004

## Acknowledgements

Firstly, I would like to thank my supervisor, Derek Wyman, for all the support, knowledge and guidance given to me throughout the year. All the enjoyable discussions and being given the opportunity to be a part of such an exciting research project was a great learning experience.

I would also like to thank the Australian Research Council (ARC) for their funding of this project within the larger grant (LP130100722). The Geological Survey of Western Australia is also thanked for the use of the whole rock data from the WACHEM database, and in particular, Jack Lowrey is also thanked for his correspondences during the year.

I would like to thank Owen for all his support and understanding throughout the year and helping me stay inspired and motivated to do my personal best. I would also like to thank Quinn, Joe and Cian for all the good times, laughs and support during this year. Lastly, I would like to thank Sabin Zahirovic for all his support and encouragement during the year.

## Abstract

Studies of Australia's Yilgarn Craton have disproportionately focussed on the resource-rich Eastern Goldfields Superterrane. The few studies of the western Yilgarn have, until recently, overwhelmingly favoured a Mesoarchean to Neoproterozoic mantle plume scenario. Increasingly, however, new field studies from the northwest Yilgarn report subduction-style magmatism. The present study investigates similarly aged volcanic sequences further south in the craton to determine the extent of the subduction-style rocks and critically re-evaluate the standard plume model. Subduction-style rocks are confirmed in the south through the presence of boninite rocks. Comparisons with the Abitibi greenstone belt plume-arc low-Ti rocks, and the younger (< 2 Ma) Hunter Ridge pre-arc boninites, shows a closer resemblance to the latter, i.e., implying an arc setting.

All spinifex textures reported are pyroxene spinifex or acicular pyroxene found in boninites or Siliceous High Magnesium Basalts or High Magnesium Andesites. Previously reported komatiites were, in all cases, misidentified due to their traditional association with spinifex texture. Some basalts and andesites, or shallow intrusive counterparts, display negative Zr-Hf anomalies that are difficult to generate via crustal contamination. Trace elements display fluid- and sediment-derived metasomatic trends consistent with a subduction setting. There is no evidence of progressive crustal contamination within the data sets for study localities, indicating that the subduction-style signatures are primary magmatic features and not the result of crustal contamination. With these findings, we determine that subduction plays a key role in the Mesoarchean to Neoproterozoic evolution of the Yilgarn craton whereas there is no strong evidence for mantle plume processes at this time in the Western Yilgarn craton.

# Table of Contents

<b>Acknowledgements</b> .....	i
<b>Abstract</b> .....	ii
<b>Table of Figures</b> .....	v
<b>Chapter 1 Introduction</b> .....	1
<b>Objectives/Aims</b> .....	3
<b>Chapter 2 Regional Geology and Previous Work</b> .....	4
<b>Tectonic Subdivisions</b> .....	4
<b>Current Yilgarn Terrane Descriptors</b> .....	6
<b>Plume and Subduction Rock Types</b> .....	8
<b>Granitoids</b> .....	8
<b>Komatiites</b> .....	9
<b>Boninites</b> .....	11
<b>Subduction and Plume Models</b> .....	13
<b>Plume Models</b> .....	13
<b>Subduction Models</b> .....	17
<b>Western Yilgarn</b> .....	18
<b>Murchison Domain Stratigraphic Models</b> .....	20
<b>Norie Group</b> .....	23
<b>Polelle Group</b> .....	23
<b>New Rock Type Classifications - Pearce and Reagan (2019)</b> .....	27
<b>Rock Type Descriptions for the Pearce and Reagan Classification Scheme</b> .....	30
<b>Study Areas</b> .....	33
<b>Mt. Mulgine</b> .....	33
<b>Yeoh Hills</b> .....	33
<b>Warriedar</b> .....	34
<b>Yalgoo</b> .....	34
<b>Chapter 3 Analytical Methods</b> .....	35
<b>Petrography</b> .....	35
<b>Geochemistry</b> .....	35
<b>Boninite Discrimination Plots</b> .....	36
<b>Geochemical Variation Diagrams</b> .....	37
<b>Primitive Mantle Plots</b> .....	37
<b>Chapter 4 Petrography Results</b> .....	39
<b>Mt. Mulgine</b> .....	40

Yeoh Hills .....	43
Warriedar.....	46
Yalgoo .....	49
<b>Chapter 5 Whole Rock Geochemical Results.....</b>	<b>53</b>
<b>Boninite Discrimination Plots .....</b>	<b>54</b>
<b>Geochemical Variation Diagrams .....</b>	<b>57</b>
Major Elements .....	58
Trace Elements .....	62
<b>Normalized Primitive Mantle Plots .....</b>	<b>65</b>
Mt. Mulgine .....	65
Yeoh Hills .....	66
Warriedar.....	66
Yalgoo .....	68
<b>Chapter 6 Discussion .....</b>	<b>71</b>
<b>Assessing Crustal Contamination and Magma Mixing.....</b>	<b>72</b>
<b>Geological Map Implications .....</b>	<b>78</b>
<b>Depositional Environment .....</b>	<b>78</b>
<b>Komatiites.....</b>	<b>79</b>
<b>Boninites.....</b>	<b>80</b>
<b>Regional Correlations of the Meekatharra Formation .....</b>	<b>81</b>
<b>Geodynamic Significance .....</b>	<b>83</b>
<b>Future Study Recommendations .....</b>	<b>85</b>
<b>Chapter 7 Conclusions .....</b>	<b>87</b>
<b>References .....</b>	<b>89</b>

## Table of Figures

<b>Figure 1.1:</b> Schematic of the Yilgarn craton with tectonostratigraphic subdivisions defined by bold and broken lines. Study areas are represented by coloured circles. Adapted from Martin et al. (2015), Witt et al. (2018) and Wyman (2019).....	3
<b>Figure 2.1:</b> Komatiite locations globally (in red and blue circles). Grey areas represent global exposed cratons with Archean ages. Proterozoic aged cratons are outlined in red and craton correlation to Pangea are represented in blue. Adapted from Pearson and Wittig (2008) and Arndt et al. (2008).....	10
<b>Figure 2.2:</b> Differences between <b>A)</b> Archean tectonics and <b>B)</b> modern tectonics incorporating long-lived style subduction. From Foley et al. (2003).....	13
<b>Figure 2.3:</b> Two periods of plume magmatism, <b>A)</b> deep mantle plume head rises at 2820-2790 Ma <b>B)</b> the next phase in plume magmatism at 2720-2675 Ma. From Van Kranendonk et al. (2013). YT= Youanmi Terrane; KT = Kalgoorlie Terrane; GT=Gindalbie Terrane; KNT = Kurnalpi Terrane, BT= Burtville Terrane; TTD = Tonalite-Trondhjemite-Dacite; CA = Calc-Alkaline magmas. ....	15
<b>Figure 2.4:</b> <b>A)</b> onset of extensions and rifting in the proto-craton at 2825-2815 Ma <b>B)</b> subduction between the Narryer Terrane and northwest Murchison Domain at ~2810 Ma <b>C)</b> convergence episodes at 2800-2740 . From Wyman and Kerrich (2012). ....	19
<b>Figure 2.5:</b> Stratigraphy of the Murchison Domain with the volcanism hiatus highlighted in red. Adapted from Van Kranendonk (2013) and Lowrey et al. (2019 in press). ....	22
<b>Figure 2.6:</b> Yalgoo geological map with samples from this study plotted with a red circle. From Ivanic et al. (2015) .....	25
<b>Figure 2.7:</b> Perenjori and Ninghan geological maps with samples from this study plotted with a red circle, where M = Mt. Mulgine, F = Fields Find East, Y = Yeoh Hills and W = Warriedar. From GSWA (1983) and Ivanic (2018) respectively. ....	26
<b>Figure 2.8:</b> <b>A)</b> IUGS scheme for high-Mg volcanic rocks - from Le Bas (2000). <b>B)</b> MgO vs SiO <sub>2</sub> plot from Pearce and Reagan (2019) <b>C)</b> MgO vs TiO <sub>2</sub> plot from Pearce and Reagan (2019) <b>D)</b> Ti8 vs Si8 plot from Pearce and Reagan (2019). ....	28
<b>Figure 2.9:</b> Archean and post-Archean boninite types in multiple settings including plume sourced boninites and subduction initiated boninites, from Pearce and Reagan (2019).....	30
<b>Figure 4.1:</b> Carbonate vein (centre) in sample FFE1 (cross polarized light).....	40
<b>Figure 4.2:</b> Spinifex texture of random dendritic pyroxenes replaced by amphibole in sample MG14A (plane polarized light).....	41
<b>Figure 4.3:</b> Pseudomorphs of cruciform to irregular polysynthetic twins of primary pyroxene replaced by subhedral amphibole in a fine-grained quartz-feldspar groundmass in sample MG11 (plane polarized light). The cross-type twins are typical of clinoenstatite in boninites (see text). ....	42
<b>Figure 4.4:</b> Secondary TiO <sub>2</sub> (leucoxene) in sample MG1. Left in plane polarized light and right in reflected light. ....	43
<b>Figure 4.5:</b> Variole forming a globular geometry in sample YH15 (plane polarized light). ....	44
<b>Figure 4.6:</b> Moderate shearing and deformational fabric in sample YH20 (left in plane polarized light, right in cross polarized light). ....	45
<b>Figure 4.7:</b> Alteration of a primary, euhedral, olivine to amphibole. The original crystal edges are best preserved on the upper right side of the crystal. Sample YH19C (plane polarized light). ....	46

<b>Figure 4.8:</b> Typical texture in the Warriedar area, with amphibole pseudomorphs of coarse primary pyroxenes (green) and a feldspathic groundmass (white). Sample WR5 is pictured in plane polarized light. ....	47
<b>Figure 4.9:</b> Altered olivine cumulate; olivine crystals have been altered to talc in sample FFE3 (plane polarized light). ....	48
<b>Figure 4.10:</b> Amphibole cleavage preserved by an oxide in sample WR10 (left in plane polarized light, right in reflected light). ....	49
<b>Figure 4.11:</b> Alteration rims from amphibole variably replacing zoned pyroxene crystals in sample WR9 (plane polarized light). ....	49
<b>Figure 4.12:</b> Left image shows inner and outer rims in an altered pyroxene in sample YL18 (cross polarized light). Right image shows a secondary hornblende crystal with a reaction rim of fine-grained silicates in sample YL18 (plane polarized light). ....	50
<b>Figure 4.13:</b> Fine bladed spinifex in sample YL8 (plane polarized light). ....	50
<b>Figure 4.14:</b> Filling in of spaces in a triangular shape in sample 225152 (plane polarized light). ....	51
<b>Figure 4.15:</b> Transition from cruciform texture (left) to a gabbroitic texture (right) in sample YL11 (plane polarized light). ....	52
<b>Figure 4.16:</b> Granophyric texture in a coarse-grained matrix in sample YL6 (cross polarized light). ....	52
<b>Figure 5.1:</b> MgO vs SiO <sub>2</sub> plot after Pearce and Reagan (2019). PB = picro-basalt, LSB = low-Si boninites, HSB = high-Si boninites, HMA = high-Mg andesites, BA = basaltic andesite, A = andesite, D = dacite. ....	55
<b>Figure 5.2:</b> MgO vs TiO <sub>2</sub> plot after Pearce and Reagan (2019). HMA = high-Mg andesites, BADR = basalt-andesite-dacite-rhyolite. ....	56
<b>Figure 5.3:</b> Ti <sub>8</sub> vs Si <sub>8</sub> plot after Pearce and Reagan (2019), refer to chapter 3 for Ti <sub>8</sub> and Si <sub>8</sub> derivations. BADR = basalt-andesite-dacite-rhyolite, SHMB = siliceous high-Mg basalts, LOTI = low-Ti basalts. ....	57
<b>Figure 5.4:</b> Harker variation plots for Yalgoo, Mt. Mulgine, Warriedar, Yeoh Hills, Gullewa and Weld Range. ....	60
<b>Figure 5.5:</b> Variation plots for Yalgoo, Mt. Mulgine, Warriedar, Yeoh Hills, Gullewa and Weld Range. ....	61
<b>Figure 5.6:</b> CaO vs MgO plot for Yalgoo, Mt. Mulgine, Warriedar, Yeoh Hills, Gullewa and Weld Range. ....	62
<b>Figure 5.7:</b> Compatible elements variation plots against Ni for Yalgoo, Mt. Mulgine, Warriedar, Yeoh Hills, Gullewa and Weld Range. ....	63
<b>Figure 5.8:</b> Incompatible element variation plots against Th, for Yalgoo, Mt. Mulgine, Warriedar, Yeoh Hills, Gullewa and Weld Range. ....	64
<b>Figure 5.9:</b> Normalised primitive mantle plot for Mt. Mulgine samples from this study. ....	65
<b>Figure 5.10:</b> Normalised primitive mantle plot for Yeoh Hills samples from this study. ....	66
<b>Figure 5.11:</b> Normalised primitive mantle plot for some Warriedar samples from this study. Samples show close associations in the HREE but are variable in LREE. ....	67
<b>Figure 5.12:</b> Normalised primitive mantle plot for some Warriedar samples from this study. Samples show 3 trends, an upper high-LREE trend, and moderate LREE trend and a lower sample, FFE1. ....	68
<b>Figure 5.13:</b> Normalised primitive mantle plot for high-LREE Yalgoo samples from this study. ....	69

<b>Figure 5.14:</b> Normalised primitive mantle plot for low-LREE Yalgoo samples from this study. ....	70
<b>Figure 6.1:</b> Th/Yb vs Nb/Yb plot after Pearce, 2008 and Smithies et al., 2018, for <b>A)</b> the Polelle Group <b>B)</b> the Norie Group. Most samples define parallel trends to the mantle array, with Polelle samples showing a strong trend in Yalgoo and Mt. Mulgine sample areas. Samples do not enter the Yilgarn TTG field. A horizontal trend is defined in A composed of Yalgoo and Yeoh Hills samples. ....	73
<b>Figure 6.2:</b> Ba/Th plot for <b>A)</b> the Polelle Group <b>B)</b> the Norie Group. Vertical trends indicate a fluid source, and horizontal trends denote a sediment melt source. Contamination trends are defined by the grey arrow. ....	76
<b>Figure 6.3:</b> Normalised primitive mantle plot showing similarities of the Warriedar Intrusive Suite between the north Mt. Magnet samples (Wyman, 2019; Mmd samples) and the south Warriedar area samples from this study (WR samples) ....	77
<b>Figure 6.4:</b> Zr vs Th plots for <b>A)</b> the Polelle Group <b>B)</b> the Norie Group. Trends indicate the amount of magma systems that are representative of the sample set (Wyman, 2019), where a minimum of 3 trends are identified. ....	81
<b>Figure 6.5:</b> Normalised primitive mantle plot for low-LREE samples from Yalgoo (YL16, YL17), Gullewa (225119) and Weld Range (183341, 190940). ....	83
<b>Figure 6.6:</b> Normalised primitive mantle plot for high-LREE samples from Yalgoo (YL8, YL11), Gullewa (DF26-256, DF31-124) and Weld Range (81634, 81635). ....	83
<b>Figure 6.7:</b> Normalised primitive mantle plot for Mt. Mulgine area boninites (MG samples) and Abitibi greenstone belt LOTI basalts (KC samples). ....	84
<b>Figure 6.8:</b> Mt. Mulgine area, Meekatharra Formation boninites (MG samples) compared to the Hunter Ridge high-Ca boninites (D4-14 and D6-17) from Patriat et al. (2019). ....	85

## Chapter 1 Introduction

The Yilgarn craton is one of Australia's most resource-rich geological provinces but research has disproportionately focussed on the Eastern Goldfields Superterrane (EGS) (Fig. 1.1). This is because the EGS is host to significant orogenic gold and komatiite nickel mineralisation as well as other base metal mineralization (Czarnota et al., 2010; Hollis et al., 2017; Moroni et al., 2017). Recent interest in the western Yilgarn (Van Kranendonk et al., 2013; Duuring et al., 2016), however, has generated new ideas that have implications for the early geodynamics of the entire craton (Wyman and Kerrich, 2012; Smithies et al., 2018; Wyman, 2019). This study continues the re-evaluation of the western Yilgarn with a focus on volcanic and sub-volcanic rock samples obtained from four areas within the southern part of the Murchison Domain, Youanmi Terrane.

The study of the Yilgarn Craton has been significant in the general development of global Archean geodynamic models, particularly those invoking mantle plume reworking of early cratons (Campbell and Hill, 1988; Hill et al., 1992). The Meso- to Neo-Archean was important in terms of crustal growth for early continents and is a key period for understanding komatiites (e.g., Barnes and Fiorentini, 2012) and hence, for Archean plume literature. Komatiites are a volcanic rock derived from the mantle that are mafic-ultramafic in composition. These are typically restricted to the Archean due to increased mantle plume source temperatures (Arndt et al., 2008). Komatiites are characterized chemically by compositions with  $> 18$  wt% MgO,  $< 50$  wt% SiO<sub>2</sub> and  $> 1000$  ppm Ni content. They typically show long acicular phenocrysts of olivine, termed 'spinfex' texture, created from rapid cooling of magma with a high thermal gradient.

The nature of geodynamics in the Archean has been a long-standing subject of debate where some consensus may be emerging due to an expansion of sample populations and the use of new analytical techniques (e.g., isotopic analyses of single zircons: Dhume et al., 2012). A gradual transition from thermal plume-driven processes to modern-style plate tectonics has been invoked with correlations of post-Archean subduction-style rocks to Archean boninites, andesites, dacites, etc. (Barley et al., 2008). Boninites are categorized as mafic extrusive rocks that are high in SiO<sub>2</sub> (> 52 wt%) and low in Ti (< 0.5 wt%) at MgO fractionation trends of 8 wt% (Pearce and Reagan, 2019). These boninites are thought to indicate subduction zones that occurred during the Archean (Pearce and Reagan, 2019). For the Yilgarn's cratonic evolution, subduction related models have been proposed in light of evidence for arc-style magmatism, plate convergence, and orogeny. However, models that incorporated subduction for the main explanation of cratonic evolution have previously been related to post-Archean accretion processes. These boundaries are now suggested to be late features of the craton (Smithies et al., 2018). This demonstrates the need for a diverse sample set in terms of location and composition. Studies regarding the stratigraphy of the Yilgarn have been published by the Geological Survey of Western Australia (GSWA) which allow for context into these geodynamic models. Both komatiites and boninites have been documented to be found in the Yilgarn, by the GSWA and other studies (Wyman and Kerrich, 2012; Wyman, 2019; Lowrey et al., 2019 in press).

This study will characterize ultramafic to intermediate volcanic rocks of the southern Murchison Domain, with a particular emphasis on distinguishing between komatiites or komatiitic basalts and boninites. It will, also consider evidence from all of the studied rock types in an attempt to establish an improved Yilgarn geodynamic model. Rock types can range from high-Mg andesites, siliceous high-Mg basalts, picrites and low-Ti basalts. Characterisation of these samples will provide additional data for the evolving geodynamic model of the craton.

## Objectives/Aims

This study is part of an Australian Research Council (ARC) Linkage grand-funded project aiming to clarify the distribution, origin and significance of boninite-like and associated rocks in the Murchison Domain (Fig. 1.1). This will be completed through petrographic analysis of each sample to understand magma histories with extensive reference to geochemical data. The results will be used to assess the GSWA's stratigraphical groups including formation and suite type, extracted from the Western Australia 1:100 000 geological map. These groups will then be compared to other global Archean and post Archean samples to improve on the 2.8 Ga tectonic model. Using this model, the mineralisation in the western Yilgarn can be given context which can assist in exploration field studies. Therefore, with the consideration of the western Yilgarn in models and theories regarding the development of the craton, the Yilgarn can be considered on a global scale and compared with other Archean cratons to understand early continent dynamics.

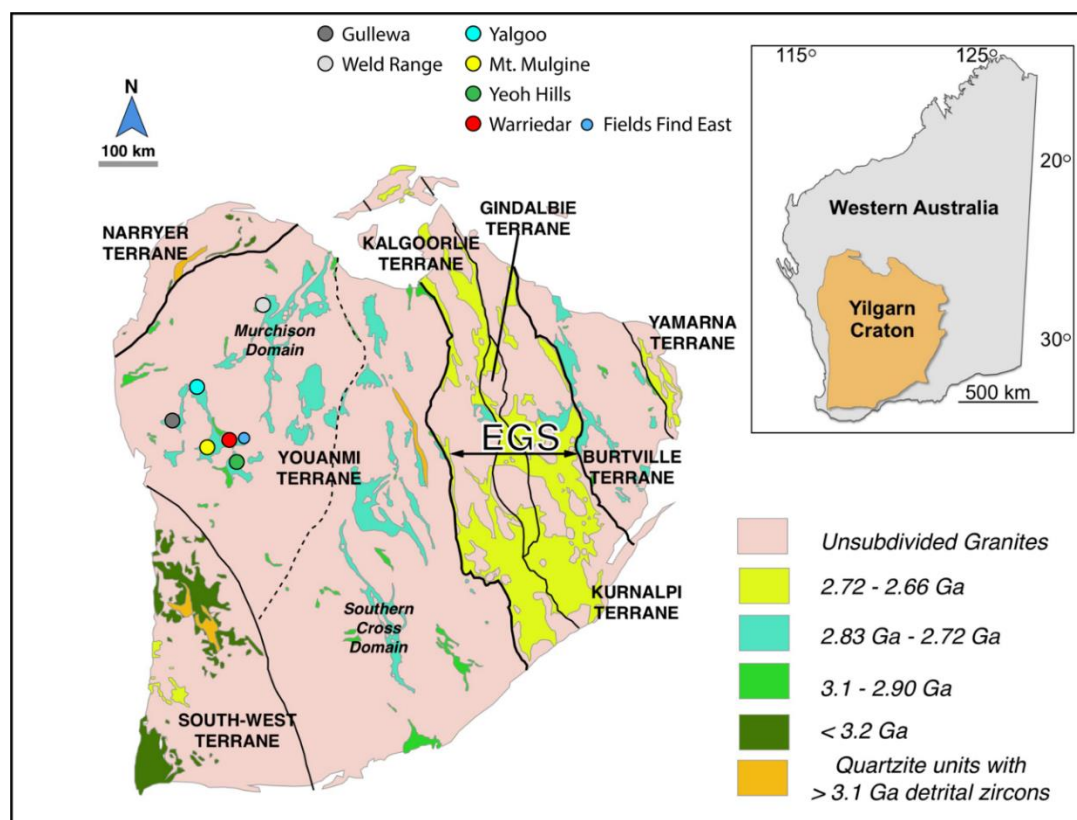


**Figure 1.1:** Schematic of the Yilgarn Craton with tectonostratigraphic subdivisions defined by bold and broken lines. Study areas are represented by coloured circles. Adapted from Martin et al. (2015), Witt et al. (2018) and Wyman (2019).

## Chapter 2 Regional Geology and Previous Work

The Yilgarn Craton is a stable piece of Archean crust that is composed of north-northwest striking greenstone belts interlayered with sediments and granitoids of varying ages as seen on Figure 1.1. Greenstone belts, in the study area, are composed of various metamorphosed basalts (siliceous high Mg basalt (SHMB) and low-Ti basalt (LOTI)), high magnesium andesites (HMA), boninites (low-Si boninites and HSB), dacite-rhyolites and ultramafic-mafic intrusive rock (peridotite, gabbro, dolerite, etc.). Additionally, regional faults and shear zones define the boundaries of tectonic subdivisions in the Yilgarn in a four-fold scheme: craton > superterrane > terrane > domain. These boundaries were conventionally thought to have developed early in the craton's history, displaying an accretionary origin of the craton. However, new theories have inferred that many of them are late features (see Smithies et al., 2018).

### Tectonic Subdivisions

The Yilgarn Craton has been subdivided into a number of superterranes, terranes, and domains as shown in Figure 1.1. Gee et al. (1981) described four major subdivisions of the Yilgarn Craton: The Eastern Goldfields, Southern Cross, the Murchison 'Provinces' and the Western Gneiss Terrain. These subdivisions were mainly hypothetical and were not based on discrete observed geological features, such as boundary faults. Other studies such as Myers (1990), Myers (1995), Swager (1997), and Barley et al. (2000), have revised this tectonostratigraphic scheme using further geochemistry and geochronology.

Myers (1990) proposed a model involving amalgamation of continental blocks associated with the current Yilgarn Craton. These features were then used to create the various boundaries associated with the subdivision of the craton. Gee et al. (1979) considered the Capricorn Orogen between the Pilbara and Yilgarn Cratons to lack

evidence of any subduction or plate tectonic processes. However, with the assessment of the cross section that is exposed at the western side of the orogen, Myers (1990) affirmed that the two cratons had distinct origins and that a continental collision took place. Another continental collision produced the Albany-Fraser orogen (1300 - 1100 Ma), which outlines the southern boundary of the craton. The Pinjarra orogen sets the boundary for the western side of the craton but is covered in approximately 10 – 15 km of sedimentary rocks dated to the Proterozoic. The Paterson orogen defines the northeast boundary of the craton (750 – 550 Ma), consisting of several thrusts that contain Early Proterozoic gneiss, volcanic and sedimentary (ca. 900 Ma) rocks.

Based on additional mapping, Myers (1995) improved on his original 1990 scheme and also proposed that the Yilgarn Craton was part of the Proterozoic Gondwana super continent before it dispersed. The variety of rock types in the Yilgarn (non-clastic and clastic sedimentary, granites, greenstones etc.), lead to the idea of accretion of the continental fragments colliding. These fragments could include back arc (basins/microcontinents) and volcanic arc material. Swager (1997) conducted a study focusing on the Southern Eastern Goldfields. The greenstones in this area are bounded by faults and are elongated. Komatiite volcanics (2710 – 2700 Ma) are present in the Eastern Goldfields Superterrane (EGS) as reported by Swager (1997). The study concluded that the terranes developed as coexisting, adjacent basins (Swager, 1997).

Cassidy et al. (2006) further subdivided the tectonostratigraphic terranes in the Yilgarn, distinguishing the boundaries between the 7 terranes (refer to Fig. 1.1). Age, geochemistry and other geological characteristics (e.g. sedimentary and magmatic) were considered when creating these boundaries. The terranes consist of older basement gneiss suites, sometimes only identified from xenocrystic zircons, overlain by younger granite-greenstone belts with meta-sedimentary rocks that were formed between 3050 to 2600 Ma (Cassidy et al., 2006). Another major change in the restructuring of the proposed terrane boundaries was introduced in this paper and it

included the region covered in the present study. The former northwest 'Murchison Terrane' was assigned to the current 'Murchison Domain' of the Youanmi Terrane, which extended further south. Some other proposed terranes, such as the Yamarna and redefined Burtville of the eastern Yilgarn also appear in recent tectonostratigraphic maps, denoting their distinctive volcanic facies, structural histories and the age and geochemistry of intermediate to silicic volcanic rocks (Pawley et al., 2012).

### Current Yilgarn Terrane Descriptors

The oldest terrane is the Narryer Terrane, with a formation age ranging from 3730 to 3300 Ma (Ivanic et al., 2010). This terrane is situated in the northwest of the craton and is predominantly composed of high-grade gneiss with metasedimentary and metaigneous rocks (Ivanic et al., 2010). Hadean aged detrital zircon grains have been reported in this terrane, hosted by quartzite and quartz rich clastic metasedimentary rocks, affirming this age (Wyche et al., 2004). This terrane is separated from the adjacent Youanmi Terrane based on the Yalgarn Fault (northeast) and the Balbalinga Fault (southeast) shown on Figure 1.1 (Myers, 1993).

The Youanmi Terrane is the focus of the current study and contains the four volcano-sedimentary groups which were recognised by Van Kranendonk and Ivanic (2009). This terrane is split into two domains, the Southern Cross and the Murchison Domain. The current study is focused in the southwest Murchison Domain (Fig. 1.1), which consists of dismembered ultramafic-mafic layered intrusions and greenstones. Hadean and early Archean aged detrital zircon grains have also been reported in the Southern Cross Domain but not in the Murchison Domain. These are hosted by quartzite, with ages ranging from 4350 – 3130 Ma (Wyche et al., 2004). The boundary that separates the Murchison Domain and the Southern Cross Domain is based on a north-south trending fault.

The South West Terrane is the southern-most component of the craton (Fig. 1.1). It is composed of high-grade gneiss, supracrustal and granitic rocks which are > 3200 – 2600 Ma of age (Chen et al., 2003). The granitic rocks host detrital Hadean-aged zircons, showing that the terrane has an extensive history. Many theories have been proposed based on the presence of the zircons, including the inference that the ultramafic-mafic volcanism in the Murchison Domain was the product of a rift zone (Wyche et al., 2004).

The Eastern Goldfields Superterrane is the focus of the mining industry in the Yilgarn with extensive gold and komatiite-hosted nickel deposits. This superterrane is divided into the Kalgoorlie, Kurnalpi, and Gindalbe Terranes that has further internal domain divisions based on regional faults. The three main fault systems are Ida, Ockerburry and Hootanui (from west to east), which denote the boundaries of the domains as seen on Figure 1.1. The Kalgoorlie Terrane consists mainly of younger greenstones (2710 – 2660 Ma) overlying older greenstones and basement (> 2730 Ma; Cassidy et al., 2006). The Kurnalpi Terrane consists of mafic volcanic rocks (~ 2720 – 2700 Ma), mafic intrusive rocks, feldspathic sedimentary rocks, and complexes (~ 2690 – 2680 Ma) consisting of bimodal rhyolite-basalt sequences and felsic calc-alkaline rocks (Cassidy et al., 2006).

The Burtville Terrane consists of intermediate felsic (~ 2810 Ma) and ultramafic-mafic volcanic rocks, with metamorphosed mafic and felsic volcanic and sedimentary rocks (Cassidy et al., 2006). The Yamarna Terrane is the eastern most terrane of the craton (< 2720 Ma) and is separated by a north-northwest trending shear zone (Pawley et al., 2009). The shear zone is < 4km wide and runs along strike for 90 km.

Revision of these tectonic subdivisions has been conducted since the tectonostratigraphic scheme of Cassidy et al. (2006), with studies such as Van Kranendonk and Ivanic (2009) and Czarnota et al. (2010) conducting further research.

Czarnota et al. (2010) noted that these boundaries refer to a previous assumption that the craton had an allochthonous origin discussed further in this chapter. However, the boundaries are still used to group various geologically similar units together. This four-fold scheme (craton > Superterrane > terrane > domain) for division of the craton has recently been revised, with Smithies et al. (2018) alluding to these features as only late features in the western Yilgarn.

## Plume and Subduction Rock Types

One focus of this study is to distinguish between the geodynamic models that have been proposed for the western Yilgarn. These models include, mantle plume only, plume-subduction and subduction-only.

Igneous rock types can give an indication of the geodynamic processes that were active in the western Yilgarn in the Meso- Neo-Archean. Traditionally, komatiites and boninites have been used as evidence for plume and early subduction/proto-arc mechanisms respectively (see Watkins and Hickman, 1990; Barley et al., 2000; Pidgeon and Hallberg, 2000; Wyman and Kerrich, 2012). Schemes to distinguish these rock types, geochemically, are defined below.

## Granitoids

Preserved Archean continental crust can provide some insight onto the processes surrounding subduction and recycling of the oceanic crust at this time (Foley et al., 2003). This crust comes in the form of 4000 - 2500 Ma tonalite-trondjemite-granodiorite (TTG) granitoids making up to 90% of juvenile continental crust (Martin et al., 2005; Foley et al., 2003). Formation mechanisms for these granitoids are still debated. One idea is formation by partial melting of basaltic crust (eclogite and/or garnet-amphibole) and/or through melting of subducted oceanic crust (Martin et al., 2005;

Foley, 2003). Another idea is that TTG's formed through the melting of thickened (magmatically or tectonically) hydrous mafic crust (Smithies, 2000; Smithies and Champion, 2000). Hence, their proposed association with subduction process may indicate subduction influence in the Meso- Neo-Archean Yilgarn. Widespread contamination of Yilgarn granites by older crust (Champion and Cassidy, 2007), however, partially obscures the evidence of tectonic processes during their formation.

## Komatiites

Komatiites have been reported and mapped all around the world, mostly in Archean and Early Proterozoic cratons with greenstone belts as shown in Figure 2.1. They are thought to be derived from hot mantle plumes. Mantle plumes generally refer to a feeder and head system originating from the core-mantle boundary (Arndt et al., 2008; Campbell and Hill, 1988). Komatiites are formed through decompression melting of such hot ascending mantle (Sossi et al., 2016). This plume melting process can include varying degrees of partial melting over a wide range of pressures (Sossi et al., 2016). Therefore, komatiites are a great tool to understand the Earth's mantle composition and its changes throughout the Archean. Typically, they display spinifex texture, named for its similarity with spinifex grasses in Western Australia. One type of spinifex is "platy spinifex" that has been restricted to olivine crystals, which would be diagnostic of true komatiites. Lowrey et al. (2017), however, have shown that in the north Murchison Domain platy pyroxene crystals are preserved in Archean basalts (Lowrey et al., 2017). Hence, initial mapping of rocks with these platy pyroxene crystals were mislabelled as komatiites.

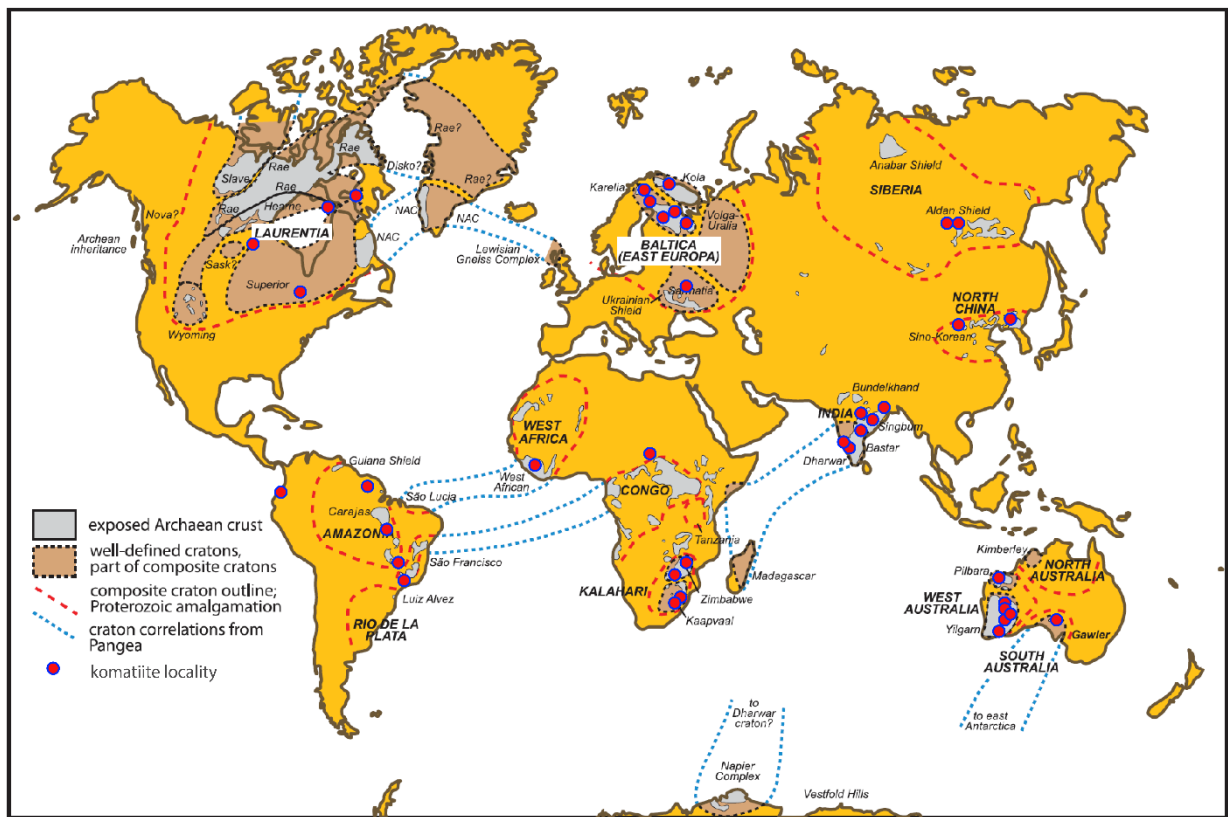


**Figure 2.1:** Komatiite locations globally (in red and blue circles). Grey areas represent global exposed cratons with Archean ages. Proterozoic aged cratons are outlined in red and craton correlation to Pangea are represented in blue. Adapted from Pearson and Wittig (2008) and Arndt et al. (2008).

Olivine-spinifex texture is due to the rapid cooling of the lava combined with high thermal gradients within the magma (Arndt et al., 2008 and references therein). Experiments to create pyroxene via rapid crystal growth in melt with a thermal gradient in laboratory studies, such as Bouquain et al. (2014), have been difficult to control and replicate. For either olivine or pyroxene spinifex, the primary mineralogy is commonly not preserved in Archean terranes. This is due to processes such as regional metamorphism, surface weathering and hydrothermal alteration (Lowery et al., 2017). These processes replace primary minerals with secondary ones, such as talc, amphibole, serpentine and chlorite (as seen in Chapter 4). Hence, the original composition of the magma is obscured.

To classify as a komatiite, at least some rocks at a given locality should show spinifex texture where the crystals are identified as acicular olivine (not acicular or platy

pyroxene crystals), implying high MgO contents (Lowery et al., 2017). Hence, the criteria for a komatiite, geochemically, is defined as < 50 wt% SiO<sub>2</sub>, > 18 wt% MgO and > 1000 ppm Ni (Lowrey and Ivanic, 2018). Additionally, acicular “spinifex” textures are not restricted to komatiites. This can be seen in platy calcic amphibole spinifex in rhyolite reported by Smithies et al. (2011) in the Musgraves Province, Western Australia and in platy calcite spinifex in a carbonatite flow reported by Copper & Reid (1991) in southwestern Namibia. Other rock types such as boninites can display spinifex or spinifex-like acicular pyroxene textures, for example some Cretaceous boninites outlined in Wood’s (1980) study of continental margin boninites.

## Boninites

Boninites were initially classified as high-Mg, high-Si (> 52 wt%) and low-Ti (< 0.5 wt%) rocks and were widely considered to signify the initiation of subduction zones in the post-Archean and Archean (Smithies et al., 2003; Pearce and Reagan, 2019). A typical composition can include microphenocrysts of orthopyroxene, olivine and clinopyroxene (Ohnenstetter and Brown, 1992). They can display spinifex texture and other glassy basalt textures and a cruciform to irregular polysynthetic twins of primary pyroxene that can be in the form of clinoenstatite as reported in this study.

Misclassification of boninites in the late Archean has occurred in the Yilgarn Craton. Boninites were not reported in the Murchison Domain until the Polelle Group boninites identified by Wyman and Kerrich (2012) in the northwest Murchison Domain, suggesting this was due to their textures, which are similar to siliceous high magnesium basalts (SHMB). Potential contamination issues (i.e., theories that the boninites were contaminated komatiites) and less specific boninite classification schemes may have also contributed to them being overlooked.

In the Phanerozoic, boninites are restricted to convergent margin settings, mainly seen in intraoceanic fore-arc and arc settings (Smithies et al., 2003). However, boninites with a current position in the fore-arc are usually displaced from the genesis position in the pro-arc (Patriat et al. 2019). They can also erupt in young back-arc basins and, much more rarely, in continental arcs (Piercey et al., 2001). Hence, in modern settings (post-Archean) boninites are strongly associated with a subduction-related petrogenesis. However, in Archean settings boninites and similar rocks may indicate other settings as described below.

Tectonics in the Archean are thought to be quite different to modern day long-lived subduction zones according to various studies such as Foley et al. (2003), Condie (2008), and Moyen and van Hunen (2012). A difference in thermal regime between modern day Earth and the Archean Earth was the prime reason for differences to modern subduction zones (Moyen and van Hunen, 2012). Hence, the Archean mantle was hotter than the modern mantle, which will result in an increase in partial melting and a decreased plate strength, causing short-lived subduction of slabs as seen in Figure 2.2 (Moyen and van Hunen, 2012). Other resulting factors influence subduction processes such as, thicker oceanic crust causing higher tensile stress between dense eclogitic crust at depth and the buoyant surface crust (Moyen and van Hunen, 2012). The average subduction velocity is predicted to have been larger in the Archean, based on numerical models described by Moyen and van Hunen (2012), therefore oceanic

crust is younger (weaker) when it arrives at the trench. A weak Archean mantle can lead to sublithospheric small scale convection and, therefore, lithospheric thinning (van Hunen et al., 2005) that did not provide support for the sinking slab. Lastly, the weak oceanic crust will result in decreased integrated strength in the subducting plate.

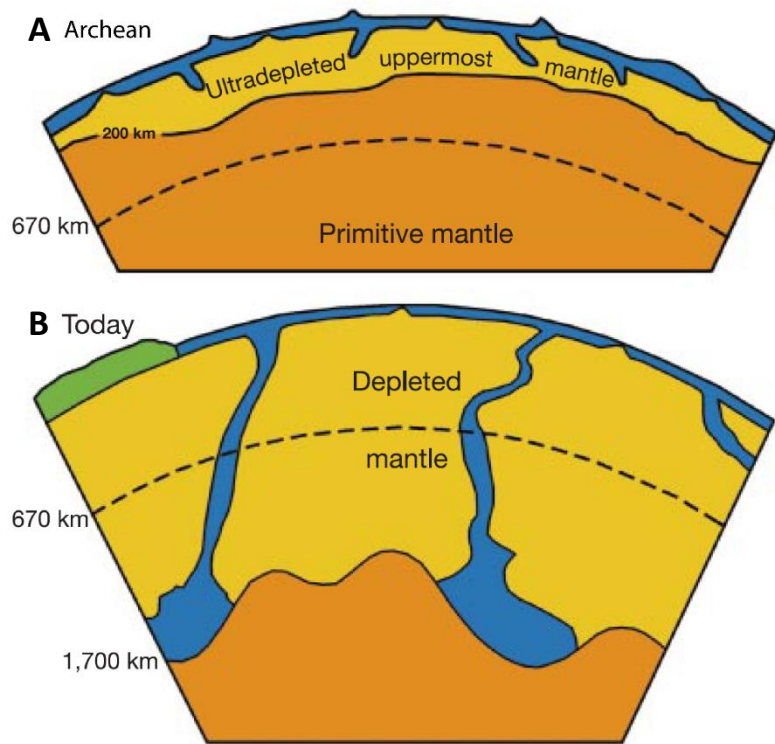


**Figure 2.2:** Differences between **A)** Archean tectonics and **B)** modern tectonics incorporating long-lived style subduction. From Foley et al. (2003).

Based on these factors and the general decrease in plate strength, Moyen and van Hunen (2012) argued that Archean subduction zones would have been short-lived. They argued that slab breakage in Archean subduction zones was a common occurrence, where cessation and re-initiation of the subduction zones would occur in a period of a few million years (Moyen and van Hunen, 2012). One possible implication would be that boninites or similar rocks would be more common due to the fact that there would be more juvenile arcs and few, if any, mature arcs.

## Subduction and Plume Models

### Plume Models

Mantle plume models have been the dominate model for the Meso-Archean Yilgarn. Recent studies have proposed such models for example, the Van Kranendonk et al. (2013) and Mole et al. (2014) models, although Mole et al. (2019) acknowledges the

presence of arc-related Norie and Polelle rocks as described by Wyman and Kerrich (2012), Smithies et al. (2018) and Wyman (2019).

The preferred model of Van Kranendonk et al. (2013) for the formation of the craton involves a single or multiple plume scenario to explain crustal evolution, which leads to the ribbon-style rifting of an older unified craton (Fig. 2.3). This model focuses on two periods of craton development. The first begins with the melting of the deep-sourced mantle plume at ~2820 – 2790 Ma (Van Kranendonk et al., 2013). With the melting of this plume, comes the placement of voluminous layered intrusions, eruption of mafic volcanics, and thinning of the cratons' centre (the Gindalbie Terrane in this model; Van Kranendonk et al., 2013). Following these events is the partial melting of older crust at ~2790 – 2760 Ma, involving the onset of faulting (Ida fault) in the Kalgoorlie, Gindalbie and Kurnalpi Terranes. The second period of plume magmatism begins ~2720 – 2675 Ma. This involves extrusive magmatism associated with komatiitic-basaltic volcanics from the Youanmi to the Burtville Terranes (Van Kranendonk et al., 2013). This plume was also responsible for 2720 Ma komatiites and magma underplating the thinned lithosphere in the Kalgoorlie, Gindalbie and Kurnalpi Terranes shown in Figure 2.3 (Van Kranendonk et al., 2013). The formation of the underplate created a new source for the later deep-crustal melting that formed the tonalite-trondhjemite-dacite magmas in the Kalgoorlie Terrane and the calc-alkaline magmas in the Kurnalpi Terrane (Van Kranendonk et al., 2013). At ~2690 – 2645 Ma, conductive heating caused widespread crustal melting and inputs continued from mantle-derived melts. This is then followed by the layering of underplated eclogitic residues (Van Kranendonk et al., 2013).

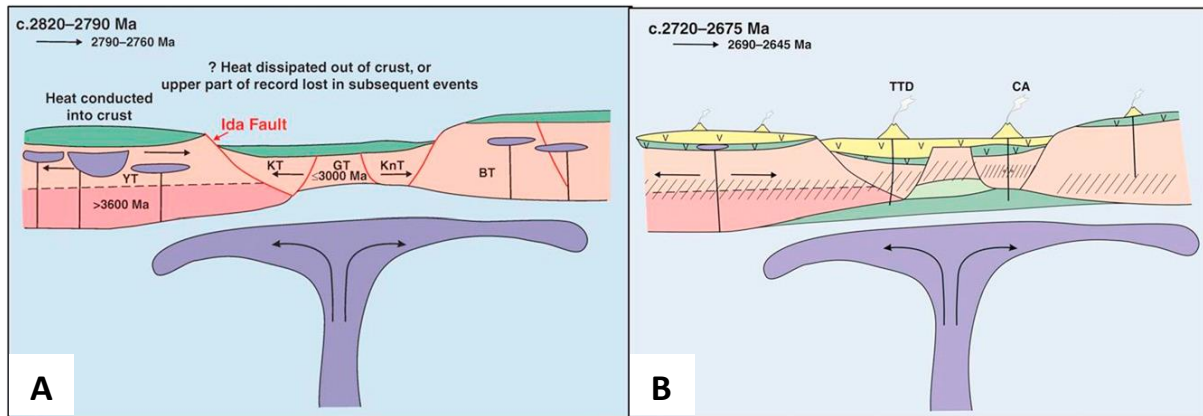


**Figure 2.3:** Two periods of plume magmatism, **A)** deep mantle plume head rises at 2820-2790 Ma **B)** the next phase in plume magmatism at 2720-2675 Ma. From Van Kranendonk et al. (2013). YT= Youanmi Terrane; KT = Kalgoorlie Terrane; GT=Gindalbie Terrane; KNT = Kurnalpi Terrane, BT= Burtville Terrane; TTD = Tonalite-Trondhjemite-Dacite; CA = Calc-Alkaline magmas.

The model explains the variety of volcanic felsic – intermediate rocks such as andesitic lavas and mafic granites as seen by the tonalite-trondhjemite-dacite magmas in the Kalgoorlie Terrane and the calc-alkaline magmas in the Kurnalpi Terrane by the same crustal melting and crustal contamination of plume-derived magmas (Fig. 2.3). Other papers favouring mantle plume models, including Barnes et al. (2012) and Mole et al. (2014) infer similar processes for the formation of felsic and intermediate volcanic and plutonic rocks.

At the time of their publication, Van Kranendonk et al. (2013) did not assign the supracrustal rocks in the southern Murchison Domain into their proposed lithostratigraphic scheme but the model also requires a ~2830 Ma “Norie mantle plume” responsible for the Norie Group volcanics throughout the domain. The plume model in Wyman and Kerrich (2012) has been re-evaluated by Wyman (2019). In light of the new findings in Wyman (2019) and Lowrey et al. (2019 in press) described below, long lived mantle plume models (Van Kranendonk et al., 2013) seem to be an unlikely scenario. This is due to the distribution of boninites and other subduction-style rocks found recently in the Murchison domain.

Crustal contamination is a major concern throughout the Yilgarn, highlighted by studies such as Wyman and Kerrich (2012), Van Kranendonk et al. (2013) and Barnes and Van Kranendonk (2014). Contamination of volcanic rocks such as boninites, inhibits the understanding of the cratons' development. Subduction related magmas (including boninites) can be hard to distinguish geochemically from crustally contaminated plume derived magmas such as Al depleted komatiites (Leshner and Arndt, 1995; Lowery et al., 2019 in press). If occurrences of uncontaminated boninites can be demonstrated, however, they provide good evidence for some form of subduction in the Archean (Polelle Group) at 2825 – 2700 Ma (Wyman and Kerrich, 2012).

Van Kranendonk et al. (2013) suggested that plate tectonic processes were unlikely to have been active in the Youanmi Terrane during deposition of the Norie and Polelle Groups for a number of reasons. Komatiitic/basaltic rocks in the Eastern Goldfields Superterrane are of similar deposition ages and sources. Their solution to this is mantle plume magmatism in an earlier boundary of the Youanmi Terrane and the Eastern Goldfields Superterrane. The next argument outlined is the presence of xenocrystic and detrital Hadean zircon grains in the Youanmi Terrane (Southern Cross), where these are a typical feature of the Narryer Terrane. These grains imply crustal formation in the Hadean (> 4000 Ma) and thus possible recycling of the Narryer and Youanmi Terranes. Thus, creating an assumption that these terranes are somewhat related. Another weakness of the plate tectonic models was said to be the occurrence of granitic magmatism reported at 2690 Ma before the terrane accreted at 2660 Ma. The last objection was that the plate tectonic model implied that subduction related magmatism at 2690 – 2660 Ma occurred across the entire craton (~1000 km).

## Subduction Models

Models for the Meso-Neo-Archean Yilgarn are increasingly incorporating subduction in models for the formation of the craton as applied to many other cratons, with or without plumes involvement. Examples include the Superior Province (Hollings et al., 1999), the Dharwar Craton (Chandan-Kumar and Ugarkar, 2016) and the Southwest Greenland Craton (Kisters et al., 2012). However, with the rise of numerous plume-subduction interaction models, other studies such as Van Kranendonk et al. (2013) and Barnes et al. (2012) argue that few modern examples of plume-subduction interactions have been documented. Barnes and Van Kranendonk (2012) left open as a possibility of an arc-accretion story for the wider Yilgarn. However, their findings in the Eastern Goldfields Superterrane present a Low-Th Basalt group with typical Ni and Cr enriched Archean flood basalt features which support a plume head volcanism and thus a komatiite association (Barnes et al., 2012).

Development of subduction models began with Myers (1993) implementing the idea of terrane accretion/amalgamation and plate tectonics (back arc basins, volcanic arcs and microcontinents). However, this study was lacking conclusive evidence for terrane accretion/amalgamation, although other studies such as Wilde et al. (1996) provided evidence in partial support of the Myers' (1993) model because it involved terrane accretion of the South-West Terrane.

Champion and Cassidy (2007) inferred accretion of the Yilgarn terranes i.e. the Narryer Terrane, EGS, southwest terranes onto the Youanmi Terrane which acts as the tectonic foreland (older nucleus). Czarnota et al. (2010) incorporated information from the study and describe, in depth, the generally accepted (at time of writing) para-autochthonous tectonic model for the Eastern Yilgarn Craton, incorporating work from various authors (e.g. Champion and Cassidy, 2006; Barley et al., 2008; Champion and Cassidy, 2007 etc.). This model assumed early arc-subduction ( $\geq 2940$  Ma) as the

primary formation mechanism for the early Youanmi Terrane. Later ~2810 Ma extension followed the formation of the early Youanmi Terrane and several studies since Czarnota et al. (2010) have argued for subduction on the Yilgarn's eastern margin between 2830 and 2730 Ma (Wyman, 2019 and references therein). Czarnota et al. (2010) also show that a ~2715 – 2690 Ma subduction event occurred later in the east, dipping towards the west. At ~2690 – 2665 Ma the subduction zone began to shallow over a thermal anomaly (plume) which initiated felsic volcanism generating the tonalite-trondjemite-granodiorite (TTG) granitoids and High-Ca granites. A ~2670 Ma event in the west and in the east ~2665 Ma, of diachronous arc closer causing compression and crustal thickening. A ~2665 Ma event in the west and in the east ~2660 Ma, of extension from mid orogeny causing the mineralization of gold. A ~2655 Ma contraction event in the west and in the east ~2650 Ma, occurred with a switch to Low-Ca granite magmatism from High-Ca (also, Champion and Cassidy, 2007). A ~2650 Ma event in the west and in the east ~2645 Ma, where crustal melts were emplaced such as the Low-Ca granites. With no subduction evidence after this time in the Yilgarn, the final events are classified as post-orogenic (Czarnota et al., 2010; Champion and Cassidy, 2007). Cratonization is the final event in this model with the termination of Low-Ca granite magmatism (~2630 Ma in the west, ~2620 Ma in the east).

## Western Yilgarn

Boninitic rocks in the Youanmi Terrane was first reported by Wyman and Kerrich (2012). Wyman and Kerrich (2012) attempted to accommodate a ~2830 Ma “Norie plume” in the study of volcanic rocks from Cue to Meekatharra. This plume would explain the Norie Group volcanics previously reported in the sequence (e.g., Van Kranendonk and Ivanic, 2009; Van Kranendonk et al., 2013). In summary, the 2825 – 2740 Ma model begins with the > 2825 Ma “Norie plume” being responsible for the rifting between the Narryer and the proto-craton Yilgarn (Fig. 2.4A), separation of the

Narryer Terrane in a 2825 – 2815 Ma rifting event in proto-craton Yilgarn (Fig. 2.4B) and rifting occurring on the eastern side of the craton (Fig. 2.4C; Wyman and Kerrich, 2012). The eastern terranes (Kalgoorlie, Burtville and Kurnalpi) were inferred to have been generated from the volcanism associated with this rifting event (Wyman and Kerrich, 2012). Subduction induced magmatism at 2800 – 2740 Ma on the western margin of the Youanmi Terrane occurs with the collision of the Narryer and Youanmi Terranes. Convergence at 2715 – 2660 Ma between the eastern terranes and the western terranes Plume then linked the craton.

Wyman (2019), however, argues that there too many subduction related rocks (from wet mantle sources) in the Norie and Polelle Groups and little evidence for a plume so that the earlier plume-subduction and plume-only models (Van Kranendonk et al., 2013) are unlikely contenders for the evolution of the western Yilgarn

Smithies et al. (2018) also argue that, although the komatiite bearing greenstone belts in the EGS display evidence of crustal contamination, the constant Th/Nb of volcanic rocks in the Norie and Polelle Groups indicate that their chemical signatures are true evidence of subduction processes.

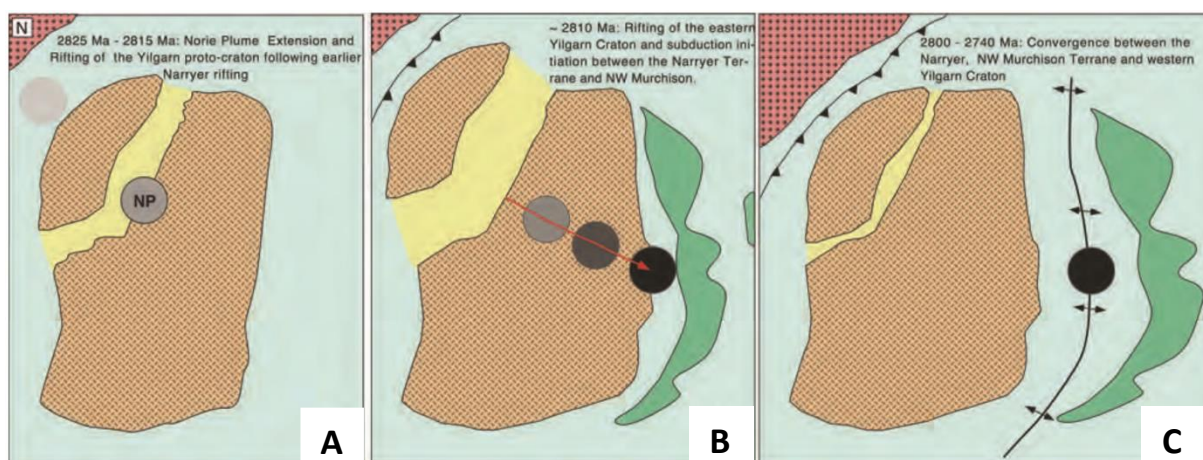


**Figure 2.4:** A) onset of extensions and rifting in the proto-craton at 2825-2815 Ma B) subduction between the Narryer Terrane and northwest Murchison Domain at ~2810 Ma C) convergence episodes at 2800-2740 . From Wyman and Kerrich (2012).

## Murchison Domain Stratigraphic Models

As with the large-scale changes applied to terranes and domains in the Yilgarn, more local stratigraphic schemes have also undergone frequent changes as a result of continued mapping, geochemical analysis and geochronological studies. The reinterpretations continue so that some of the rock types and their associated stratigraphical groupings on quite recent maps produced by the Geological Survey of Western Australia (GSWA) (e.g. Yalgoo, Ninghan, and Cue maps) have already been re-interpreted. For example, the Cue geological map of 2015 is not entirely consistent with the rock types and stratigraphic units described by more recent literature. Another study by Lowery et al. (2019 in press) has reclassified rock types on the regional maps. They reclassify some rocks assigned in 2015 to the Glen Group volcanics, southwest of Meekatharra, to Polelle Group volcanics. Therefore, the classification of stratigraphical groups (either Polelle or Norie) used in later chapters must be considered with caution for future studies, due to any possible revisions of the GSWA geological maps. In fact, assessing the present regional stratigraphic models in the four study areas is a significant objective of this research project.

Ideas on the development of the Yilgarn Craton have been changing since the 1990's, starting with Watkins and Hickman (1990). They created a stratigraphic scheme for the "Murchison Supergroup", dividing the terrane (not the current "Murchison Domain") into two groups, the older Luke Creek Group and the younger Mount Farmer Group. The main fault with the scheme was the reliance on regional correlations of apparently similar volcanic sequences with poor constraints from radiometric dating. Wang et al. (1993) used geochemical and geochronological data to improve on the classification of recrystallised granites, which involved subdividing them into 3 categories: monzogranite-granodiorite, trondhjemite-tonalite and monzogranite-syenogranite. However, in combination with the geochronological data produced by Pidgeon and Hallberg (2000), inconsistencies were detected within the

stratigraphic framework provided by Watkins and Hickman (1990) for the northeastern Murchison.

An important study of Yilgarn granite geochemistry was made by Cassidy et al. (2002), who identified four distinct suites in the northern Murchison Domain: high-Ca granites, low-Ca granites, mafic granites, high-HFSE granites and syenite. However, this classification scheme still lacked sufficient support from geochronological data, hence Champion and Cassidy (2007) improved on this by adding direct correlations through dating of numerous granite samples.

Van Kranendonk et al. (2013) provided a detailed description of a revised stratigraphic model for the Murchison Domain based on new geochemical data, mapping and geochronological data to devise a stratigraphic scheme shown in Figure 2.5 that has been the foundation for more recent studies. They split the volcano-sedimentary rocks into four groups. The first group denotes the ~ 2960 – 2935 Ma Mount Gibson Group consisting of felsic and mafic volcanics/volcaniclastics, located in the south Murchison (Van Kranendonk et al., 2013). A gap in the stratigraphy between the Mount Gibson Group and the Norie Group volcanics exists, which represents a  $\leq 110$  Ma hiatus in magmatism as shown in Figure 2.5 (Van Kranendonk et al., 2013). The second group is the 2825 – 2805 Ma Norie Group, composed of felsic volcaniclastic sandstones, mafic volcanic rocks and banded iron formation, located domain-wide (Van Kranendonk et al., 2013). The third group is the 2800 – 2735 Ma Polelle Group, containing intermediate – felsic volcanic/volcaniclastic sedimentary rocks, banded iron formation and ultramafic-mafic volcanic rocks (Van Kranendonk et al., 2013). The fourth group, the 2735 – 2700 Ma Glen Group, includes coarse sedimentary rocks, minor rhyolite and “komatiitic basalt” (Van Kranendonk et al., 2013). The latter is actually pyroxene spinifex-bearing volcanic flows with MgO as low as 5.6 wt%. The two stratigraphic groups examined in the present study are the Polelle and Norie Groups.



## Norie Group

The Norie Group (~ 2825 – 2805 Ma; Van Kranendonk et al., 2013), as presently defined, occurs in areas covered by both the Yalgoo (Fig. 2.6; Ivanic et al., 2015) and Ninghan (Fig. 2.7; Ivanic, 2018) maps. However, the Norie samples in this study correspond to the Singleton Formation of the Norie Group of the Ninghan map. The Norie Group on the Ninghan (Ivanic, 2018) map includes the earlier Singleton Formation and above this, volcanic units not assigned to specific formations. The Singleton Formation consists of psammitic and pelitic schist, metabasalt, metamorphosed ultramafic rock, serpentized metaperidotite and metamorphosed pillowed/pyroxene spinifex basalt. The overlying rocks consists of metabasalt, metasedimentary rocks, metamorphosed banded chert/iron-formation, and volcanoclastics.

## Polelle Group

The 2015 Yalgoo map of Ivanic et al. (2015), shown in Figure 2.6, presents the distributions of formations and members of the 2800 – 2735 Ma Polelle Group along with brief descriptions of their rock types and textures (Van Kranendonk et al., 2013). According to the 2015 Yalgoo map, the earliest member in the Yalgoo Formation (more recently re-defined as the Meekatharra Formation: GeoView, 2019) is the Mugs Luck Basalt Member. This member was described as consisting of metamorphosed spinifex textured basalts, ultramafic schists, banded iron formations (BIF), sedimentary layers including sandstone and siltstone, and pillow basalts. As is common during the ongoing re-evaluation of the Murchison Domain, however, the Mugs Luck Basalt and the Carlaminda Komatiite Member of the 2015 map are being re-evaluated and may be merged in the future (J. Lowrey, GSWA, pers. comm., 2019). The “Komatiite Member” consists of tremolite-chlorite-actinolite ± talc (greenschists), serpentinite, metamorphosed volcanoclastics, peridotite, and was reported to include olivine

spinifex textured komatiite with flows of pyroxene spinifex-textured basalt (metamorphosed). More recent studies (Jack Lowrey, GSWA pers. comm., 2019) and the present study show that the “komatiites” have been mislabelled and are actually basalts or picrites exhibiting pyroxene spinifex textures.

The Singleton Basalt Member overlies these rocks (currently been reassigned). This member is composed of psammite, metabasalts, mafic schists, pillow basalts, pyroxene spinifex textured basalt (metamorphosed), amygdaloidal basalt, and spherulitic basalt. The youngest member is the Yilgaddy Andesite Member, which consists of metamorphosed andesites and basalts, felsic schists, and metamorphosed andesitic volcanic breccia. All rock types in this formation are subject to metamorphism or are locally strongly sheared.

On the 2018 Ninghan map (Ivanic, 2018), shown in Figure 2.7, formations of the Polelle Group are briefly described in terms of rock type and texture. Within the Polelle Group is the Meekatharra and Coodardy Pool Formations. These formations consist of metamorphosed basalts, quartzite and psammite, BIF, rhyolite, and schists. The earliest formation is the Coodardy Pool Formation, which consists of an altered garnet-mica schist. The Meekatharra Formation contains a variety of rock types. These include quartzite and psammite, metamorphosed BIF, tremolite-chlorite(-talc) schist, metamorphosed rhyolite and metamorphosed pillowed/variolitic/amygdaloidal/pyroxene spinifex textured basalts. The Meekatharra Formation is the only formation from this map that is included in the current study.

# Yalgoo Map

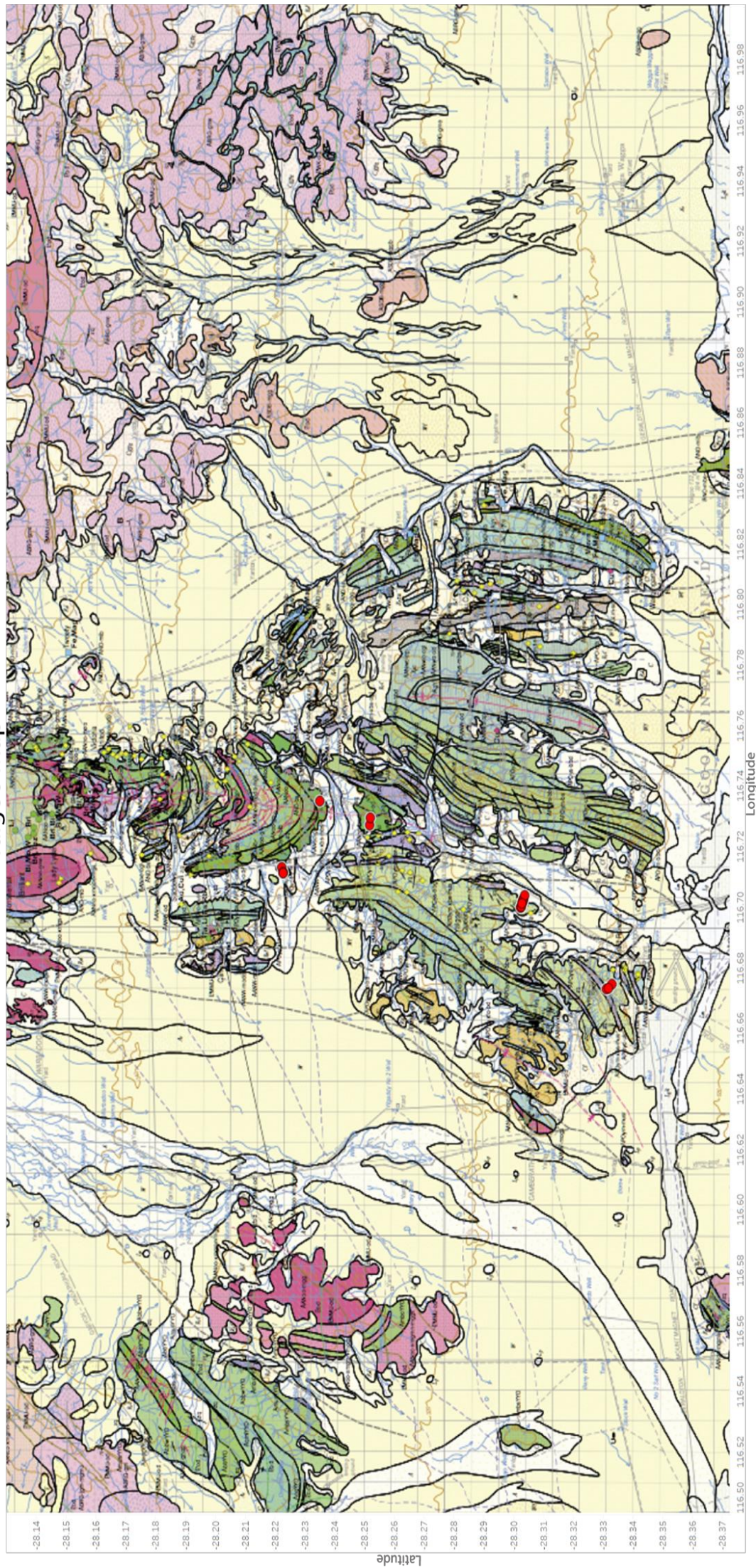
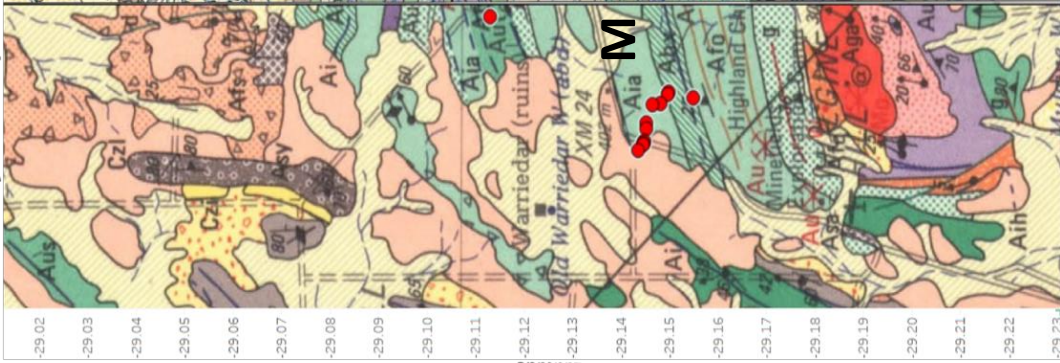


Figure 2.6: Yalgoo geological map with samples from this study plotted with a red circle. From Ivanic et al. (2015)

Perenjori Map



Ninghan Map

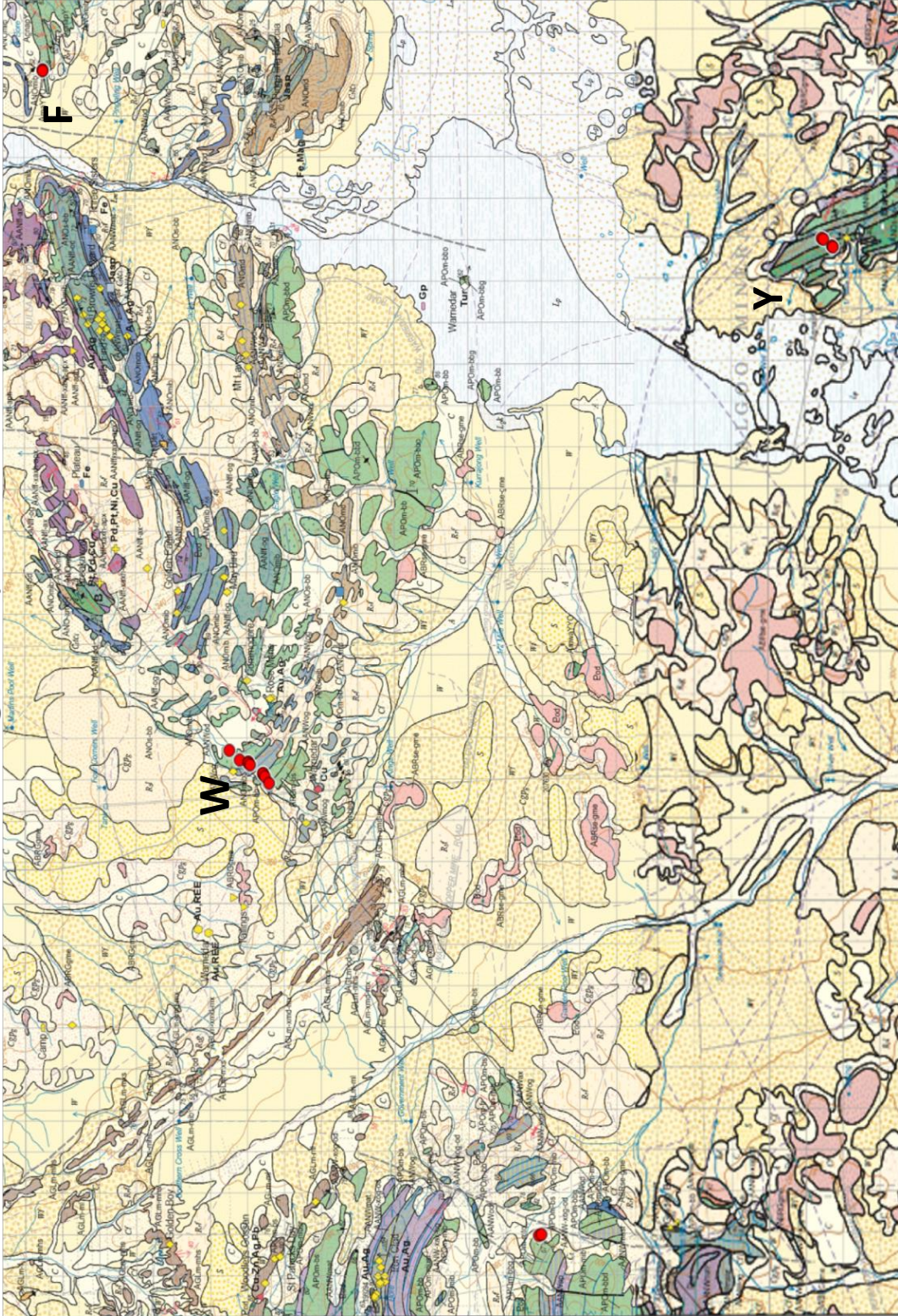
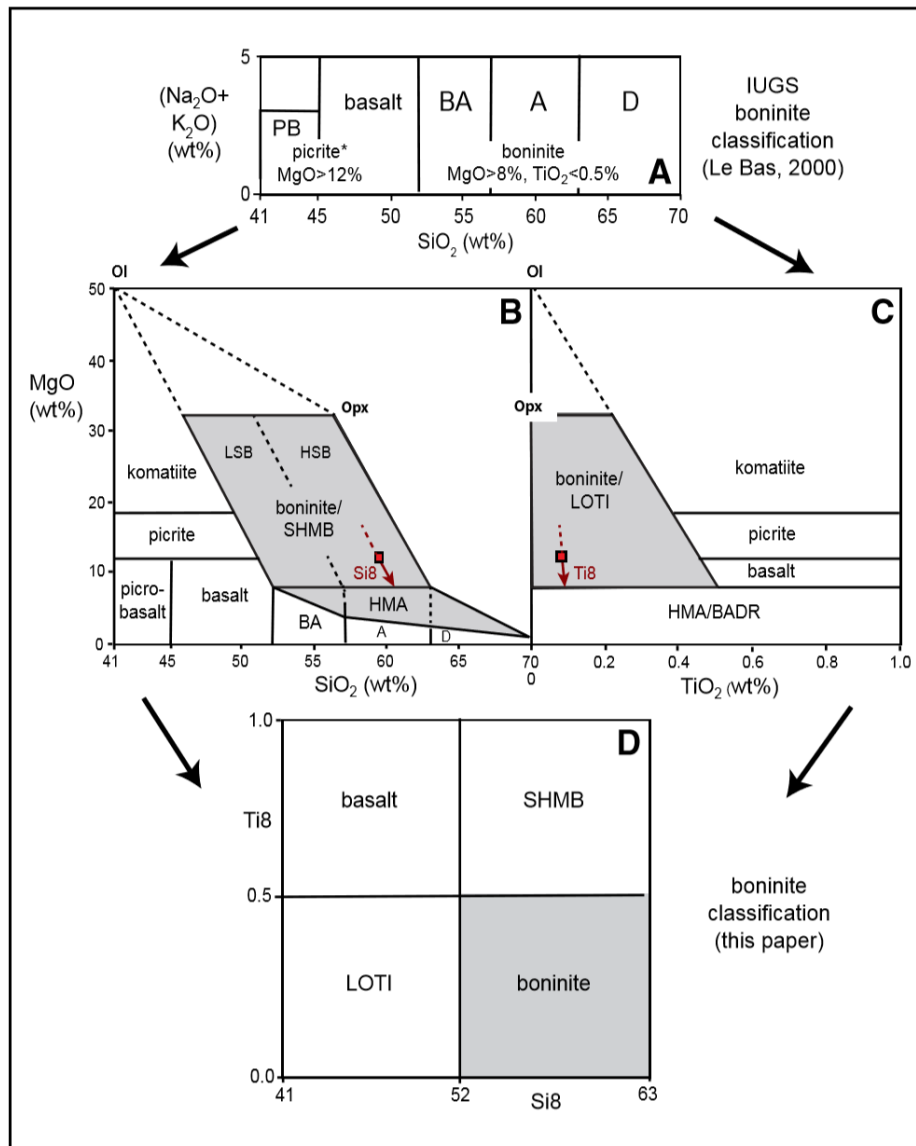


Figure 2.7: Perenjori and Ninghan geological maps with samples from this study plotted with a red circle, where M = Mt. Mulgine, F = Fields Find East, Y = Yeoh Hills and W = Warriedar. From GSWA (1983) and Ivancic (2018) respectively.

## New Rock Type Classifications - Pearce and Reagan (2019)

In addition to the frequent changes occurring in the classification of Yilgarn domains and Murchison stratigraphic units, the classification of important Archean rock types has been revised in 2019 during the time of the present study.

Pearce and Reagan (2019) have published new discrimination plots to distinguish boninites and other rock types based on their chemical composition and it is likely that these new definitions will eventually receive official acceptance. These diagrams satisfy the International Union of Geological Sciences (IUGS) composition requirements for a boninite of  $Si_8 > 52$  and  $Ti_8 < 0.5$  (see Chapter 3). These terms refer to the concentration of the oxide forms,  $SiO_2$  and  $TiO_2$  at fractionation trends of 8 wt% MgO. Their discrimination diagrams also require a normalization to a 100% volatile-free foundation and a particular method for partition of iron  $Fe^{2+}$  and  $Fe^{3+}$  into the sum of oxides totalling to 100% (Pearce and Reagan, 2019). The boninite boundaries in these diagrams deviate from the IUGS scheme by using mineral controls lines, instead of traditional constant  $SiO_2$  and  $TiO_2$  values. Hence, the use of non-vertical olivine and orthopyroxene control lines rather than the vertical boundaries of the IUGS discrimination plot (Fig. 2.8A). These control lines are more realistic than those of the IUGS classification, however, magma evolution involving clinopyroxene fractionation can still result in magma trends crossing over classification boundaries. Three discrimination plots were produced to identify boninites. These are the MgO- $SiO_2$ , MgO- $TiO_2$ , and  $Si_8$ - $Ti_8$  discrimination plots and are seen on Figure 2.8B, C, and D used in Chapter 3. These plots have identified the boundaries between various rock types, including Low-Si boninites (LSB) and high-Si boninites (HSB), high-Mg andesites (HMA), siliceous high-Mg (SHMB), picrites, and low-Ti basalts (LOTI), some of these rock types are shown in their tectonic settings on Figure 2.9.



**Figure 2.8:** **A)** IUGS scheme for high-Mg volcanic rocks - from Le Bas (2000). **B)** MgO vs SiO<sub>2</sub> plot from Pearce and Reagan (2019) **C)** MgO vs TiO<sub>2</sub> plot from Pearce and Reagan (2019) **D)** Ti8 vs Si8 plot from Pearce and Reagan (2019).

In the past, classification of Archean boninites has been confused partly because fractionation processes were not accounted for in the original definitions of any boninites, as highlighted by Pearce and Reagan (2019). Confusion could also be due to the misinterpretation of tectonic settings or silicification (Pearce and Reagan, 2019). Pearce and Reagan (2019) include results that show, during the 2000 – 3000 Ma period, that “boninite-siliceous high Mg basalt associations formed by melting of refertilized, depleted cratonic mantle in intracratonic rift or rift-edge settings”. Hence, indicating a wider variety of potential settings in which Archean boninite’s could form in.

Using their revised classification scheme, Pearce and Reagan (2019) identified a number of Archean boninites and their tectonic settings. These include,

- Barberton AUK-Type “Boninites” (fractionated “Al-undepleted komatiites”)
- Comondale-Type “Boninites” (formerly “Comondale Komatiites”)
- BK-Type “Boninites” (formerly “Basaltic Komatiites”)
- Whitney-Type “Boninites”
- Mallina-Type “Boninites”
- Kambalda-Type “Siliceous High-Mg Basalts”
- Whundo-Type “Boninites”
- Nuvvuagittuq-Type “Boninites”

Rocks similar to Barberton AUK komatiites and Barberton AUK-Type “Boninites” and have been reported along with Kambalda-Type “Siliceous High-Mg Basalts” in the Yilgarn Craton, but this association is generally considered to represent mantle plume associated Large Igneous Province (Hayman et al., 2015).

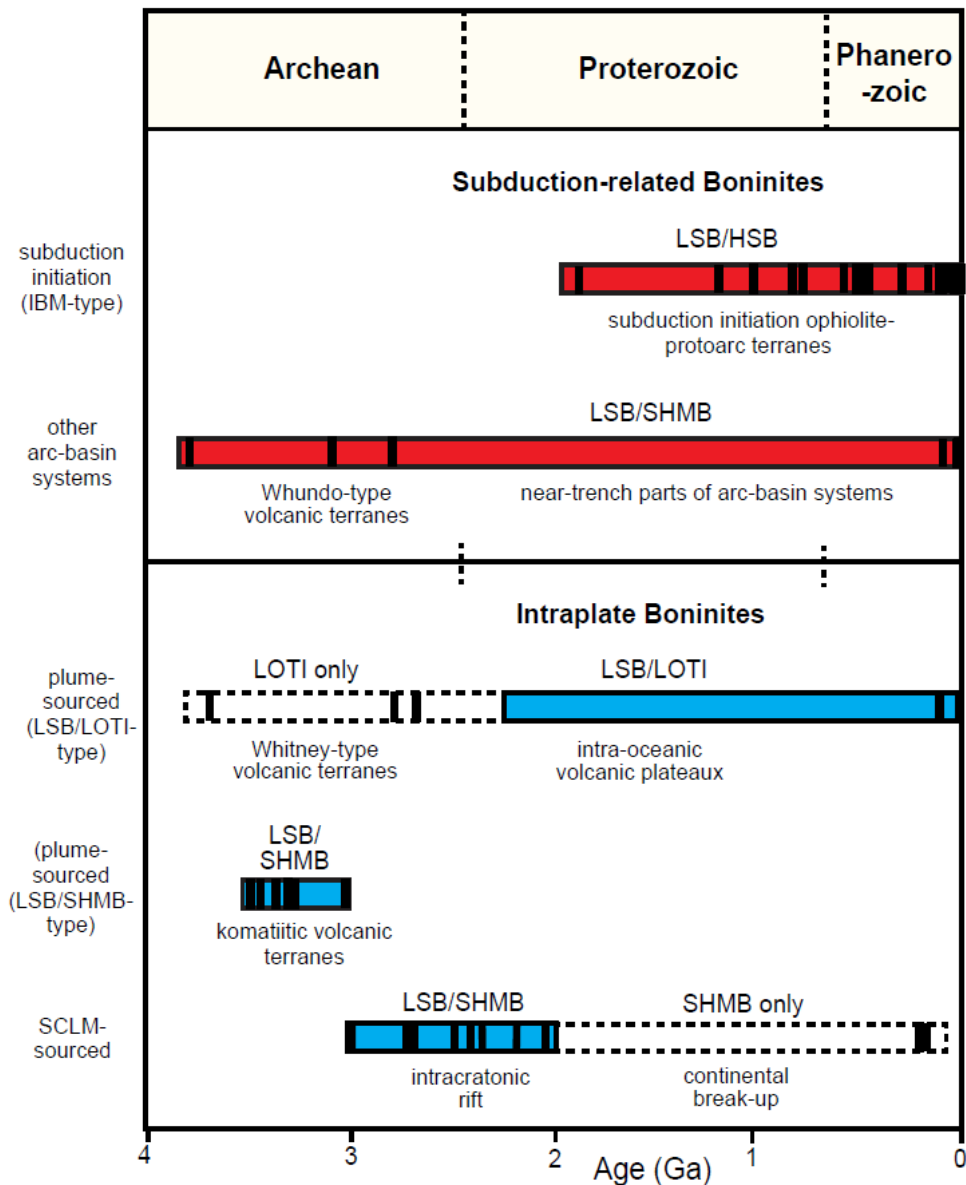


Figure 2.9: Archean and post-Archean boninite types in multiple settings including plume sourced boninites and subduction initiated boninites, from Pearce and Reagan (2019).

## Rock Type Descriptions for the Pearce and Reagan Classification Scheme

### LSB & HSB

Crawford et al. (1989) subdivided boninites based on Ca, creating two divisions of “low-CaO” and “high-CaO”. The high mobility of Ca causes these subdivisions to be inadequate for old volcanic rocks, such as in this study, and was mainly used for petrogenetic discussions. This was improved by Kanayama et al. (2013), dividing the field based on Si, as also seen in the Pearce and Reagan scheme. Subdivisions into low-

Si boninites and high-Si boninites are used on the MgO-SiO<sub>2</sub> discrimination plot with a bounding value of Si<sub>8</sub> = 57. This boundary corresponds to the basaltic andesite and andesite composition boundary in the IUGS TAS diagram (Fig. 2.8A).

### *HMA*

A new definition for high-Mg andesite (HMA) was also added to the scheme, as seen in the MgO-SiO<sub>2</sub> discrimination plot in Figure 2.8B. This category does not overlap with either LSB or HSB boninite categories as other previous criteria and encompasses a wide variety of rocks (Tatsumi et al., 2003). Previous overlap between the HMA and basalt-andesite-dacite-rhyolite field did not align with the IUGS TAS classification scheme, whereas the new boundaries in this classification scheme are compliant with the TAS diagram.

### *SHMB*

Siliceous high-Mg basalts (SHMB), originally termed siliceous high-Mg series basalts (SHMSB) by Redman and Keays (1985), are common in Archean greenstone belts. Archean SHMB have been compared to early Proterozoic SHMB by Sun et al. (1989) who considered the involvement of felsic crust in the contamination of Archean and early Proterozoic magmas but also suggested a range of possible mechanisms for their generation. These included subducted sediments modifying the upper mantle sources or interactions between rising komatiite magmas and melting continental harzburgitic lithosphere (Sun et al., 1989). Primary magmas could have had komatiite or boninite compositions prior to the melting of refractory lithospheric mantle (Sun et al., 1989). Hence, at least some SHMB may form from contaminated magmas as in the Eastern Goldfields Superterrane where they appear to be related to komatiites (Sun et al., 1989).

## *Picrites*

Picrites are high-Mg rocks with abundant olivine phenocrysts, that are formed in several tectonic settings, including arc-settings where they can fractionate to arc-basalt. These lavas have been mislabelled as komatiites, due to their high-Mg contents (geochemistry) but petrographic evidence, or mineral compositions, can often distinguish between them. An example of this is highlighted by Baziotis et al. (2017), where the non-spinifex lava was relabelled to a picrite. The high-Mg contents in the picrite were due to accumulated olivine as revealed by the high Mg content of the olivine, which reflected the original magma composition. The boundaries for picrites in the Pearce and Reagan plots were directly taken from the high-Mg volcanic rocks IUGS classification scheme (Figure 2.8A; Le Bas, 2000). This rock type has low SiO<sub>2</sub> values (generally < 52 wt%) and high-Mg contents (12 - 18 wt%) (Le Bas, 2000; Pearce and Reagan, 2019).

## *LOTI*

Low Titanium mafic volcanic rocks are associated with boninites, where MgO and SiO<sub>2</sub> values are similar, and Ti values are lower than boninites. LOTI values on the current Pearce and Reagan (2019) plots refer to a < 52 wt% Si<sub>8</sub> and < 0.5 wt% Ti<sub>8</sub> composition as seen in Figure 2.8D (Si<sub>8</sub> and Ti<sub>8</sub> definition in Chapter 3). Cambrian LOTI and boninite rocks from Tasmania were compared to Tertiary LOTI and boninites by Brown and Jenner (1989). They concluded that these rocks are consistent with a supra-subduction zone setting involving mantle depletion by melting and re-enrichment by subduction and that no other tectonic environment is consistent with the volcanic sequence in Tasmania.

## Study Areas

The study areas are located in the central west Murchison Domain, in the larger Youanmi Terrane of the Yilgarn Craton. Geological maps of the area from the GSWA were used in order to extrapolate stratigraphical units/rock types and groups (Norie or Polelle in this study). Four maps were used, the Yalgoo 2015 map (Ivanic et al. 2015), the Ningham map (Ivanic 2018), the Perenjori map (GSWA, 1983) and the on-line WA Geological Survey 1:100,000 Interpreted Bedrock map compilation (Geoview, 2019).

### **Mt. Mulgine**

The Mt. Mulgine study area is located south of Cue and Mount Magnet on the Ningham map (Ivanic, 2018) and the Perenjori map (GSWA, 1983). Samples were collected around the Mt. Mulgine and Warriedar areas as shown on Figure 2.7. Rock types associated with the sample locations are documented by Ivanic (2019). These include, amygdaloidal basalt with quartz filled vesicles, pyroxene spinifex-textured basalt, metamorphosed peridotite (with relict cumulate textures), and tremolite-chlorite(-talc) schist. The inferred stratigraphic group for these rocks is the Polelle Group, specifically the Meekatharra Formation and Warriedar Suite.

### **Yeoh Hills**

The Yeoh Hills study area is located south of Cue and Mount Magnet on the Ningham map (Ivanic, 2018). Samples were collected just north of Pinyalling in Paynes Find as shown on Figure 2.7. Rock types associated with the sample locations are documented by Ivanic (2018). These include, metabasalt, metamorphosed pillowed basalt and metamorphosed dolerite. The associated stratigraphical groups for these rocks are the Polelle (Warriedar Suite) and Norie Group (Singleton Formation).

## Warriedar

The Warriedar study area is located south of Cue and Mount Magnet on the Ninghan map (Ivanic, 2018). Samples were collected in and around Fields Find East and north-northwest of Lake Moore at the hinge of an anticline as shown on Figure 2.7. Rock types associated with the sample locations are documented by Ivanic (2018). These include, metamorphosed locally pillowed basalt, metamorphosed gabbro, metamorphosed massive to weakly foliated pillowed basalt, and meta-ultramafic intrusive rock. The associated stratigraphical groups for these rocks are the Polelle (Meekatharra Formation and Warriedar Suite) and Norie Groups (Singleton Formation).

## Yalgoo

The Yalgoo study area is located southwest of Cue on the Yalgoo area map (Ivanic et al. 2015). Samples were collected within and around the Noongal anticline and the north-south striking greenstone belt, shown on Figure 2.6. Rock types associated with the sample locations are documented by Ivanic et al. (2015). These include, locally metamorphosed pyroxene spinifex-textured basalt and platy olivine spinifex-textured komatiite with flows of pyroxene spinifex-textured basalt. The associated stratigraphical group for these rocks is the Polelle Group, specifically the Mugs Luck Basalt Member and Carlaminda "Komatiite" Member.

## Chapter 3 Analytical Methods

### Petrography

Petrographic analysis of 43 samples was conducted using a Zeiss Primotech Polarizing Microscope at the University of Sydney, using transmitted light and reflected light. Thin section photographs were captured with the integrated IP 3MP camera on the Zeiss Primotech Polarizing Microscope. Thin sections were prepared with an ideal thickness of 30  $\mu\text{m}$ . The samples were then analysed based on mineral assemblages and textures (primary-igneous and secondary). These were then put into groups of similar textures.

### Geochemistry

Whole rock geochemistry was conducted on 54 samples. These data are a part of a larger Southern Murchison database (WACHEM) from the Geological Survey of Western Australia (GSWA). The database also includes re-analysed Watkins and Hickman (1990) samples.

ALS Brisbane conducted research grade geochemical analysis on the 54 samples. The analysis package selected was the complete characterisation package (CCP-PKG01). This was selected due to the lack of mineralisation in the samples. This package is a combination of two packages to quantify the major elements in each sample. The whole rock package (ME-IR08) and carbon and sulphur by combustion furnace package (ME-IR08). Trace elements and rare earth elements suites (REE) are also included in this duo package. Data are extracted from three digestions, a lithium borate fusion for the resistive elements (ME-MS81), a four-acid digestion for the base metals (ME-4ACD81), and an aqua regia digestion for the volatile gold related trace elements (ME-MS42) (ALS Global, 2015). Each of these digestions either used an

inductively coupled plasma atomic emission spectrometer (ICP-AES) or inductively coupled plasma mass spectrometer (ICP-MS) finish. The ICP-AES finish quantifies the major element oxide concentrations ( $\text{SiO}_2$ ,  $\text{Al}_2\text{O}_3$ ,  $\text{Fe}_2\text{O}_3$ ,  $\text{CaO}$ ,  $\text{MgO}$ ,  $\text{Na}_2\text{O}$ ,  $\text{K}_2\text{O}$ ,  $\text{Cr}_2\text{O}_3$ ,  $\text{TiO}_2$ ,  $\text{MnO}$ ,  $\text{P}_2\text{O}_5$ ,  $\text{SrO}$ ,  $\text{BaO}$ , and LOI) and the ICP-MS finish quantifies the rare earth elements (Ba, Ce, Cr, Cs, Dy, Er, Eu, Ga, Ge, Gd, Hf, Ho, La, Lu, Nb, Nd, Pr, Rb, Sm, Sn, Sr, Ta, Tb, Th, Tm, U, V, W, Y, Yb, and Zr).

### Boninite Discrimination Plots

The updated Pearce & Reagan (2019) discrimination plots were used in the analysis of rock types, including boninites, basalts and high-magnesium andesites. Three discrimination plots were used to identify boninite type rocks in the study area. They include the  $\text{MgO-SiO}_2$ ,  $\text{MgO-TiO}_2$ , and  $\text{Si}_8\text{-Ti}_8$  discrimination plots. To obtain this data, manipulation to a 100% volatile-free foundation and a partition of iron, ferrous ( $\text{FeO}$ ) and ferric ( $\text{Fe}_2\text{O}_3$ ) oxides totalling to 100% (Pearce and Reagan, 2019) was needed. Samples were then classified based on their location on these plots. A three-stage process of refining the rock types for each sample was conducted as follows. The first stage was plotting the samples in the revised  $\text{MgO-SiO}_2$  discrimination plot from Pearce and Robinson (2010) (Fig. 2.8B). The second stage was plotting the samples on the  $\text{MgO-TiO}_2$  discrimination plot (Fig. 2.8C). The third stage was the plotting of the samples on the  $\text{Si}_8\text{-Ti}_8$  diagram (Fig. 2.8D) as a requirement of the definition of a boninite as previously stated in Chapter 2. These values were calculated using the formulae from Pearce and Reagan (2019). For the  $\text{Si}_8$  values, using the  $\text{MgO-SiO}_2$  discrimination plot the  $\text{Si}_8$  value can be determined by the downward extrapolation to the  $\text{MgO} = 8$  line, using the slope of the bounding lines (Pearce and Reagan 2019):

$$\text{Si}_8 = \frac{\text{SiO}_2 + (\text{MgO} - 8)}{3.83} \text{ for } \text{MgO} > 8$$

For the  $\text{Ti}_8$  values, using the  $\text{MgO-SiO}_2$  discrimination plot, the  $\text{Ti}_8$  value can be determined by projecting from olivine to the  $\text{MgO} = 8$  line using the following equation (Pearce and Reagan 2019):

$$Ti8 = \frac{42TiO_2}{(50 - MgO)} \text{ for } MgO > 8$$

## Geochemical Variation Diagrams

Harker variation diagrams were used to interpret major element trends within the four study areas. The Gullewa and Weld Range localities were used as reference samples for the west and north Murchison respectively. Single major element Harker diagrams that were used include,  $Al_2O_3$ ,  $P_2O_5$ ,  $TiO_2$ ,  $Fe_2O_3$ ,  $MgO$ , and  $Mg\#$  ( $Mg / [Mg + Fe] \times 100$ ) all plotted against  $SiO_2$ . Compatible element variation plots were created as well, these included,  $Cr$  vs  $Ni$ ,  $V$  vs  $Ni$  and  $V$  vs  $Ti$ . Incompatible element variation plots were also used in this analysis including,  $Nb$ ,  $Zr$ ,  $U$ ,  $Th/Nb$  all plotted against  $Th$ .

## Primitive Mantle Plots

Geochemical groups were created based on their locations in the Yalgoo (Ivanic et al, 2015), Ninghan (Ivanic, 2018), and Perenjori (GSWA, 1983) maps (Fig. 2.6 and 2.7). The 1983 Perenjori map was used due to no updated detailed geological map of the Mt. Mulgine area. The samples were located in 4 locations, Yalgoo, Yeoh Hills, Mt. Mulgine, and Warriedar. Stratigraphical group or formation type data was extrapolated from these maps and GeoView (2019) for each sample.

Further refinement of geochemical groups was completed with the analysis of normalised primitive mantle plots. These plots were created based on the ordering of incompatible and compatible elements by Sun and McDonough (1989). Increasing incompatibility of elements to the left and increasing compatibility of elements to the right. Analysis of trends in these plots was conducted with subdivision into similar geochemical groups. Intergroup comparisons of these plots were conducted, relating groups of different areas. Further analysis of specific trends was conducted, for

example elements such as niobium (Nb), zirconium (Zr), and hafnium (Hf) showed significant trends presented in Chapter 5.

## Chapter 4 Petrography Results

Petrographic analysis was conducted on 43 samples. All samples have undergone greenschist to amphibolite grade metamorphism. This implies maximum pressure and temperature conditions of 10 kb and 700 °C (Mottana et al., 1978). Primary textures and mineral phases are generally obscured due to this metamorphism, however, some relict textures such as spinifex and cumulus texture can be observed in many samples. This contrasts with the textural preservation in the northern Murchison, where textures are locally well-preserved due to lower metamorphic prehnite-pumpellyite to greenschist grade conditions noted by Lowery et al. (2017) and Wyman and Kerrich (2012).

In some cases, distinct primary petrographic features are observed at a single locality, however recurring textures can be observed at multiple localities in volcanic units that are classified as belonging to the Norie or Polelle Groups. These recurring petrographic groups are referenced to the geochemical sub-types described in later chapters. The petrographic groups include altered volcanics exhibiting primary extrusive igneous textures, such as spinifex or porphyritic texture, and intrusive samples with cumulate texture. Cumulous textures cannot be used to understand the original magma compositions. This is due to the buildup of concentrations in a mineral such as the accumulation of olivine crystals at the base of the magma.

Strong alteration in some samples can be an indicator for the usefulness of the geochemistry discussed in later chapters, this can be seen through the various carbonate veins (300 µm x 1100 µm) which are a common feature of sample FFE1 (Fig. 4.1).

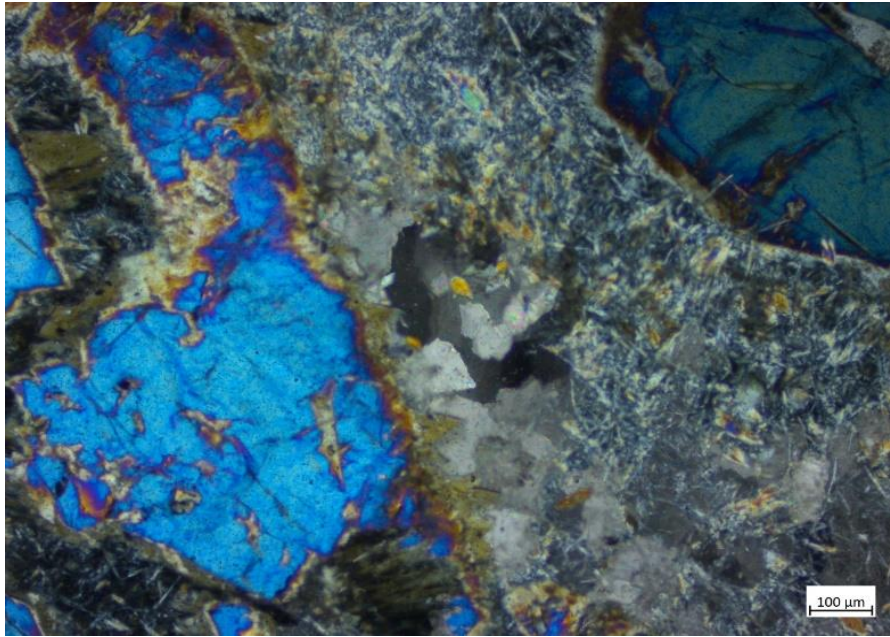


*Figure 4.1: Carbonate vein (centre) in sample FFE1 (cross polarized light).*

## Mt. Mulgine

Stratigraphic units and coeval intrusions in the Mt. Mulgine area are classified on both the Perenjori (GSWA, 1983) and Ninghan (Ivanic, 2018) maps. The samples contain Polelle group (Meekatharra Formation and Warriedar Suite) rocks. Rock types in this group include, amygdaloidal basalt with quartz filled vesicles, pyroxene spinifex-textured basalt, metamorphosed peridotite (with relict cumulate textures), and tremolite-chlorite(-talc) schist. Most samples in this area are basalt/andesite, with subhedral grains of interlocking pyroxene/olivine replaced by secondary amphibole. Feldspar grains are typically anhedral acting as a fine-grained groundmass but in some samples show subhedral to euhedral grains. Other textures and features that are ascribed to one or more rocks in this area are described below.

Petrographic analysis was conducted on 12 samples from the Mt. Mulgine locality. Many of the samples display similar metamorphic textures. Primary (igneous) spinifex texture, however, was preserved in one sample from this locality (Fig. 4.2). The chemical composition of this sample is equivalent to all other samples (Chapter 5) and all samples are therefore considered to be volcanic. Random dendritic pyroxenes have been replaced by amphibole, the large spinifex blades are elongated with an average blade length of 2900  $\mu\text{m}$ . Later spinifex blades are smaller (500  $\mu\text{m}$ ) and fill the interstices (spaces) between the earlier large blades showing multiple generations of spinifex blades as seen in Figure 4.2.

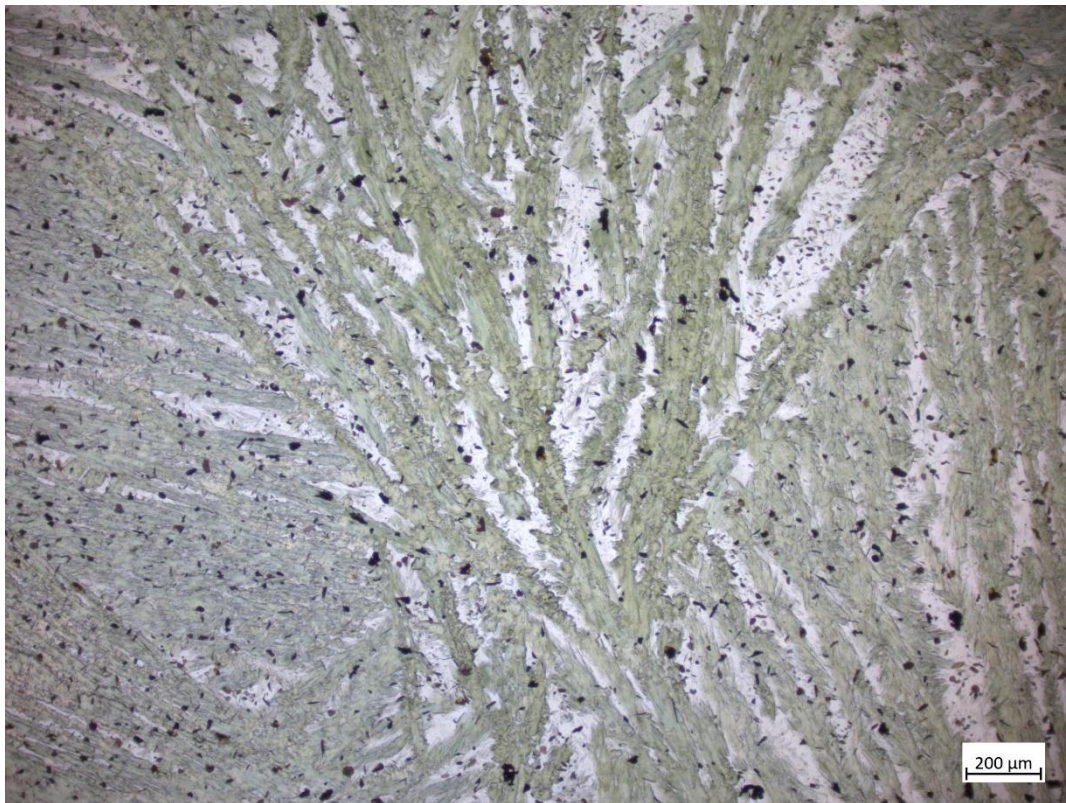


*Figure 4.2: Spinifex texture of random dendritic pyroxenes replaced by amphibole in sample MG14A (plane polarized light).*

The predominant texture in the Mt. Mulgine samples includes pseudomorphs of cruciform to irregular polysynthetic twins of primary pyroxene replaced by subhedral amphibole (average 60%), up to ~2400 by 150  $\mu\text{m}$ , in a fine-grained quartz-feldspar groundmass (Fig. 4.3). This overlapping texture can be compared to the clinoenstatite textures seen in the lower metamorphic grade Pölelle Group boninites reported by

Wyman and Kerrich (2012) and Eocene examples (Ohnenstetter and Brown, 1992), where the samples are lower-grade and therefore primary textures are well preserved. This texture is also seen in all other localities.

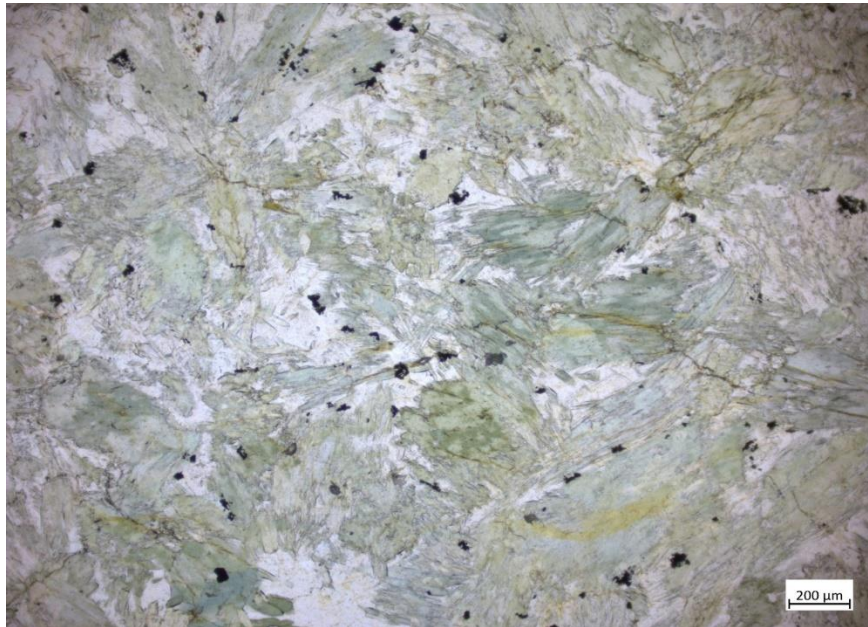


**Figure 4.3:** Pseudomorphs of cruciform to irregular polysynthetic twins of primary pyroxene replaced by subhedral amphibole in a fine-grained quartz-feldspar groundmass in sample MG11 (plane polarized light). The cross-type twins are typical of clinoenstatite in boninites (see text).

Secondary characteristics of this amphibole texture include acicular terminations corresponding to outward growth during metamorphism. Opaque minerals of varying sizes ( $< 200 \mu\text{m}$ ) are present in the majority of samples. These opaques were identified as predominantly magnetite and pyrite. Secondary  $\text{TiO}_2$  (leucoxene) was also observed in samples MG1 and MG7 (Fig. 4.4). Some occurrences of secondary biotite were also observed.

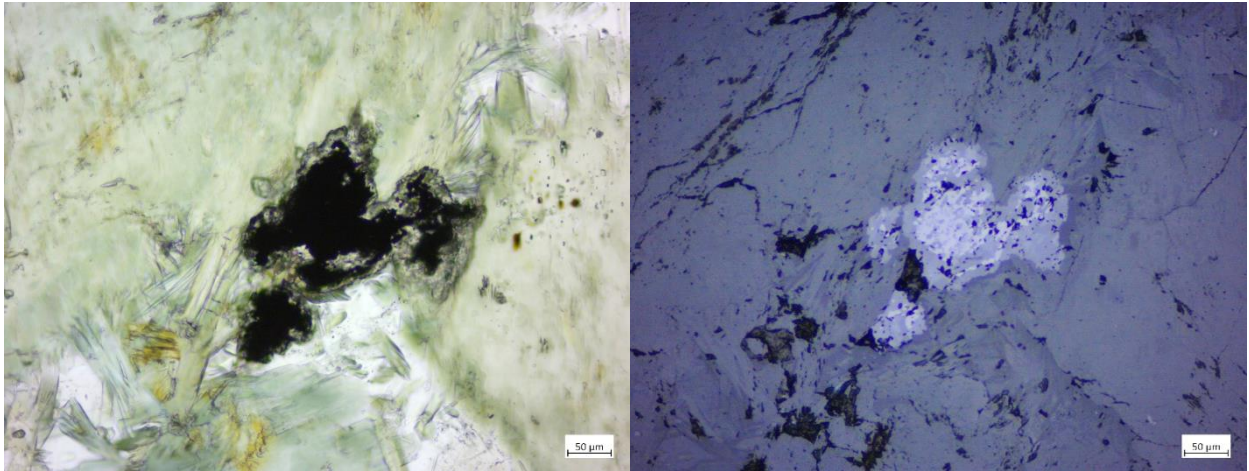


*Figure 4.4: Secondary TiO<sub>2</sub> (leucoxene) in sample MG1. Left in plane polarized light and right in reflected light.*

## Yeoh Hills

Stratigraphic units and coeval intrusions in the Yeoh Hills area are classified on the Ninghan (Ivanic, 2018) map. The samples in this study include Polelle (Warriedar Suite) and Norie (Singleton Formation) group rocks. Rock types in these groups include, metabasalt, metamorphosed pillowed basalt and metamorphosed dolerite. Most samples in this area are microcrystalline basalts composed of subhedral to euhedral pyroxene/olivine replaced by secondary amphibole with a quartz-feldspar groundmass. Other textures and features that are ascribed to one or more rocks in this area are described below.

Petrographic analysis was conducted on 9 samples from the Yeoh Hills locality. Samples from this locality displayed little variation in texture. Most samples are dominated by masses of fine-grained ( $< 300 \mu\text{m}$ ) subhedral amphibole but contain globular or spherical  $1200 \mu\text{m}$  features. This texture can be subtle and is interpreted as relict varioles that are mineralogically similar to the surrounding rock (Fig. 4.5). These varioles are similar to Paleoproterozoic examples described by Humbert et al. (2018). The origin of varioles has been thoroughly debated with the two main theories of, undercooling through sub-aqueous deposition (Humbert et al. 2018; Fowler et al. 2002) and formation before and during cooling by liquid immiscibility (Cawthorn et al. 1979). Another texture for this locality includes the sub-volcanic texture seen in sample YH24. These coarser rocks may contain cruciform pyroxene pseudomorphs similar to the those observed boninite volcanic flows but also found in coarse-grained rocks in the Mt. Mulgine area.

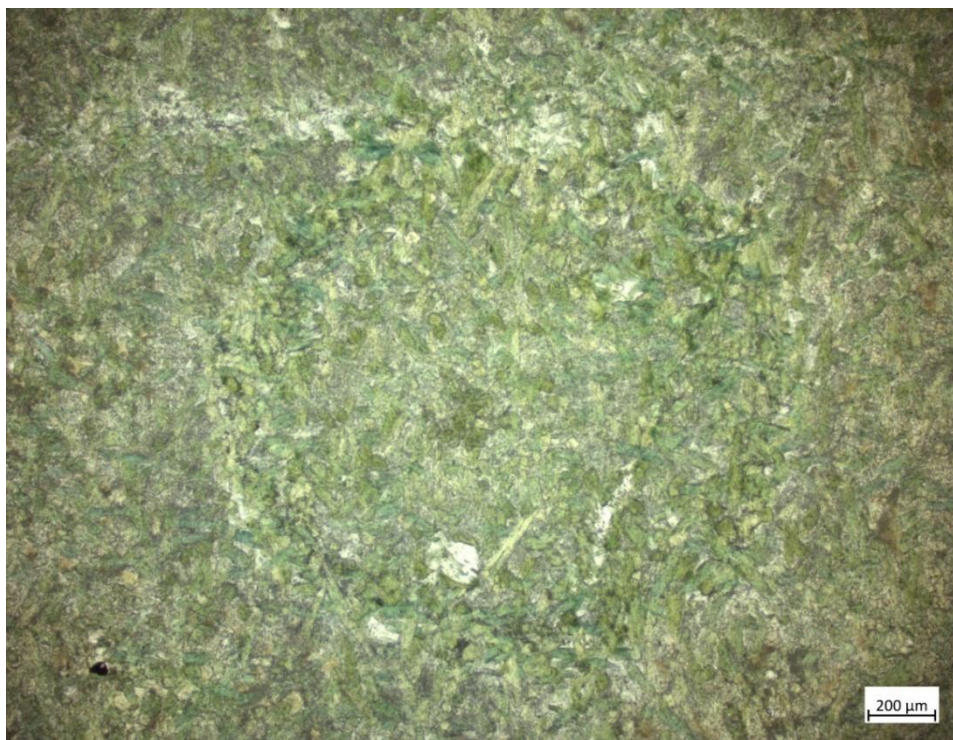


*Figure 4.5: Variole forming a globular geometry in sample YH15 (plane polarized light).*

Quartz and feldspar occur in vesicles ( $1300 \times 1000 \mu\text{m}$ ) in basaltic sample YH3B. A rare texture for this entire study is the presence of moderate shearing and deformational fabric identified in sample YH20 (Fig. 4.6). This sample contains the

same mineral assemblage as other Yeoh Hills samples, which includes mainly secondary amphibole (80 %) and a quartz-feldspar and grey-coloured fine-grained groundmass. Euhedral secondary amphibole porphyroblasts, with second order birefringence, overprint the fabric of the fine groundmass at random orientations, and therefore postdate development of the fabric (Fig. 4.6). Opaque minerals seen in this sample align with the fabric direction, which includes lenticular areas (~400 x 200  $\mu\text{m}$ ) consisting of a feldspar-rich groundmass.

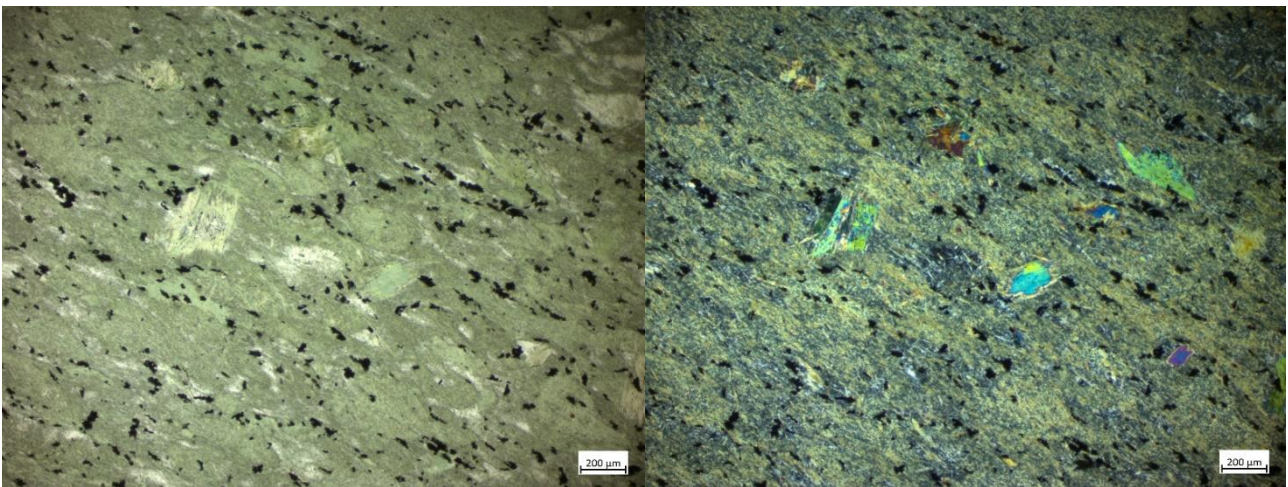


**Figure 4.6:** Moderate shearing and deformational fabric in sample YH20 (left in plane polarized light, right in cross polarized light).

Samples YH19A, YH19B and YH19C are relatively coarse-grained masses of interlocking amphiboles (< 500  $\mu\text{m}$ ) with minor patches of feldspathic groundmass. Accessory amounts of olivine are present as large (average 2400  $\mu\text{m}$  in diameter) crystals. The olivines have been altered, but the original crystal shape is somewhat preserved as seen in Figure 4.7. Given the size of the crystals, they appear to have been derived from a coarse-grained crystal within the magma plumbing system.

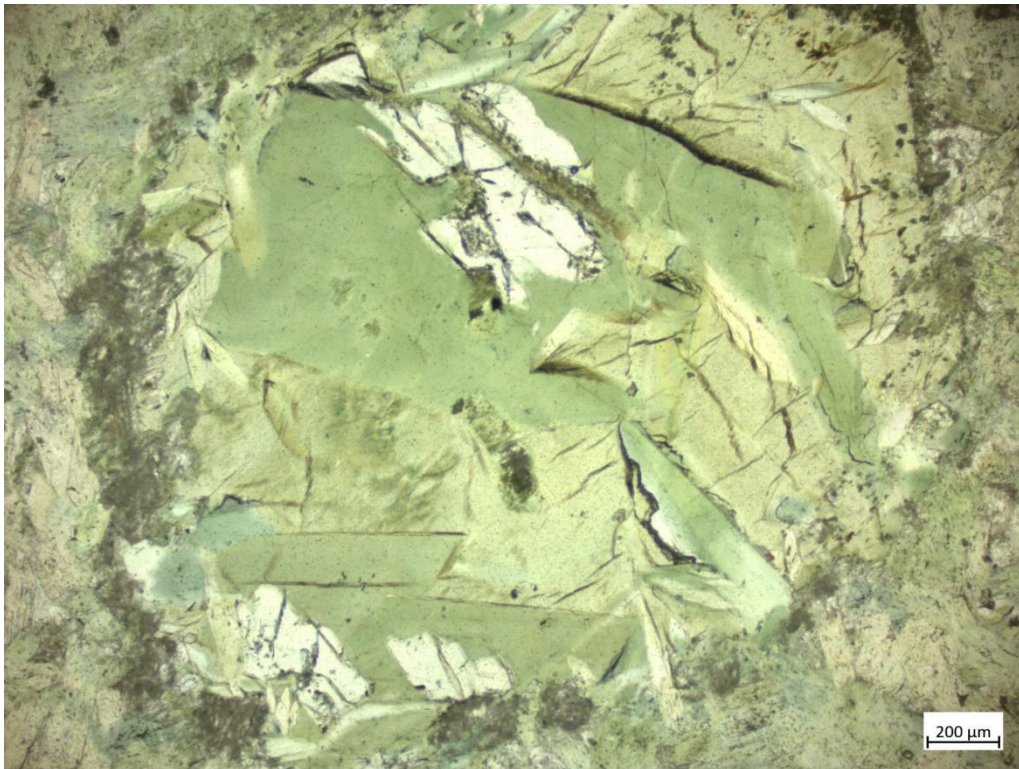


*Figure 4.7: Alteration of a primary, euhedral, olivine to amphibole. The original crystal edges are best preserved on the upper right side of the crystal. Sample YH19C (plane polarized light).*

## Warriedar

Stratigraphic units and coeval intrusions in the Warriedar area are defined on the Ninghan (Ivanic 2018) map. Study samples include Polelle (Meekatharra Formation and Warriedar Suite) and Norie (Singleton Formation) group rocks and a non-assigned group consisting of the three Fields Find East samples. Rock types in these groups include, metamorphosed locally pillowed basalt, metamorphosed gabbro, metamorphosed massive to weakly foliated pillowed basalt, and meta-ultramafic intrusive rock. Most samples in this area are medium grained gabbros composed of

subhedral to euhedral pyroxene/olivine replaced by secondary amphibole with a quartz-feldspar groundmass. Basalt/andesite is also present with anhedral phenocrysts of primary pyroxene and a groundmass of quartz-feldspar. Other textures and features that are ascribed to one or more rocks in this area are described below.

Petrographic analysis was conducted on 10 samples from the area of the Fields Find Igneous Complex in the Warriedar greenstone belt, which is described on the Ninghan 2018 1:100,000 Map (Ivanic, 2018). Samples FFE1, FFE2, and FFE3 are located further



*Figure 4.8: Typical texture in the Warriedar area, with amphibole pseudomorphs of coarse primary pyroxenes (green) and a feldspathic groundmass (white). Sample WR5 is pictured in plane polarized light.*

northeast than the other samples taken in this belt. The FEE samples (Fields Find East) correspond to pyroxenite and peridotite layers within a thick differentiated sill. The remaining samples are generally composed of 70% subhedral to euhedral amphibole (< 600  $\mu\text{m}$  in length) with a quartz-feldspar groundmass. The predominate texture in this area is characterised by abundant amphibole pseudomorphs of coarse (< 300  $\mu\text{m}$ ) subhedral to euhedral pyroxenes in an altered feldspathic groundmass, pictured on Figure 4.8. The texture probably represents shallow intrusive rocks or possibly thick flows and, in some cases, includes accumulated phenocrysts that settled toward the bottom of the magma.

A cumulous texture is seen in sample FFE3, where olivine crystals (average ~600  $\mu\text{m}$ ) have accumulated and altered to talc due to the addition of water and carbon dioxide ( $\text{CO}_2$ ) (Fig. 4.9).

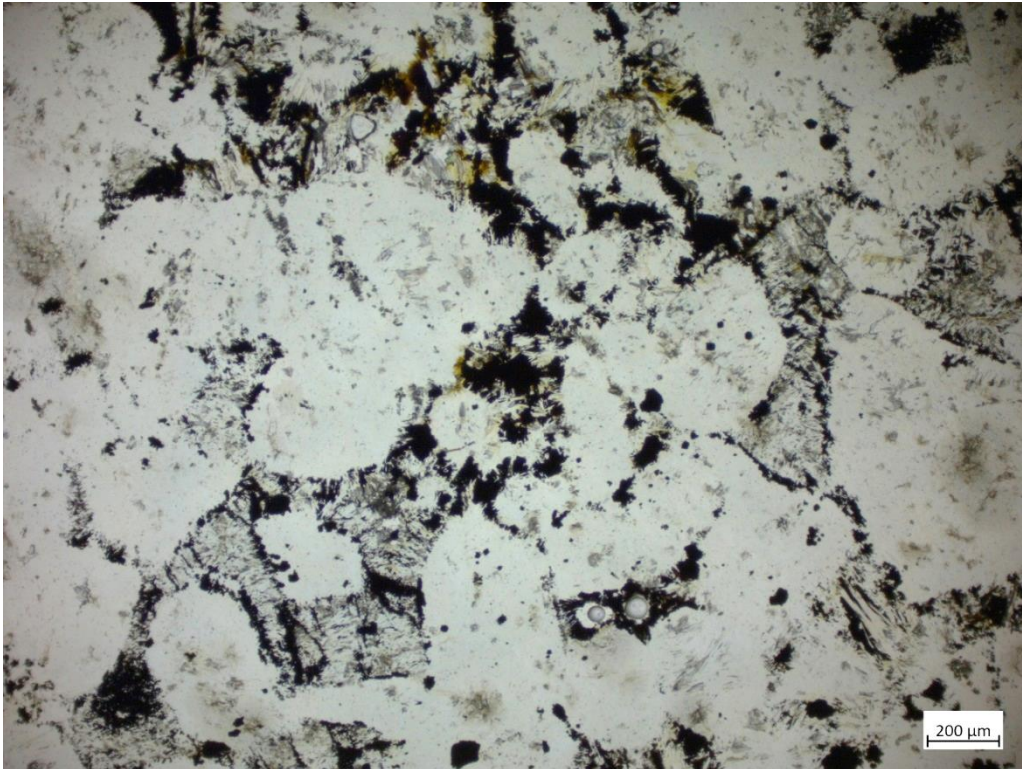


*Figure 4.9: Altered olivine cumulate; olivine crystals have been altered to talc in sample FFE3 (plane polarized light).*

Other features in this locality can include twinning of clinopyroxene (simple twins), in sample WR10. Opaques are common throughout this area with relict cleavage of primary amphiboles being preserved by the replacement of oxides as seen in reflected light on Figure. 4.10. Secondary amphibole typically pseudomorphs pyroxene, leaving a reaction rim related to compositional differences in the original zoned pyroxenes (Fig. 4.11).

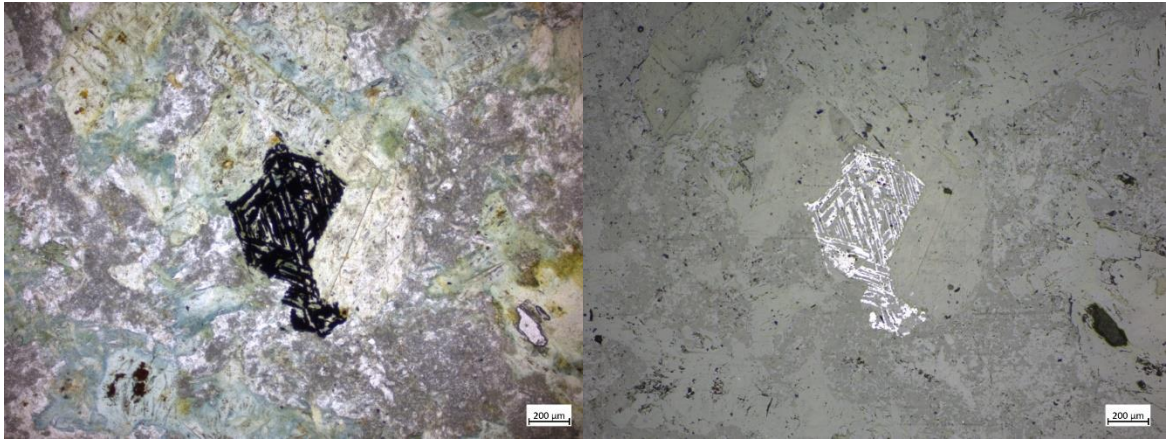


**Figure 4.10:** Amphibole cleavage preserved by an oxide in sample WR10 (left in plane polarized light, right in reflected light).

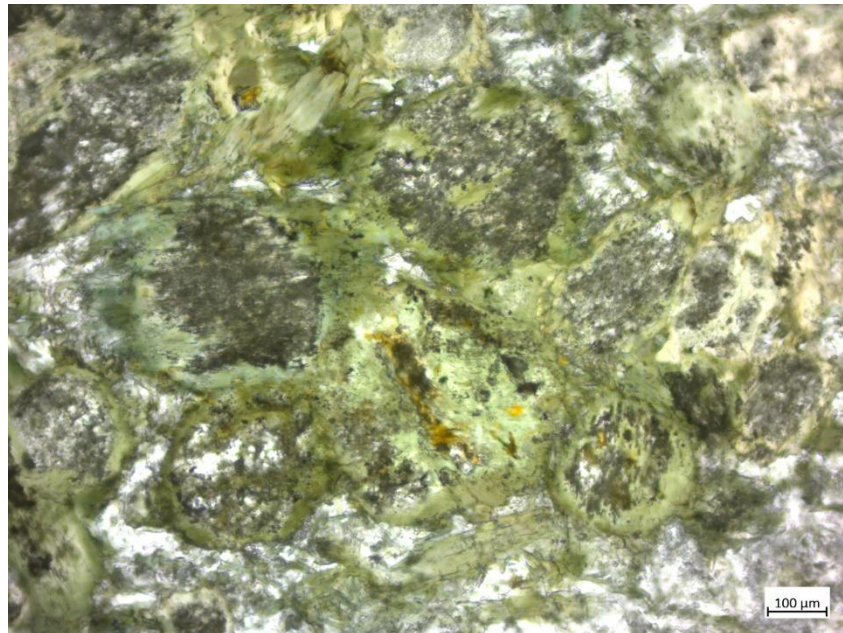


**Figure 4.11:** Alteration rims from amphibole variably replacing zoned pyroxene crystals in sample WR9 (plane polarized light).

## Yalgoo

Stratigraphic units and coeval intrusions in the Yalgoo area are classified on the Ninghan (Ivanic, 2018) map. The samples contain Polelle (Mugs Luck Basalt Member and Carlaminda “Komatiite” Member) group rocks. Rock types in this group include, locally metamorphosed pyroxene spinifex-textured basalt and purported platy olivine spinifex-textured komatiite with flows of pyroxene spinifex-textured basalt. This

study area is located further north to the other localities and samples are situated in the Noongal anticline. Most samples in this area are spinifex textured basalts composed of platy pyroxene replaced by secondary amphibole with a quartz-feldspar groundmass. Other textures and features that are ascribed to one or more rocks in this area are described below.

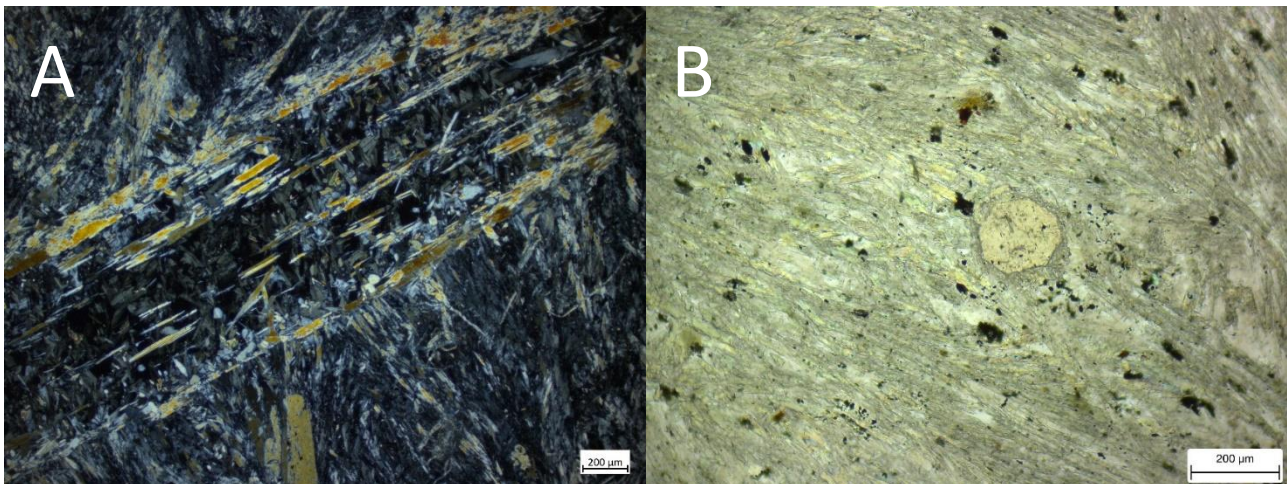


**Figure 4.12:** Left image shows inner and outer rims in an altered pyroxene in sample YL18 (cross polarized light). Right image shows a secondary hornblende crystal with a reaction rim of fine-grained silicates in sample YL18 (plane polarized light).

The main texture observed in this area through the 12 petrographically analysed samples, includes fine bladed spinifex (< 200 µm in width), seen in 9 samples (Fig. 4.12A). The blades display a large variation in sizes, thin long blades (~50 µm x ~3000 µm) to less common short but wider crystals



**Figure 4.13:** Fine bladed spinifex in sample YL8 (plane polarized light).

(~400 µm x 1100 µm). The samples contain variable amounts of secondary biotite (< 10 %). A special case, sample YL18, displays altered pyroxene spinifex texture with larger pyroxenes displaying zones, where the inner and outer sections are altered at different times (Fig. 4.13). Finer grains occur in the centre as elongated acicular grains, where

twinning is also preserved. A unique feature for this study area is the presence of secondary hornblende crystals with a reaction rim of fine-grained silicates (Fig. 4.12B). This feature is seen in YL17 but is less defined due overprinting of an alteration texture. Some samples (YL11, YL12) also display secondary  $\text{TiO}_2$  (leucoxene) as seen in Figure 4.4 in the Mt. Mulgine samples.

Another texture that was observed is adcumulate texture, with  $<1200 \mu\text{m}$  sized crystals. Samples showing this texture are altered to talc (sample 225152), however they are not as altered as the olivine cumulate, FFE3. Some spaces between crystals are filled with a dark fine-grained liquid, hence not allowing enough time to further crystallise these pockets and have been accumulated (Fig. 4.14).



*Figure 4.14: Filling in of spaces in a triangular shape in sample 225152 (plane polarized light).*

The last texture seen in this locality consists of pseudomorphs of cruciform to irregular polysynthetic twins of primary pyroxene replaced by subhedral amphibole (average 70%), in a fine-grained quartz-feldspar groundmass. Sample 225145 displays this texture and includes quartz-feldspar veins with an average length of 1400  $\mu\text{m}$  and width of 100  $\mu\text{m}$ . Sample YL11 shows a unique feature,



*Figure 4.15: Transition from cruciform texture (left) to a gabbroitic texture (right) in sample YL11 (plane polarized light).*

displaying the cruciform texture, with random gabbroitic globular features. The transition between these two areas can indicate a shallow intrusive origin (gabbroitic) or fluid interaction, this distinction is shown in Figure 4.15. Another indicator of an intrusive origin is the granophyric texture in a coarse-grained matrix with accumulated crystals depicted in sample YL6 (Fig. 4.16).

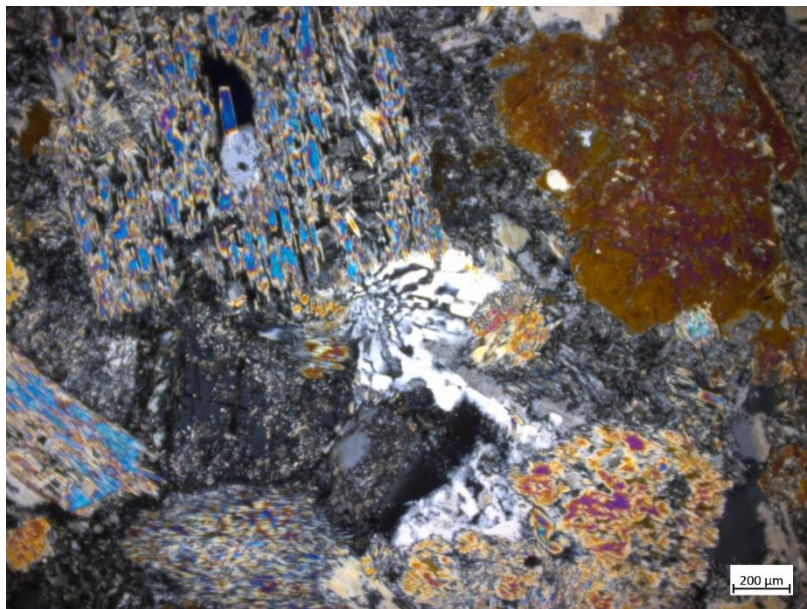


*Figure 4.16: Granophyric texture in a coarse-grained matrix in sample YL6 (cross polarized light).*

## Chapter 5 Whole Rock Geochemical Results

Ultramafic-mafic to intermediate samples were analysed by the ALS procedures described in Chapter 3, which provided the study with the whole-rock major and trace element geochemical data. The data from this study has been included in Appendix 1. To analyse these data, discrimination plots, x-y plots, and normalised primitive mantle plots were used to classify rock types, such as the identification of potential boninites and komatiites, based on accepted criteria. Caution, however, must be used when geochemically defining a sample's rock type, given the effects of metamorphism, alteration and crystal fractionation. For example, petrographic observations for a sample may indicate that it contains cumulate mafic minerals and is not an ultramafic flow.

Generally, Warriedar samples displayed the highest variability in the x-y plots of the major elements (Harker variation diagrams), with SiO<sub>2</sub> ranging from 42 wt% up to about 48 wt%. High MgO contents extend to high values, greater than 25 wt%, which generally results from crystal fractionation and the formation of cumulate-bearing intrusive samples in the area. These chemical variations are also seen on the primitive mantle plots where the contents of incompatible trace elements vary with the degree of prior crystal fractionation undergone by the magma. Multiple distinct magma types also occur in particular study areas as indicated partly by distinct trends on Harker variation diagrams and normalized trace element plots. Four subgroups are identified at Warriedar. Samples from the other study areas generally extend over a range of SiO<sub>2</sub> contents between 48 and 58 wt%. Yalgoo samples had the least variation in all x-y plots, with similar values in the Harker diagrams or being a part of the same continuum in the incompatible element plots. However, in the normalised primitive mantle plots, four subgroups were defined showing the magmatic differences within the area. Mt. Mulgine samples tended to have similar values on the Harker diagrams

with an exception of one outlier from the WACHEM database (sample 198294) identifying as a gabbro. The normalised primitive mantle plots for this area were very consistent, with all samples falling into one group. Yeoh Hills samples showed some fractionation-related variation in the Harker diagrams and on the incompatible element x-y plots they defined a consistent trend. In the normalised primitive mantle plots, these samples also define a single group. Further detail in the analysis of the whole rock geochemical data is given below.

### Boninite Discrimination Plots

Classification schemes for the categorisation of many Archean rock types have recently been refined with the publication of a new boninite classification scheme by Pearce and Reagan (2019). This scheme presents two discrimination plots that define the boundaries for basalts, picrites, low-Si boninites (LSB), high-Si boninites (HSB), high-Mg andesites (HMA), high-Mg andesites and basalt-andesite-dacite-rhyolite (HMA & BADR), basaltic andesite (BA), and komatiites.

Samples from this study were first categorised using the MgO-SiO<sub>2</sub> discrimination plot (Fig. 5.1). This plot was used to satisfy the SiO<sub>2</sub> > 52 wt% requirement of the IUGS (International Union of Geological Sciences) criteria. Mt. Mulgine samples displayed an LSB-basalt-HMA trend, which exhibited the least MgO and SiO<sub>2</sub> variation among the four localities. Yeoh Hills samples plot as a cluster with samples across the LSB, basalt, BA, and HMA fields. This is likely due to the fractionation of clinopyroxene, since that mineral was observed in thin section and the boninite boundaries within the discrimination plot are defined based on olivine fractionation trends. Warriedar samples displayed at least two trends, where the altered cumulate sample FFE2 is a low-Si outlier in the basalt field. Other Warriedar samples with MgO above ~ 18 wt.% also contain cumulate olivine and define a trend for this locality that lies near the

komatiite-picrite-basalt boundary with the LSB field. The second trend identified is an LSB-HSB-HMA trend. Yalgoo samples displayed an LSB-HSB-HMA trend.

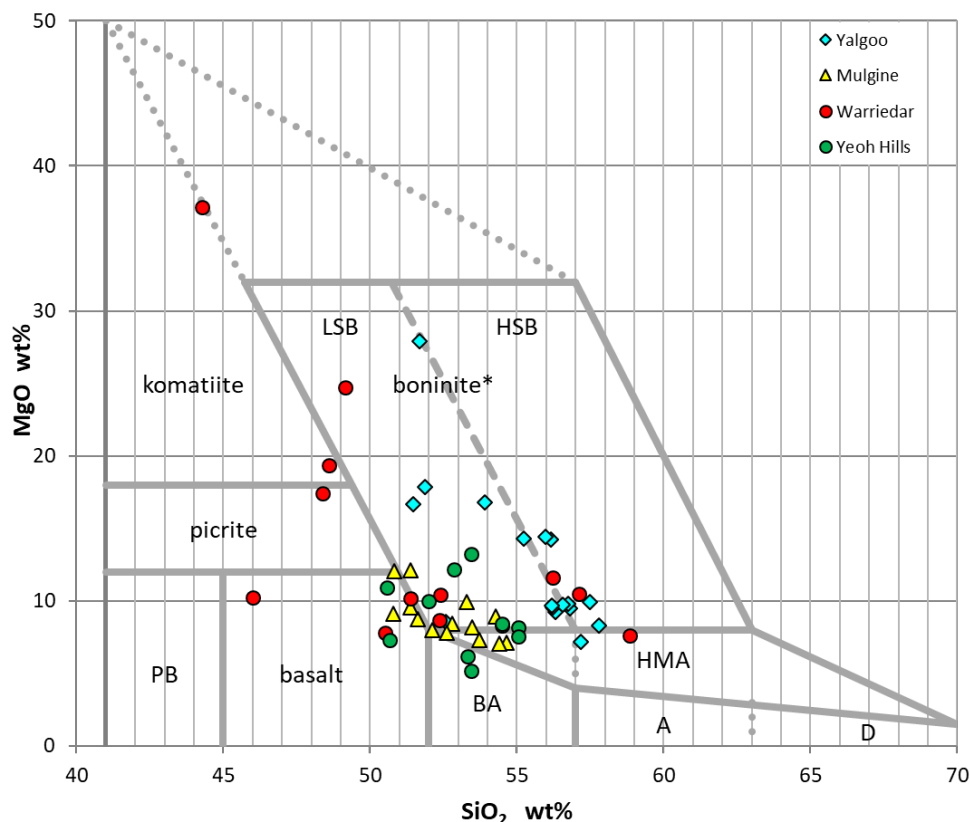


**Figure 5.1:** MgO vs SiO<sub>2</sub> plot after Pearce and Reagan (2019). PB = picro-basalt, LSB = low-Si boninites, HSB = high-Si boninites, HMA = high-Mg andesites, BA = basaltic andesite, A = andesite, D = dacite.

Samples were then further categorised using the Pearce and Reagan (2019) MgO-TiO<sub>2</sub> discrimination plot (Fig. 5.2). This plot was used to satisfy the TiO<sub>2</sub> < 0.5 wt% requirement of the IUGS criteria. Some samples have been excluded from this graph due to TiO<sub>2</sub> values > 1.0 wt%. Mt. Mulgine samples displayed a boninite-basalt-HMA & BADR trend. The MgO-SiO<sub>2</sub> discrimination plot trend was similar to this trend, affirming the identification of 6 boninite samples, MG1, MG11, MG12, MG17, MG24, and YL17. These samples all have Si<sub>8</sub> values of > 52, (apart from sample MG1 with a Si<sub>8</sub> value of 51.83) and Ti<sub>8</sub> values of < 0.5. Yeoh Hills samples displayed a picrite-basalt-HMA & BADR trend. Some samples have been excluded due to the TiO<sub>2</sub> limitation of 1.0 wt%. The Warriedar high-MgO samples define a komatiite-picrite trend, and the second a basalt-HMA & BADR trend. In this plot, two outliers have

been identified, sample WR9 and WR17, this is similar to the previous MgO-SiO<sub>2</sub> plot, with two other outliers being added. Yalgoo samples displayed a fairly linear trend of komatiite-picrite-boninite-basalt, with an HMA & BADR outlier (sample YL14).

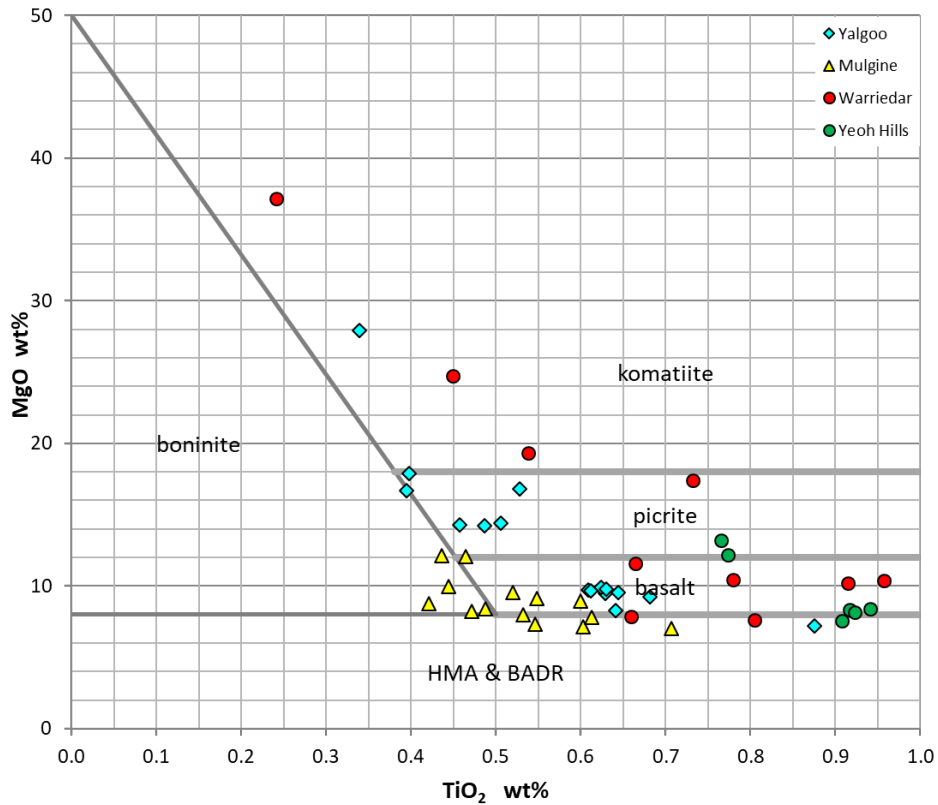


**Figure 5.2:** MgO vs TiO<sub>2</sub> plot after Pearce and Reagan (2019). HMA = high-Mg andesites, BADR = basalt-andesite-dacite-rhyolite.

In the Pearce and Reagan (2019) method, samples that passed both discrimination plots as boninites can be re-classified as either LOTI (low-Ti basalt) if  $Si_8 \leq 52$  and SHMB (siliceous high-Mg basalts) if  $Ti_8 \leq 0.5$  with use of the  $Ti_8$  vs  $Si_8$  plot in Figure 5.3. Re-classification of sample MG1, using the  $Ti_8$ - $Si_8$  plot, to the LOTI category. Other identified boninites have passed this stage, leaving 5 boninite samples.

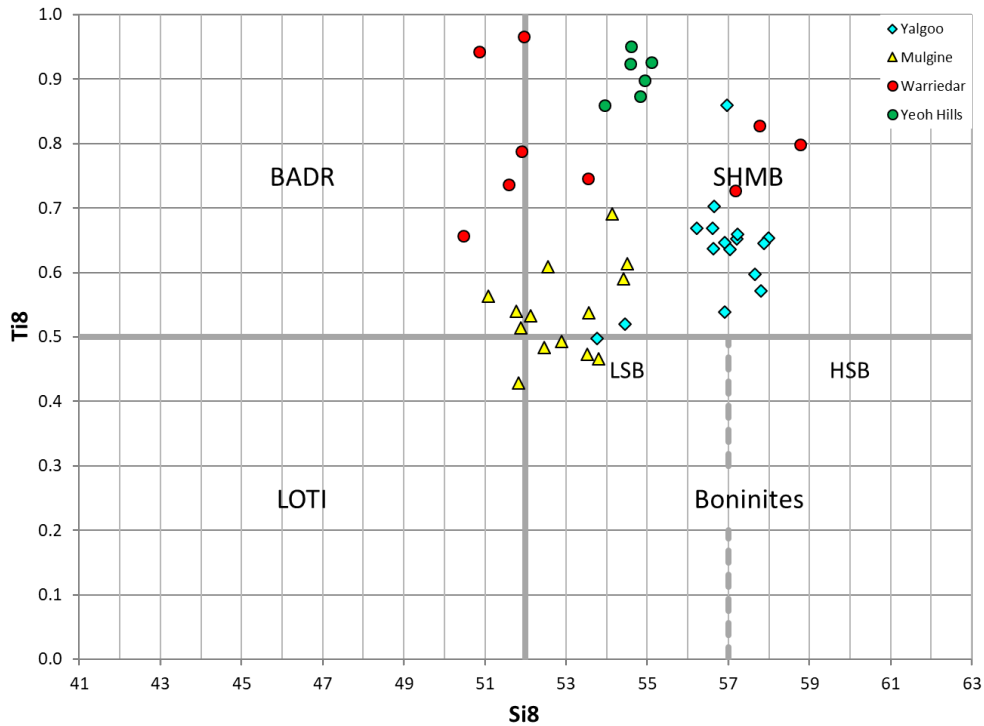


**Figure 5.3:** *Ti8 vs Si8 plot after Pearce and Reagan (2019), refer to chapter 3 for Ti8 and Si8 derivations. BADR = basalt-andesite-dacite-rhyolite, SHMB = siliceous high-Mg basalts, LOTI = low-Ti basalts.*

Samples that passed both the MgO-SiO<sub>2</sub> and MgO-TiO<sub>2</sub> plots as komatiites are not defined as komatiites due to variations in the petrography. Each sample that appeared in the komatiite field was observed or labelled (in the WACHEM database) as having cumulate texture, impacting on their respective MgO levels. For example, this is seen for sample FFE3, where in Chapter 4, displays an olivine cumulate texture.

## Geochemical Variation Diagrams

New whole rock geochemical data from this study was added to the current WACHEM database for the southern Murchison. Samples from the WACHEM database were added to the x-y plots seen in this section, collecting all data for each area. The re-analysed Watkins and Hickman (1990) samples are also included in these diagrams. These samples are then compared to the Gullewa and Weld Range samples from the database, using them as a reference for related rocks in the west and north

Murchison respectively. Included in these plots are samples of volcanic, and intrusive/shallow intrusive origin.

## Major Elements

Harker Diagrams (including element-element, element-ratio, etc.) in Figure 5.4 display the major and trace element compositional variations for sets of whole rock samples. Where trends are present, the plots can help to distinguish between magmatic systems or suggest that spatially separated samples belong to the same or similar systems. Trends on these plots can also help to establish how magmas evolved in terms of mineral fractionation and accumulation.

The  $\text{Al}_2\text{O}_3$  vs  $\text{SiO}_2$  plot in Figure 5.4 shows a weak positive trend since both Al and Si are somewhat incompatible in evolving magmas. Two weak trends are observed for Yeoh Hills and four Warriedar samples are offset from other samples in the group, defined by Yalgoo and Yeoh Hills samples. The Yeoh Hills trends are parallel and, at  $\text{SiO}_2 \sim 52$  wt %, one trend is situated around 15 wt%  $\text{Al}_2\text{O}_3$  and the other at 12 wt%  $\text{Al}_2\text{O}_3$ . Warriedar samples have the most variable trend, this may be partly due to the inclusion of intrusive/shallow intrusive rocks in the sampling area, causing lower values in both  $\text{Al}_2\text{O}_3$  and  $\text{SiO}_2$ .

The  $\text{Fe}_2\text{O}_3$  vs  $\text{SiO}_2$  plot in Figure 5.4 shows a weak negative linear relationship, with  $\text{Fe}_2\text{O}_3$  ranging from 7 to 20 wt%. This negative trend is consistent with the removal of Fe from the melt. Early-forming crystals such as olivine and pyroxene accommodate this element into their structure (Winter, 2014). Variations in the  $\text{Fe}_2\text{O}_3$  vs  $\text{SiO}_2$  trends between locations show Yalgoo having a stronger negative relationship than other areas and Yeoh Hills showing a large  $\text{Fe}_2\text{O}_3$  range to a small  $\text{SiO}_2$  range. This is depicted by the vertical trend around  $\leq 53.03$  wt%  $\text{SiO}_2$ .

The MgO vs SiO<sub>2</sub> plot in Figure 5.4 shows Warriedar samples which extend to MgO contents greater than 20 wt%, implying a komatiite or cumulate-rich sample. The high-Mg samples lie on one of two or three weak negative trends on the plot. Two other possible trends involving Yeoh Hills, also present on the Mg# vs SiO<sub>2</sub> plot are consistent with results from other Harker plots. One of these trends overlaps the trend of Mulgine samples with MgO ranging from 1 to 39 wt%. This general trend can be broken down into three. The first extends from < 39 wt% MgO to < 60 wt% SiO<sub>2</sub>. The second begins around 19 wt% MgO, and the third at around 10 wt% MgO. The general negative trend is consistent with the removal of Mg from the melt. As in the Fe<sub>2</sub>O<sub>3</sub> vs SiO<sub>2</sub> plot, early-forming crystals such as olivine and pyroxene accommodate this element into their structure (Winter, 2014). Hence, olivine accumulation can be inferred for samples with an MgO value of > 15% wt.

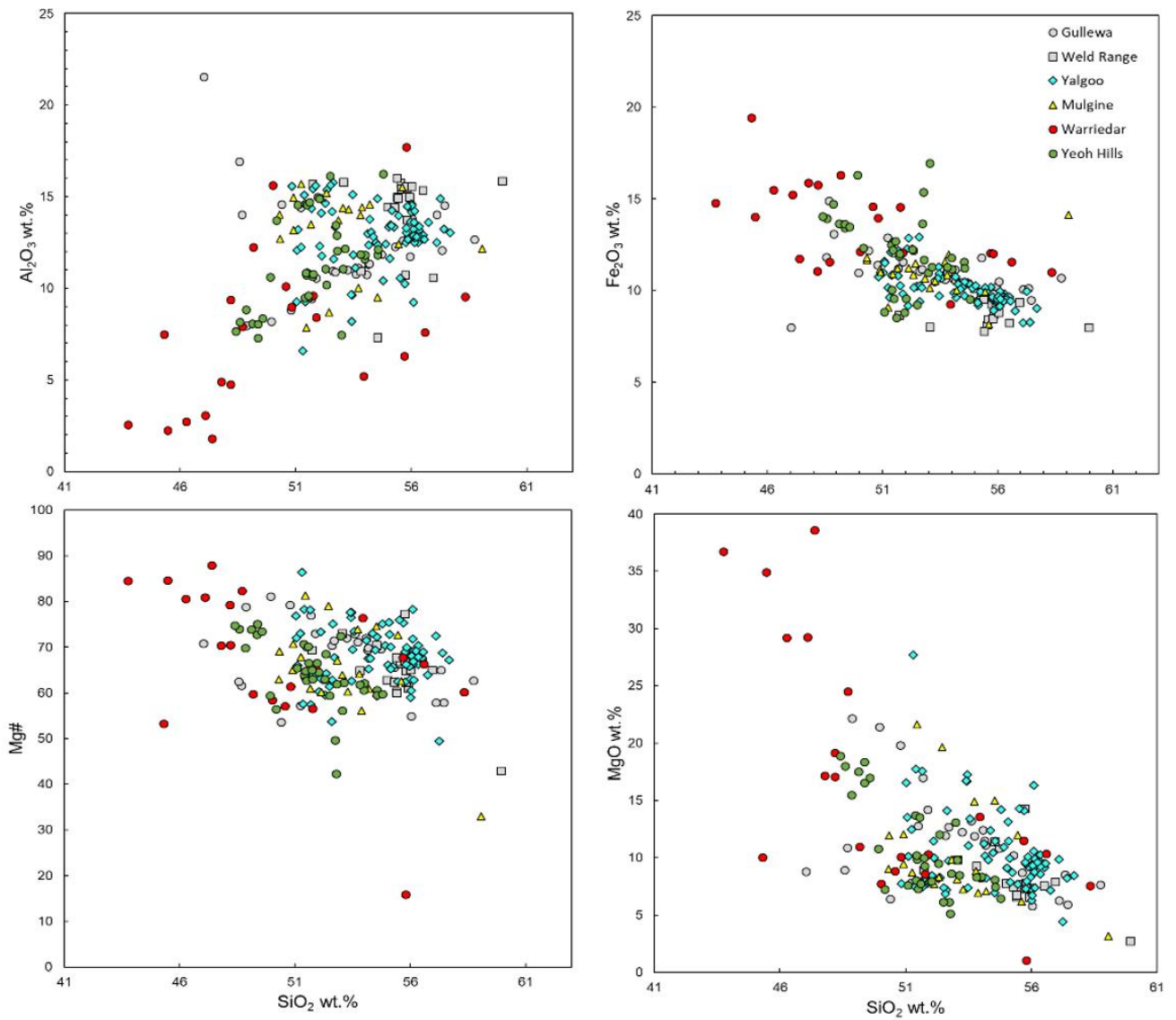
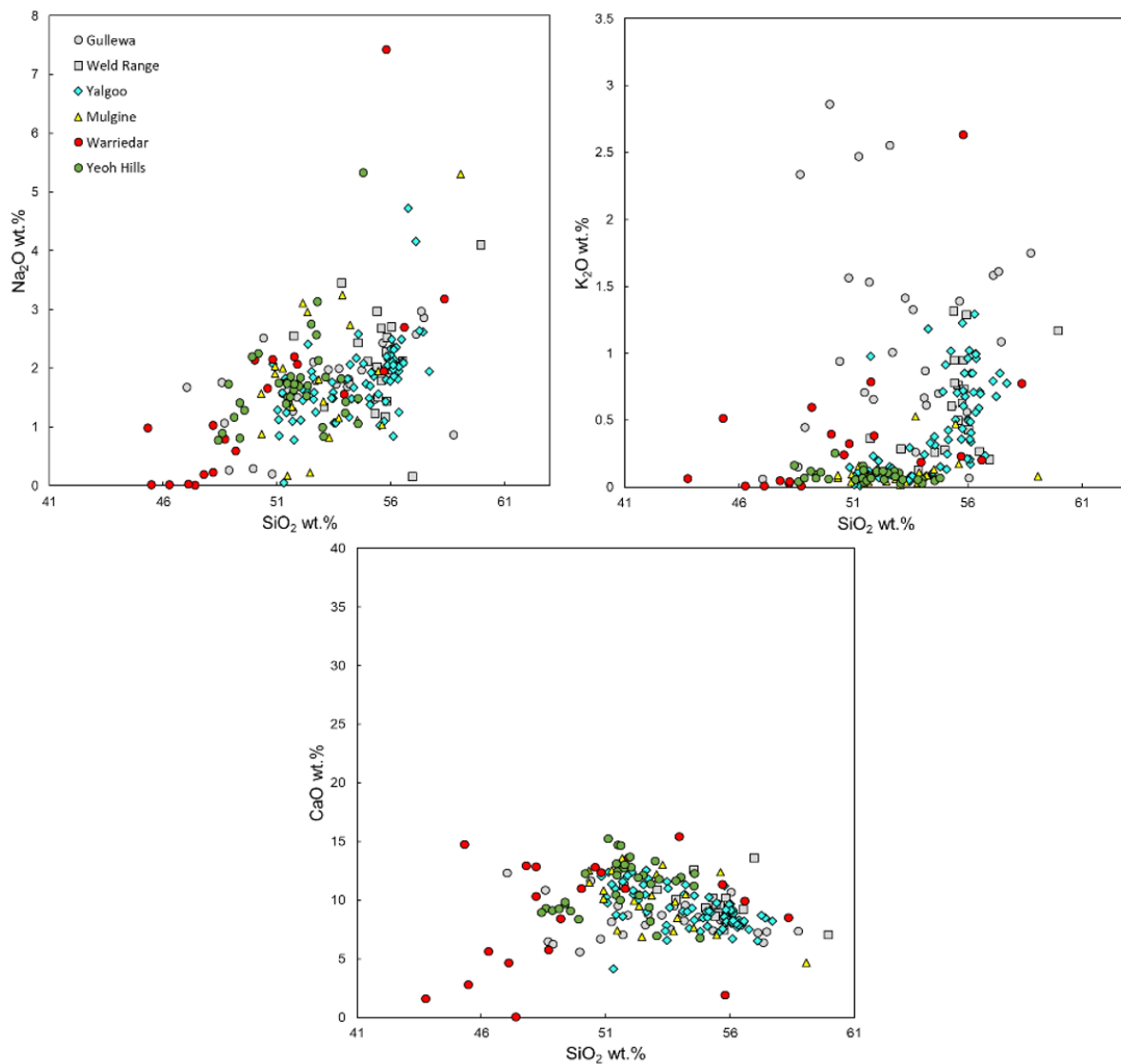


Figure 5.4: Harker variation plots for Yalgoo, Mt. Mulgine, Warriedar, Yeoh Hills, Gullewa and Weld Range.

The oxides CaO, Na<sub>2</sub>O and K<sub>2</sub>O (vs SiO<sub>2</sub>) on Figure 5.5 are susceptible to alteration and disturbance in amphibolite-grade greenstone belts. Nonetheless, the CaO vs SiO<sub>2</sub> Harker plot does show decreasing CaO with increasing silica for Mulgine and Yeoh Hills, as expected in fractionating magmas. Results for Yeoh Hills may be complicated by the presence of two magma types and no clear trend is present for the Warriedar samples. The Na<sub>2</sub>O plot displays a positive overall trend with SiO<sub>2</sub>, although trends for individual areas are poorly developed. The most distinctive feature of the K<sub>2</sub>O Harker plot is the abrupt increase at ~ SiO<sub>2</sub> = 56 wt% for Yalgoo samples compared to Mulgine and Yeoh Hills. Warriedar samples again display considerable scatter.



**Figure 5.5:** Variation plots for Yalgoo, Mt. Mulgine, Warriedar, Yeoh Hills, Gullewa and Weld Range.

The CaO vs MgO plot shows an inflection trend on Figure 5.6, where samples towards the left of the graph show a positive (almost vertical) trend and samples > 10 wt% MgO towards the right of the graph show a negative trend. This inflection may be due to the change of control from olivine to clinopyroxene/plagioclase (Rollinson, 1993). Samples defining the trend from 20 to 40 wt% MgO contain varying amounts of accumulated olivine, based on petrographic observations.

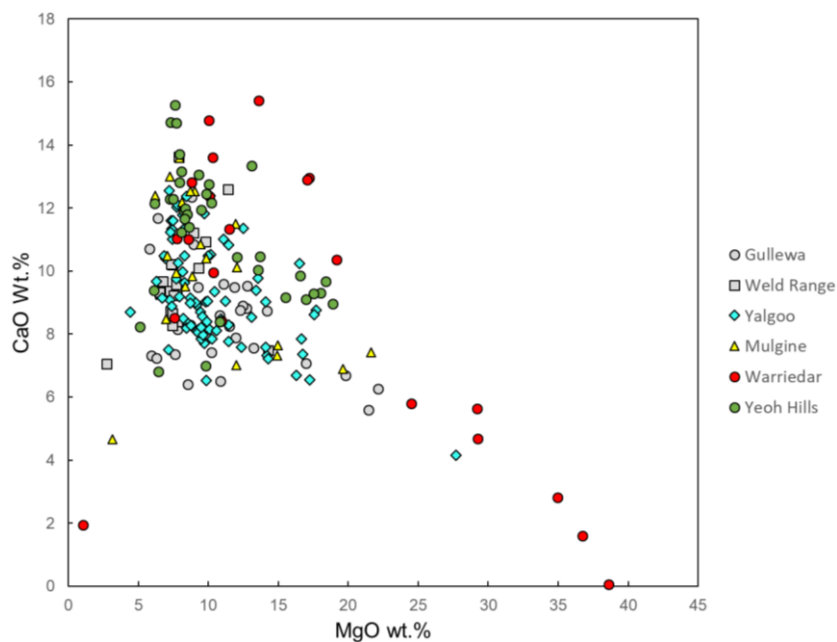


Figure 5.6: CaO vs MgO plot for Yalgoo, Mt. Mulgine, Warriedar, Yeoh Hills, Gullewa and Weld Range.

## Trace Elements

### Compatible Elements

Compatible elements, Cr, Ni, V and Ti show distinct trends with less variation to the incompatible elements. These are shown on Figure 5.7, where four graphs are plotted, Cr vs Ni, V vs Ni, Cr/Ni vs Ni and Sc vs Ni.

The Cr vs Ni plot in Figure 5.7 shows a strong positive trend, where with an increase in Ni values, an increase in Cr occurs. All sample localities follow this trend, with the

exception of five outliers in the Warriedar sample locality. Two separate trends can be defined. Yalgoo and Mt. Mulgine samples define a trend with a maximum Cr value of 3389 ppm. Warriedar and Yeoh Hills samples define a trend with a maximum Cr value of 3186 ppm, where the decrease in Cr/Ni is probably caused by the accumulation of Ni-rich olivine.

The V vs Ni plot in Figure 5.7 shows a weak negative trend, which is evident in all sample localities. Samples are generally clustered with maximum values of 35 ppm in V and 846 ppm in Ni. Samples that were outliers had high Ni values with a maximum value of 2416 ppm, these samples belong to the Warriedar locality, with one Yalgoo sample (1366 ppm Ni).

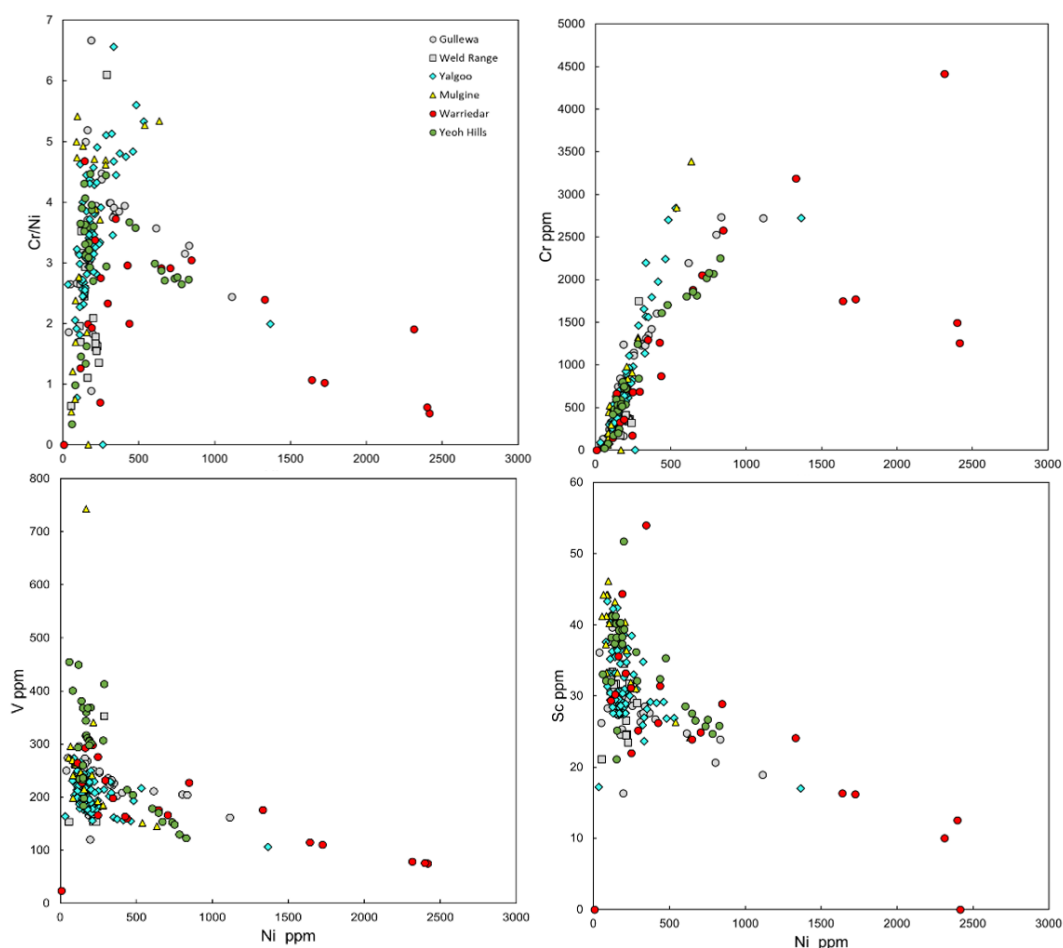


**Figure 5.7:** Compatible elements variation plots against Ni for Yalgoo, Mt. Mulgine, Warriedar, Yeoh Hills, Gullewa and Weld Range.

## Incompatible Elements

The highly incompatible elements also known as the high field strength (HFS) elements, U, Th, and Nb show distinct trends on Figure 5.8.

The U vs Th plot in Figure 5.8 shows a strong positive linear relationship. However, a small number of outliers occur in the Yalgoo group with a variety of both high-Th and high-U values. In addition, one sample from Mt. Mulgine with a higher Th value than its corresponding U value is specified as an outlier. These outliers are somewhat exempt to the co-variance in the U and Th values in each area.

The Th/Nb vs Th plot in Figure 5.8 shows an increasing trend with a plateau at  $< 1.5$  Th/Nb, meaning that as Th (x-axis) increases in Yalgoo, and other samples such as five Mt. Mulgine samples and two Yeoh Hills samples, the Th/Nb values are relatively equivalent. However, with low levels of Th  $< 1$  ppm, the Th/Nb ratio shows an increasing trend until it reaches  $> 0.5$ . This trend is dominated by Yeoh Hills, Warriedar and Mt Mulgine samples.

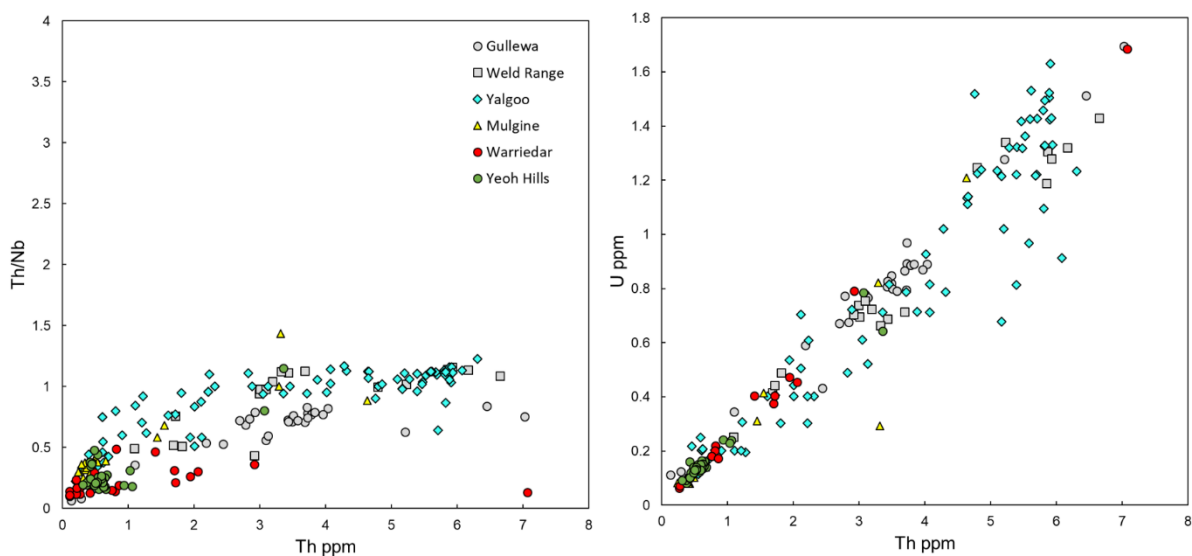


**Figure 5.8:** Incompatible element variation plots against Th, for Yalgoo, Mt. Mulgine, Warriedar, Yeoh Hills, Gullewa and Weld Range.

## Normalized Primitive Mantle Plots

Normalised primitive mantle plots were used in the analysis of the 54 samples collected. These plots were used to identify different magma systems and were then compared to the petrography results from Chapter 4.

### Mt. Mulgine

Mt. Mulgine samples are fairly similar with consistent Nb, Ti and Al depletions with a general flat trend as seen in Figure 5.9. Sample trends are usually situated around 5 on the y-axis in Figure 5.9. Sample MG1 in this group crosscuts other samples in the graph on the right-hand side in the Al-V-Sc fields. These samples belong to the Meekatharra Formation with two samples (MG26 and MG27) in the Warriedar Suite and consist of mainly basaltic or andesitic compositions (chapter 4).

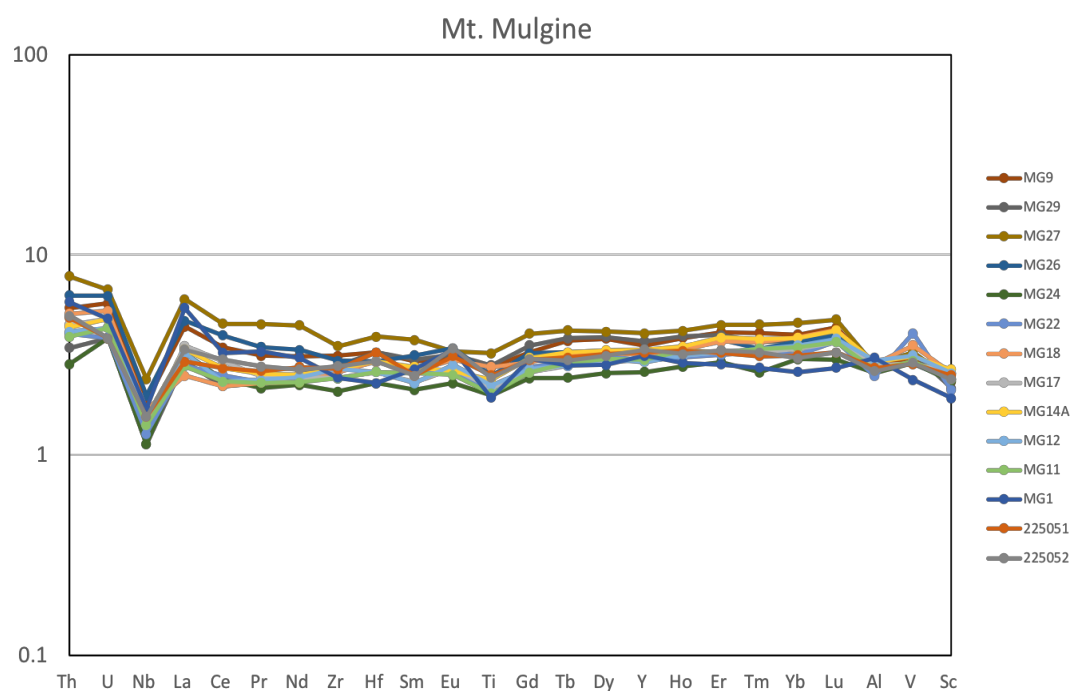


*Figure 5.9: Normalised primitive mantle plot for Mt. Mulgine samples from this study.*

## Yeoh Hills

Yeoh Hills samples show strong similarities with depletions in Nb, Al, Ti, and Sc as seen in Figure 5.10. Samples are separated with varying amounts of fractionation. Sample YH19 is more analogous to the hypothetical primitive mantle value, due to its proximity to a value of 1. Samples display a microcrystalline basaltic texture (chapter 4) and belong to the Singleton Formation in the Norie Group.

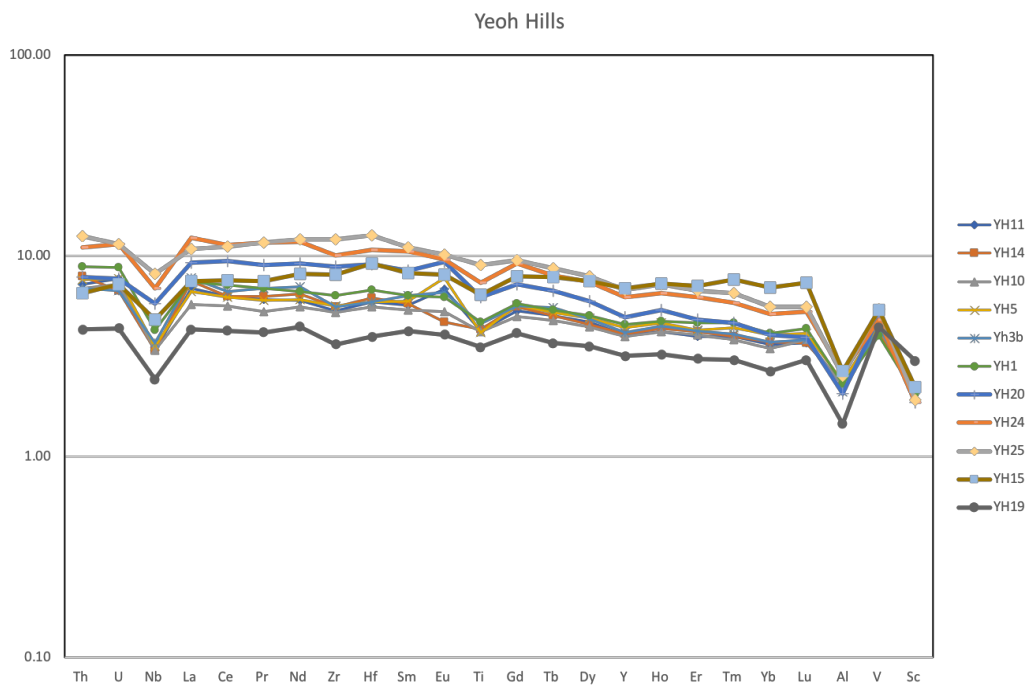
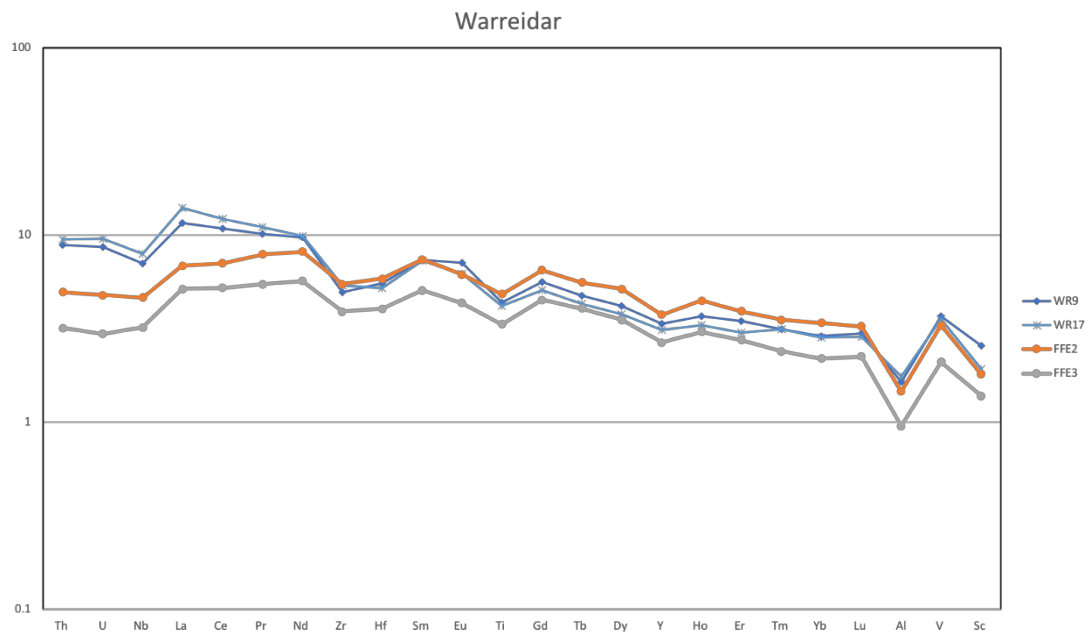


Figure 5.10: Normalised primitive mantle plot for Yeoh Hills samples from this study.

## Warriedar

A high variation in the Warriedar area is due to both Norie and Polelle Groups being present. The main trends in these samples are, common depletions in Nb, Ti and Al showing some enrichment in LREE. The first trend shown in Figure 5.11 consists of samples WR17, WR9, FFE2 and FFE3 and shows variability in LREE in comparison to similar MREE and HREE concentrations. These samples are related to the Polelle Group as well as Fields Find East samples in the Norie Group.



**Figure 5.11:** Normalised primitive mantle plot for some Warriedar samples from this study. Samples show close associations in the HREE but are variable in LREE.

Other trends within this area on Figure 5.12 include a generally flat trend consisting of samples WR16, WR15 and WR10, which are all classified as Singleton Formation within the Norie Group except for WR10 in the Warriedar Suite within the Polelle Group. WR10 shows some variation with less depleted Ti values relative to Lu and V and shows a Zr-Hf trough.

The final trend within this area (Fig. 5.12) is largely enriched in LREE compared to HREE and shows a great depletion in Al relative to the MREE. Zr-Hf troughs are present in samples WR11 and WR12, however, not in sample WR8. WR11 and WR12 belong to the Singleton Formation within the Norie Group, and WR8 belongs to the Meekatharra Formation in the Polelle Group. These rocks are considered gabbroitic and are intrusive.

Sample FFE1 on Figure 5.12 shows a Zr-Hf trough with depletions in Nb, Ti and Al with a variable trend. This sample was collected in a shear zone and is highly altered (carbonate veins) as seen in Figure 4.1. Hence, there is a low reliability for the acquisition of original magma compositions from this sample.

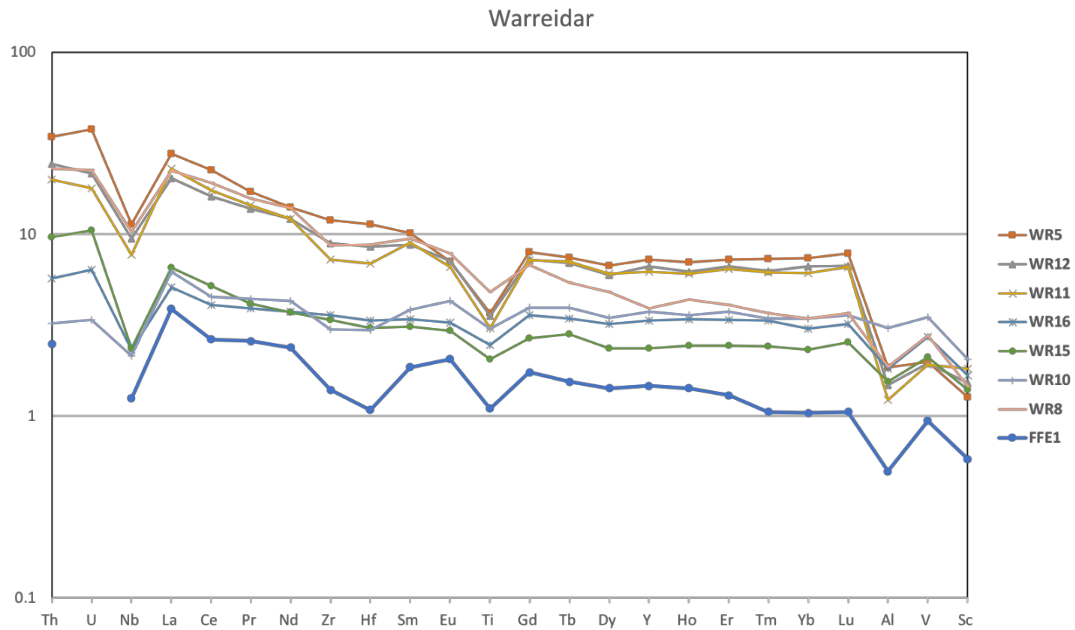


**Figure 5.12:** Normalised primitive mantle plot for some Warreidar samples from this study. Samples show 3 trends, an upper high-LREE trend, and moderate LREE trend and a lower sample, FFE1.

## Yalgoo

Yalgoo samples showed some variation in trends with some main features being depletions in Nb, Ti and Al and overall enrichment in LREE compared to HREE as seen in Figures 5.13 and 5.14.

There are two main groups defined in this area. The first group on Figure 5.13 shows great enrichments in LREE and therefore is termed the high-LREE group. The overall trend of this group is convex with some depletions in Zr. Samples are of basaltic compositions with frequent spinifex texture documented. Sample 225152 shows similar trends to this high-LREE group but has lower values on the y-axis. This sample has a cumulous texture and is altered to talc.

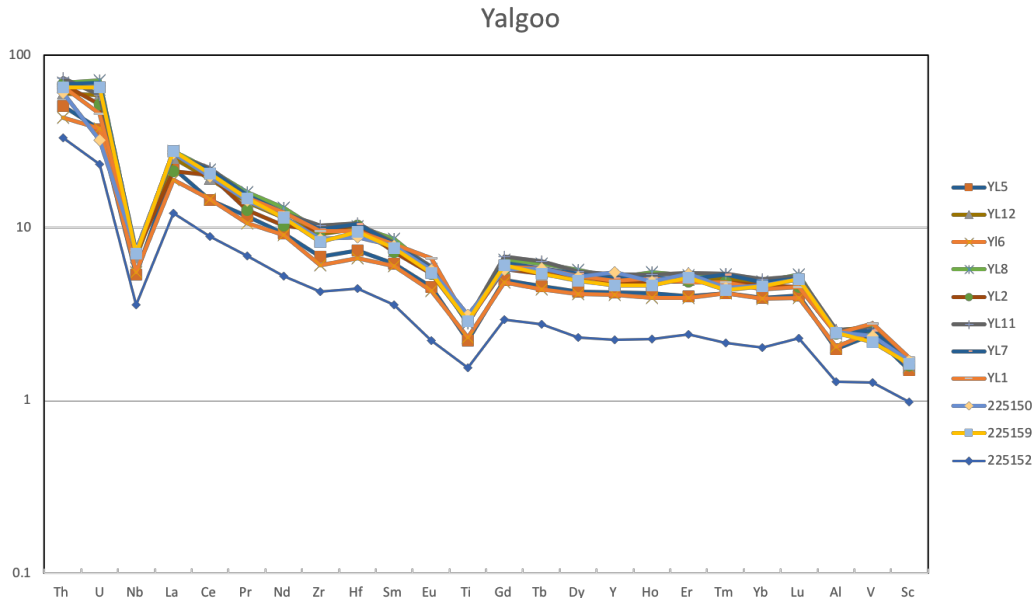


**Figure 5.13:** Normalised primitive mantle plot for high-LREE Yalgoo samples from this study.

The second group on Figure 5.14 shows a flat trend with the main features described above. According to the Yalgoo 2015 map, all samples are from the Mugs Luck Basalt Member with the exception of YL16 and YL17 in the Carlaminda Komatiite Member. As mentioned, in chapter 2, the status of these members is under review by the GSWA. In addition, all of the samples consist of basaltic compositions, many showing pyroxene spinifex textures, as described in chapter 4, but none of the samples are actually komatiites.

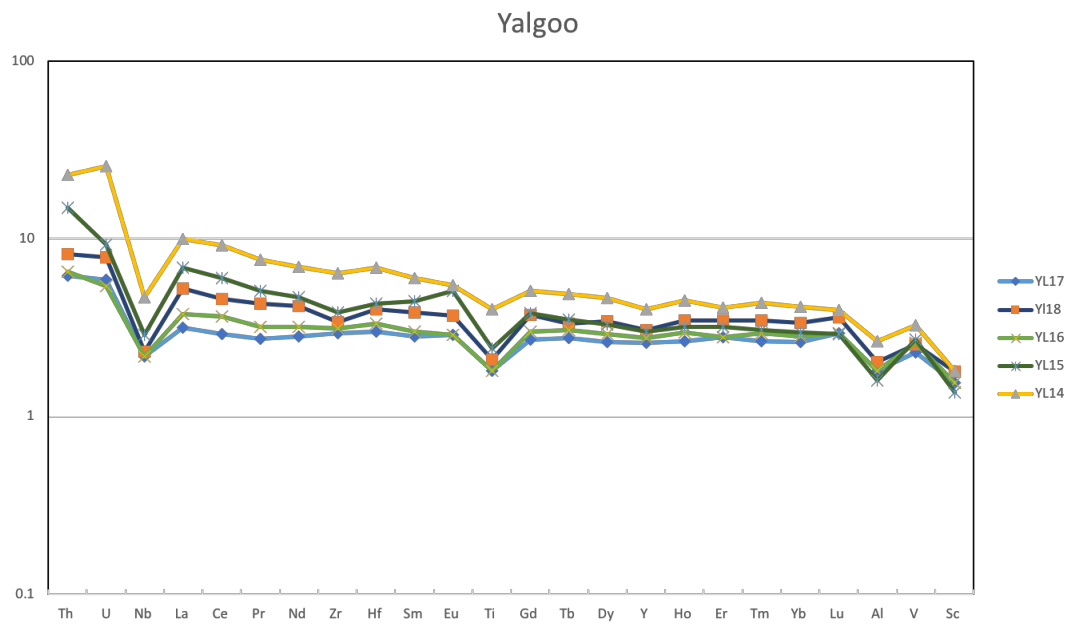


**Figure 5.14:** Normalised primitive mantle plot for low-LREE Yalgoo samples from this study.

## Chapter 6 Discussion

This study investigates similarly aged volcanic sequences to give insight onto the Meso- Neo-Archean geodynamics in the southwest Yilgarn. Through petrography and geochemical methods described in previous chapters, possible subduction-style or plume-related rocks can be identified in the study area.

Plots in chapter 5 present the overall compositional range for rock suites in each area and the classification plots put samples into broad categories. The primitive mantle-normalised geochemical plots display a variety of patterns and elemental abundances, but some features occur on most or all plots. For example, there are “depletions” of Nb relative to neighbouring Th-U and La. The light rare earths increase in concentration to the left with increasing “incompatibility” as referenced to mantle melting associated with mid-ocean ridges. In this chapter, geochemical variations are assessed in detail to:

- establish sets of samples that are likely to belong to a single magmatic system or multiple similar systems
- assess the possible role of crustal contamination in modifying the compositions of mantle-derived magmas
- evaluate possible tectonic processes associated with these magmas, particularly the possible roles of subduction style processes and (or) mantle plume events.

The use of discrimination plots to identify rock types is not always straight forward. These plots can also be obstructed by the interference of element mobility and crystal-liquid fractionation processes (Rollinson, 1993). Another factor that can interfere, is the differing tectonic environments in the Archean, where higher mantle temperatures can cause higher degrees of mantle and crustal melting and less mantle fractionation (Rollinson, 1993). This then affects the trace element composition of the mantle source

and thus cannot infer the same modern processes, such as long-lived subduction systems. In addition, samples may fall on the boundary of two or more rock types, the classification will then be intuitively chosen. An example of this in the present study is the sample YL17, which is classified as a boninite. This may not be a true boninite based on its affinity to the bounding lines of the graph, where a true boninite refers to a mantle source that was strongly depleted and then re-enriched by subduction-style processes in the mantle. Therefore, tectonic discrimination plots are not used, except for the Th/Yb versus Nb/Yb plot of Pearce (2008), which has been used frequently in previous Archean studies.

### Assessing Crustal Contamination and Magma Mixing

Samples from this study could potentially represent mantle magmas modified through crustal contamination due to the presence of older crust (TTG) in the western Yilgarn (Cassidy et al., 2006; Champion and Huston, 2016). For some sample sets, crustal contamination is not a likely scenario. In the case of many Mt. Mulgine and Yeoh Hills samples, they display low ratios of High Field Strength Elements, such as Nb/Zr, that are similar to the mantle, but not crustal granites, and their normalised primitive mantle plots do not display strong enrichment of the light rare earths, which is typical of granite or crustal contamination.

Plots involving Th are frequently used to assess crustal contamination because the element is concentrated in continental crust and sediments. The Th/Yb vs Nb/Yb plot of Pearce (2008) is commonly used to assess the contamination process because Th and Nb behave similarly in igneous processes, resulting in the arrays shown in Figure 6.1. Trends of contamination will result in sub-vertical trends but, as noted by Smithies et al. (2018) in their northern Youanmi study, there are no such indications of major contamination in the Youanmi volcanic rocks.

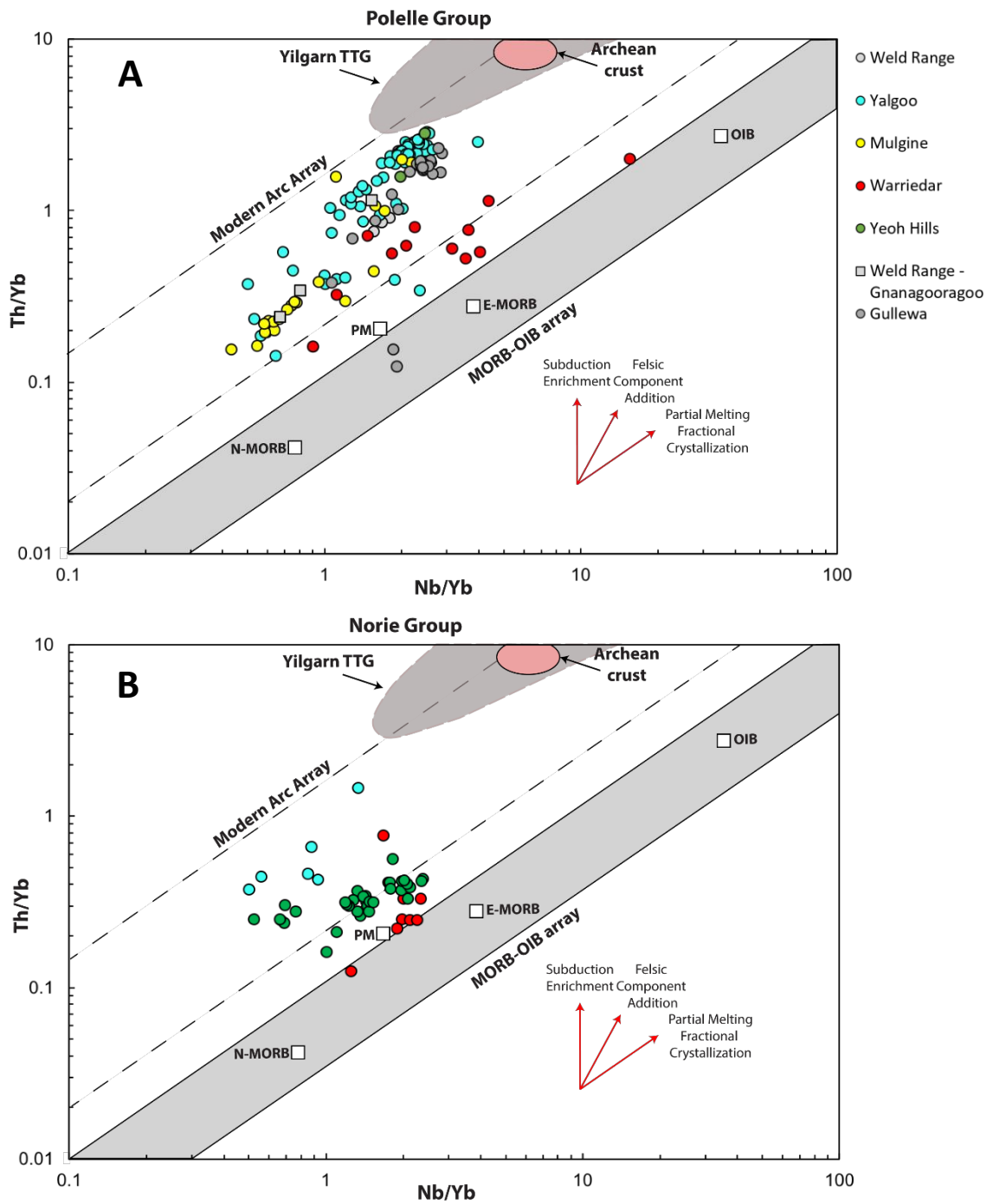


**Figure 6.1:** Th/Yb vs Nb/Yb plot after Pearce, 2008 and Smithies et al., 2018, for **A)** the Polelle Group **B)** the Norie Group. Most samples define parallel trends to the mantle array, with Polelle samples showing a strong trend in Yalgoo and Mt. Mulgine sample areas. Samples do not enter the Yilgarn TTG field. A horizontal trend is defined in A composed of Yalgoo and Yeoh Hills samples.

One difference between the present samples and the Smithies et al (2018) data is a noticeable horizontal trend for 7 Yalgoo samples (YL16, YL17, YL18, 81341, 81338, 81336 and 81322), which is an unusual feature (Fig. 6.1). Two additional Yalgoo samples, 205850 and 205820, extend the trend into a cluster of Yeoh Hills samples and occur in a unit described as, “peridotite with relict olivine  $\pm$  pyroxene cumulate textures; typically strongly metamorphosed”, on the Yalgoo map (Ivanic et al., 2015). Because neither fractionation or contamination should produce near horizontal trends, the cumulate rocks at one end of the trend suggest magma mixing between ascending magmas and ultramafic cumulates within the magma plumbing system. Petrographic evidence also supports this idea, with reference to Figure 4.12 in chapter 4, secondary hornblende crystals are common in sample YL18 and are present but less apparent in sample YL17. These crystals have a reaction rim which can indicate the reaction when one magma or its minerals interacts with the other. The primary crystal type here is interpreted to be olivine, derived from a cumulate magma, that has been collected during magma ascension.

High concentrations of incompatible elements (e.g., Zr, Hf, Th, Nb) can indicate an extensive liquid evolution, an enriched source, or crustal contamination, particularly if they display a positive anomaly versus the REE on normalized plots (Winter, 2014). However, in the case of negative Zr-Hf anomalies (depletions), as seen in these Warriedar Suite samples, it is very difficult to explain these as the result of crustal contamination in the Archean because very few granites display such features. In Cenozoic rocks with these Zr-Hf depletions, it is inferred that zircon (host to Zr and Hf) was left behind in the mantle when subducted sediments partially melted, and enriched magmas in MREE-LREE (Hermann and Rubatto, 2009). This depletion is not a feature inherited from TTG's, which represent the Archean crust generally used to model crustal contamination as seen in Barnes and Van Kranendonk (2014).

If the geochemical signatures of the study area rocks are not contaminated, then they can be compared to Cenozoic subduction-related rocks. One commonly used plot for young subduction zones is the Ba/Th vs Th plot in Figure 6.2 (after Hawkesworth et al., 1997). Vertical trends on the plot indicate fluid input because Ba is much more soluble in water than Th, and horizontal trends indicate a sediment input because there is much more Th in sediment than Ba (Hawkesworth et al., 1997). Vertical trends are somewhat indicative of incompatible element-depleted arcs and horizontal trends define trace element-enriched arcs as per examples of Hawkesworth et al. (1997). Intermediate samples are then clustered with lower amounts of Th and lower Ba/Th. These samples indicate a mixed contribution of sediments, fluids and possibly crustal components (TTG's). An example of a mixed source is the Matthew and Hunter subduction zone, which is a young (< 2 Ma) subduction zone comprising MORB and subducted oceanic crust (Patriat et al., 2019). Mt. Mulgine, Yeoh Hills and Warriedar samples show a vertical trend on this plot indicating a fluid source. However, some samples align with a sediment source. This can be attributed the potential for fluids to carry some subduction sediment (Hawkesworth et al., 1997) suggesting mixed process.

On this plot, a correlation between Ba/Th to Th might indicate contamination or a combination of hydrous fluids and sediment melts in the mantle source. In any case, such an effect is only seen in a few Weld Range, Gullewa and Warriedar samples highlighted on Figure 6.2. Samples 81353 (Yalgoo) and 83415 (Mulgine) may have also been affected by a contaminate, along with the three Warriedar samples, 211193, WR5 and WR11.

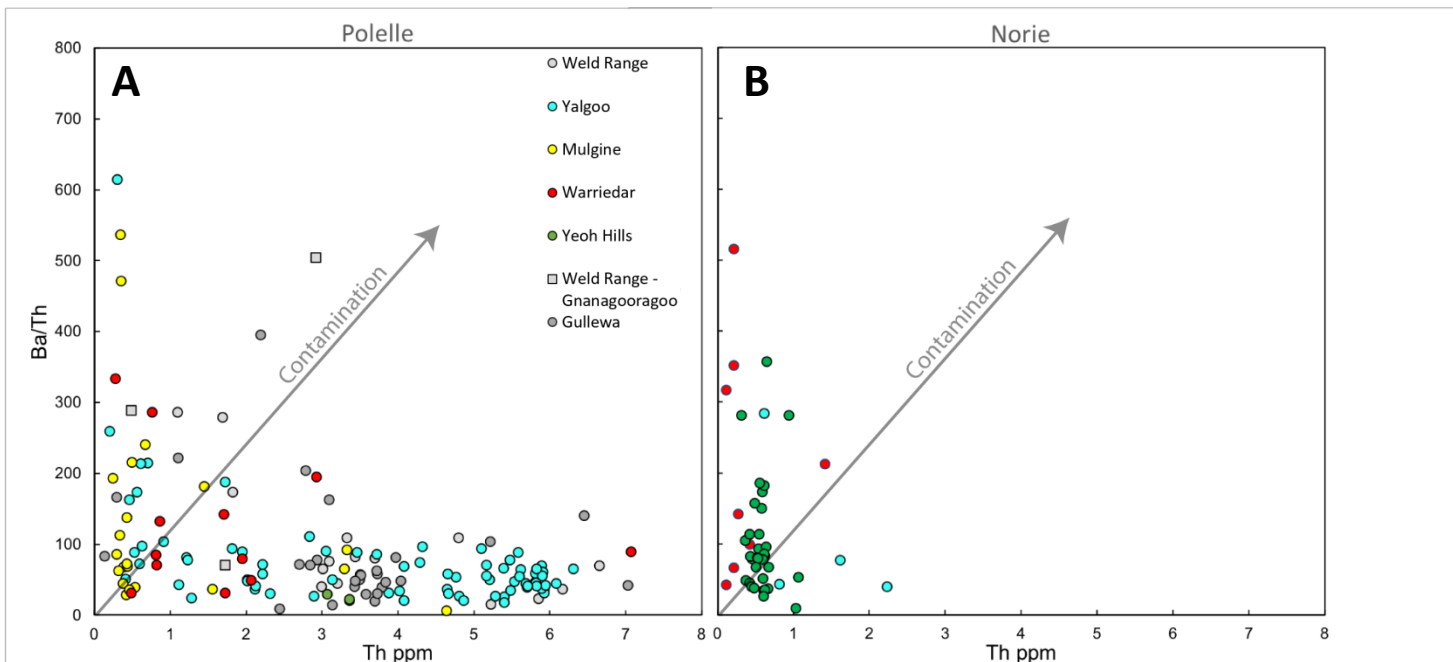


**Figure 6.2:** Ba/Th plot for **A)** the Polelle Group **B)** the Norie Group. Vertical trends indicate a fluid source, and horizontal trends denote a sediment melt source. Contamination trends are defined by the grey arrow.

As noted in chapter 5, four boninitic samples were identified, based on the new definition. These samples are similar to those of Lowrey et al. (2019 in press), which showed concave REE patterns and Th and Zr-Hf enrichments. The similarity in signatures between these boninites, and the fact that both are found in the Meekatharra Formation, suggests that the results of their extensive isotope data interrogation applies to the boninites of the present study. Lowrey et al. (2019 in press) concluded with minimal crustal contamination in the boninite samples in the Polelle group based on  $^{147}\text{Sm}/^{144}\text{Nd}$  isotope analysis. They then inferred a re-enriched mantle melt source rather than a TTG contaminant acting on a mantle magma. Wyman (2019) reached a similar conclusion given that TTG's could not reproduce the positive Zr-Hf anomalies found in some boninites (or boninitic) samples. Another Murchison Domain study incorporating isotope data was reported by Ivanic et al. (2015) who found minimal contamination in intrusions of similar age that also exhibit “subduction-style” geochemical signatures. Ivanic et al. (2015) inferred a hydrated mantle source for the hornblende-rich intrusions of the Narndee Igneous Complex (Youanmi Terrane).

Other features can give an indication of crustal contamination. Zr-Hf troughs were only observed in some Warriedar samples (WR8, WR9, WR10, WR11, WR12 and WR17), which are shallow intrusive rocks. These intrusions were emplaced at around the same time as volcanism in the Polelle group. They are compared to the Warriedar Suite (Polelle group), in the Mt. Magnet area from Wyman (2019). Figure 6.3 shows the similarities between these more northern Warriedar Suite samples (Mt. Magnet) and the southern samples in the Warriedar area from this study. This similarity implies a Murchison Domain sized process relating to enrichment in REE in mantle sources.

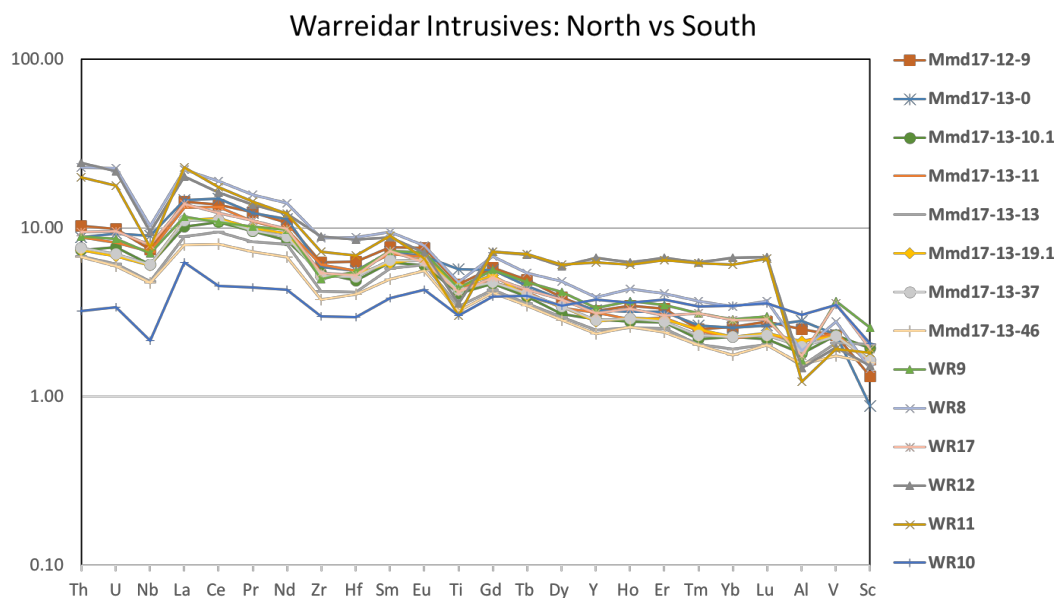


**Figure 6.3:** Normalised primitive mantle plot showing similarities of the Warriedar Intrusive Suite between the north Mt. Magnet samples (Wyman, 2019; Mmd samples) and the south Warriedar area samples from this study (WR samples)

Samples WR5, WR11 and WR12 (Fig 5.12), in the Warriedar area exhibit extreme depletion in HREE compared to LREE. This can be indicative of garnet in the source, as defined by partition coefficients (Rollinson, 1993). This strong variation in HREE and LREE can imply a deeper sourced intrusion in the Warriedar area or a magma melting process that moved upward in the mantle, possibly during crustal extension.

## Geological Map Implications

Petrographical analysis allowed for the first step in assessing the current geological maps of Ninghan (Ivanic, 2018), Yalgoo (Ivanic et al., 2015) and Perenjori (GSWA, 1983) since the misinterpretation of pyroxene spinifex basaltic rocks identified in Lowrey et al. (2017). Rock types such as “platy olivine spinifex-textured komatiite; randomly oriented plates of serpentine after olivine up to 20 mm long; includes flows of pyroxene spinifex-textured basalt; metamorphosed” (Ivanic et al., 2015) in the Yalgoo map have been refined with all petrographically studied samples only showing pyroxene-spinifex textured basaltic rock types. This is evident in samples YL16 and YL17 showing siliceous high-Mg basalt (SHMB) and boninite compositions respectively. Hence, this misinterpretation is attributed to the spinifex texture seen in YL17.

Boninite samples, MG11, MG12, MG17 and MG24, can be compared to their assigned units on the Perenjori/Ninghan geological map. The samples were identified as “Pyroxene spinifex-textured basalt and minor basalt; locally variolitic; interlayered with thin sills of granophyric to coarse-grained leucogabbro; metamorphosed” (Ivanic, 2018), as extrapolated from the Ninghan map. Pyroxene spinifex or acicular texture was only identified in one Mt. Mulgine sample (MG14A), located near MG12 and MG11. MG12 and MG11 displayed a stubby cruciform texture described in chapter 4 and observed in Phanerozoic boninites (Wyman and Kerrich, 2012). The results show that even within one group of chemically similar rocks, there is significant textural variability in one given area.

## Depositional Environment

Primary evidence for the depositional setting of magmas can be seen in rock types identified by the GSWA and the petrography from this study. Varioles are abundant

in some of the volcanic units and are also found in similar greenstone sequences around the world, such as the Abitibi belt (Fowler et al., 2002). An example of this is the presence of varioles identified in chapter 4, in the Yeoh Hills samples, YH14 and YH15. The whole rock geochemistry of the variolitic samples, YH14 and YH15, is indistinguishable from other Yeoh Hills samples. This is most evident on the Yeoh Hills normalised primitive mantle plot in Figure 5.10 where these two samples have the same REE patterns as all others in the area, suggesting one magma source. Humbert et al. (2018) attributed the formation of Paleoproterozoic variolites of the Hekpoort Formation, Kaapvaal craton to undercooling (supercooling) of submarine magmas. The cause of this undercooling was accredited to sub-aqueous deposition (Humbert et al., 2018) but the precise mechanism was not explained. Ballhaus et al. (2015) suggest that they result from H<sub>2</sub>O saturation in the melts, which would be enhanced by eruption on the ocean floor. They also note that such features are common in suprasubduction zone ophiolites such as Troodos in Cyprus. Other evidence for a submarine scenario, is the presence of pillow basalts in this studies' volcanic sequences, identified in both the Ninghan (Ivanic, 2018) and Yalgoo (Ivanic et al., 2015) maps. Hence, the varioles are likely the result of the cooling of water-rich magma in an aqueous depositional environment.

## Komatiites

The identification of any komatiites in the overall sample area is a critical aim of this study. The Pearce and Reagan (2019) discrimination plots, identified 2 possible komatiites, samples FFE3 and WR16. These were both found in the Warriedar study area, where a shallow intrusive Warriedar Suite is widespread. Sample FFE3 has been identified as a cumulate through the petrography in chapter 4. Hence, the high-MgO (36.72 wt%) content is attributed to accumulated primary olivine crystals. The other sample, WR16, did not have petrographic information. Therefore, it is inferred that this sample is not a komatiite, based on its similarity in primitive mantle trends with

WR15 which does not pass all the Pearce and Reagan (2019) plots to classify as a komatiite. Also, the sample is close to the boundary lines for picrites and boninites (LSB) and therefore can be interpreted as a picritic basalt. Therefore, no komatiites were found in the study area, even with stratigraphic sequences being labelled as komatiites.

## Boninites

Samples with low-Si boninite compositions (MG11, MG12, MG17 and MG24), identified in chapter 5 of this study using the Pearce and Reagan (2019) scheme are located in the Mt. Mulgine area in the Meekatharra Formation within the Polelle group. These are likely to correlate to the Bassets Member in the Polelle Syncline (Lowrey et al., 2019 in press). The rocks show similar features that include a slightly concave structure with Nb depletions in relation to Th and  $\text{TiO}_2$  (<0.5 wt%) depletions and slight enrichments in HREE than in LREE. Where, Ti troughs are very shallow in these samples which can show a lack of contamination, where Ti is enriched in the crust. Nb troughs are indicative of subduction enrichment in post-Archean settings (Pearce and Stern, 2006).

Other Mulgine samples that did not enter the boninite field are considered to be from similar, if not the same source, due to their close association with the boninite field in all plots. These are termed 'high Mg-andesites' and one other sample termed 'low Ti-basalt'. This can show an evolutionary path of Mt. Mulgine are samples. For these and other Murchison Domain samples to be considered subduction-related, depletion of incompatible elements such as Ti and Nb relative to Th and Zr, is required (Turner et al., 2014), which produce the negative Nb and Ti anomalies characteristic of arc lavas.

The Zr vs Th plot in Figure 6.4 gives an indication of the number of magma systems in relation to the samples from this study (Wyman, 2019). The plot shows at least three

trends, from samples in this study, defined by linear trends seen in Figure 6.4, similar to the Nb vs Th plot. The first trend is characterized by an upward trajectory and is defined by Yeoh Hills samples. The second is defined by Warriedar samples, and the third is defined by both Mt. Mulgine and Yalgoo samples. 5 Yeoh Hills samples define an upwards trend on this plot, corresponding to increasing fractionation on their respective normalised primitive mantle plots. They display a more LREE re-enriched source for Yalgoo samples than the majority of Yeoh Hills samples. Two Yeoh Hills samples are more analogous with the dominate Yalgoo trend, hence showing a more enriched source again. Additionally, 4 Mt. Mulgine samples follow the Yalgoo trend, and are similar to Yalgoo samples which have high-LREE levels.

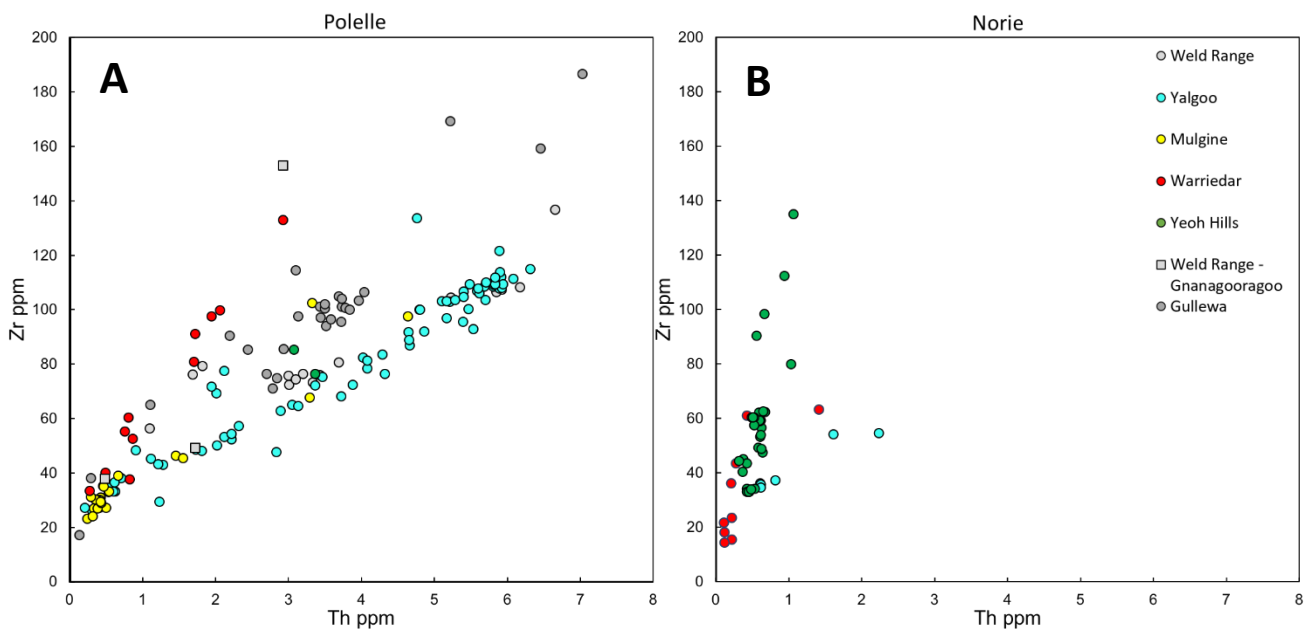


**Figure 6.4:** Zr vs Th plots for **A)** the Polelle Group **B)** the Norie Group. Trends indicate the amount of magma systems that are representative of the sample set (Wyman, 2019), where a minimum of 3 trends are identified.

## Regional Correlations of the Meekatharra Formation

There are differences in these Polelle Group boninites in the Mt Mulgine area compared to examples from the Norie Group. Lowrey et al. (2019 in press) and Wyman et al. (2019) show that the Norie boninitic rocks display more variable normalised primitive mantle trends compared to the Polelle Groups examples whose

trends are much flatter. These observations provide support for the regional mapping correlations of units assigned to the Polelle Group.

Two kinds of SHMB are identified together at Yalgoo, Gullewa and Weld Range, collectively as seen in Figure 6.5 and 6.6. One of the rock types show high-Th and -LREE and at Yalgoo is thought to be a part of the Meekatharra Formation in the Polelle group (Jack Lowrey, GSWA pers. comm., 2019). The first group of rocks (Fig. 6.5) has much steeper trends on primitive mantle normalised plots than the second group (Fig. 6.6), due to high LREE/HREE ratios and is characterised by high Th-U levels, high Th/Nb ratios, and Ti troughs, creating a concave structure. The second group of rocks has a shallower trend than the first due to normalised LREE/HREE ratios near 1 and is characterised by lower Th/Nb ratios, and Ti troughs.

The recurring association of the two rock types is based on trace elements but this correlation is also supported by similar major element concentrations in Gullewa and Weld Range which are comparable to those of the Yalgoo area, as seen in Figure 5.4 of chapter 5. There are slight regional variations in the high-LREE group from the north to the south, however, but all samples were derived from a similar enriched Th and LREE source and origin. These results demonstrate a widespread episode of Polelle Group volcanism in the north (Weld Range area), the west (Gullewa) and the south (Yalgoo area).

The close association of the two groups indicates that they erupted in the same tectonic environment. The low-LREE group may be less fractionated than the high-LREE group but some differences may come from their sources. A likely generation scenario for the high Th contents of these flows in the Polelle Group could be derived from melting of sediment (due to its high Th content) from a subduction source. The textures within these two groups both include pyroxene spinifex textured basalts and with the Yalgoo samples, this is the dominant texture. Two samples from this study

in the Yalgoo area do not have this spinifex texture and are highly altered, which is reflected by lower overall values on their primitive mantle plots.

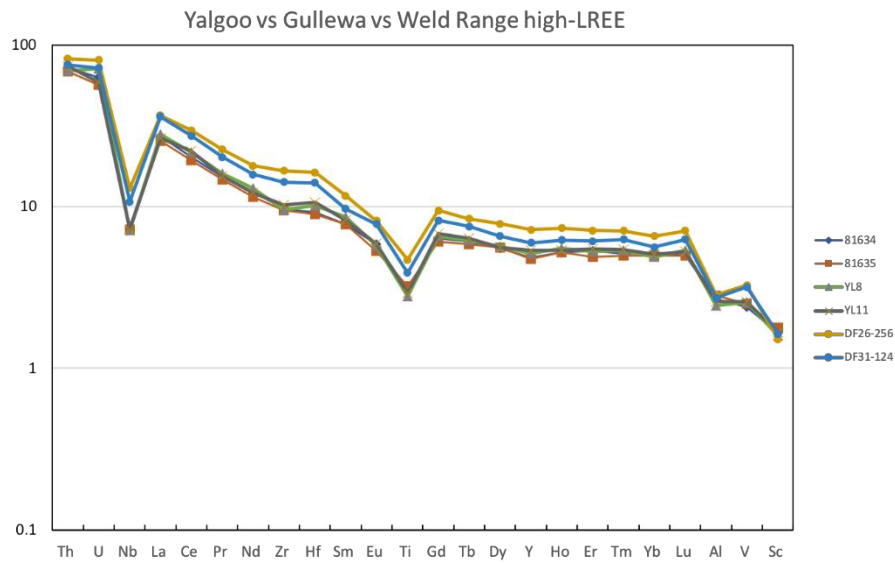


**Figure 6.6:** Normalised primitive mantle plot for high-LREE samples from Yalgoo (YL8, YL11), Gullewa (DF26-256, DF31-124) and Weld Range (81634, 81635).

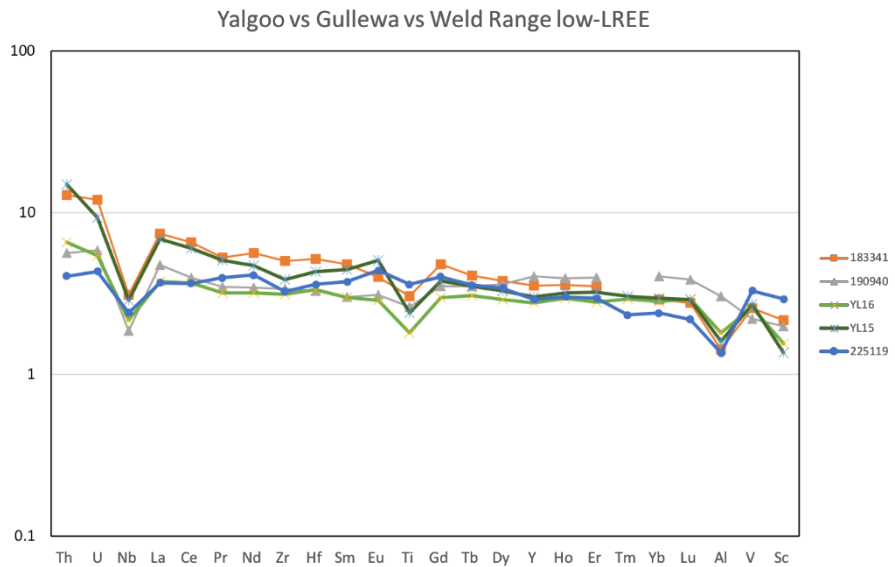


**Figure 6.5:** Normalised primitive mantle plot for low-LREE samples from Yalgoo (YL16, YL17), Gullewa (225119) and Weld Range (183341, 190940).

## Geodynamic Significance

Generation of boninites-like rocks from crustal contamination of mantle plume rocks is possible if komatiites were present in the northwest Yilgarn. However, there is

currently no evidence for this, with the “komatiites” previously identified in the field by studies such as Watkins and Hickman (1990) being reanalysed and reclassified. This issue is being resolved by studies such as Lowrey et al (2017) and this study. Re-assessment of the 2830 Ma ‘Norie plume’ by Wyman (2019) has further suggested that contaminated komatiites cannot generate boninites with the features seen in this study in the northwest Yilgarn.

The samples from this study, especially Yalgoo samples, are analogous with the modern arc array seen in Figure 6.1, highlighting their affinity with arc-settings. They are contrasted with the boninites and LOTI from the Abitibi greenstone belt in Figure 6.7. Those were generated from a depleted mantle plume source, which were then further depleted by early arc subduction processes before being hydrated by a subducting slab (Wyman and Kerrich, 2009). The two mantle depletion processes produced much stronger depletion of incompatible elements in the Abitibi examples.

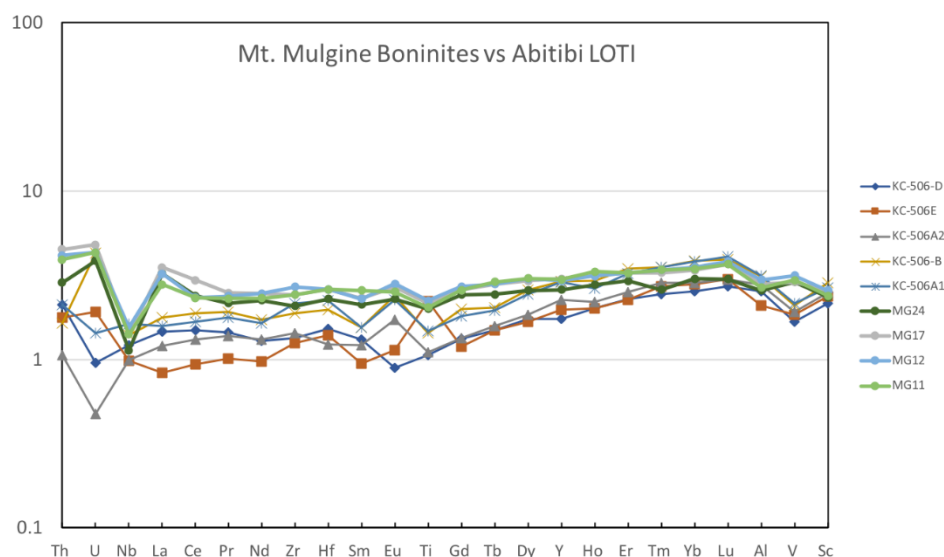


**Figure 6.7:** Normalised primitive mantle plot for Mt. Mulgine area boninites (MG samples) and Abitibi greenstone belt LOTI basalts (KC samples).

Hence, the difference between the Abitibi and Yilgarn boninites indicates that there are no missing komatiites in the Murchison Domain and there was no depletion by a mantle plume. Rather, our data implies a subduction related depletion is more likely,

such as the Matthew and Hunter subduction zone (< 2 Ma), which also shows mixed metasomatism in a subduction zone. These boninites erupted in a pre-arc stage of the subduction process (Patriat et al., 2019). They appear analogous with boninite samples in the Meekatharra Formation of the Polelle Group as seen in Figure 6.8. Hence, a subduction-like process can be inferred for this area.

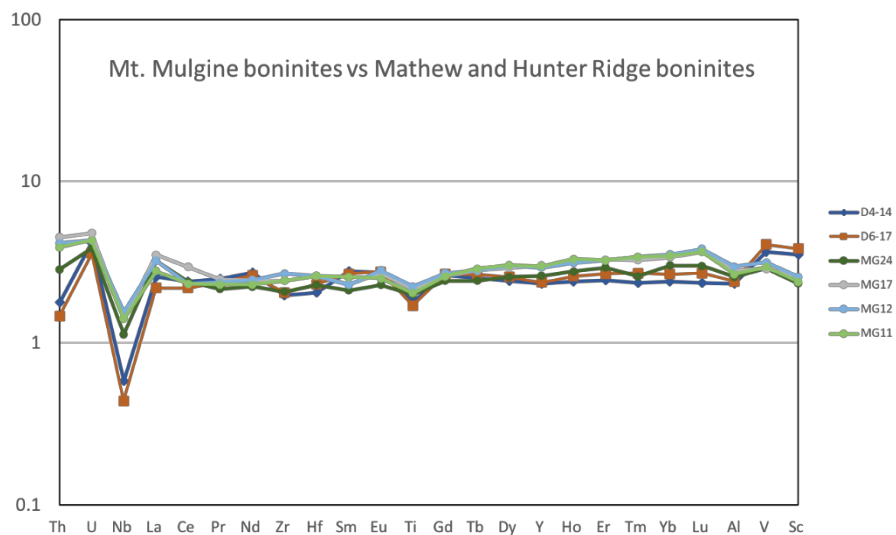


**Figure 6.8:** Mt. Mulgine area, Meekatharra Formation boninites (MG samples) compared to the Hunter Ridge high-Ca boninites (D4-14 and D6-17) from Patriat et al. (2019).

## Future Study Recommendations

Establishing minimal crustal contamination in these samples can be further confirmed through  $^{147}\text{Sm}/^{144}\text{Nd}$  isotope analysis. Furthermore, geochronology in units such as the Carlaminda Komatiite Member will enhance the idea of subduction related volcanism in the Norie and Polelle groups. Further sampling, whole rock geochemistry, and petrography on the Meekatharra Formation in the Polelle Group around the Mt. Mulgine area may provide additional evidence for subduction related rocks. Along with this the units that are associated with komatiite identification need to be re-evaluated to consider the possibility of plume induced volcanism during the emplacement of Norie and Polelle volcanics. This can also be determined through an increased sample acquisition and analysis in the south Murchison Domain. Finally,

evolving ideas on the origin and tectonic processes of the northwest Yilgarn in the Meso- Neo-Archean will alter the current geological maps in the areas studied, hence a re-visit to these areas can be beneficial in assessing the geodynamic context of the area.

## Chapter 7 Conclusions

This study addresses the controversial debate on the geodynamics in the Meso- Neo-Archean. The results clarify the distribution, origin and significance of boninite-like and associated rocks in the study area, with some major results summarised below:

- Minimal crustal contamination is established with the use of Th x-y plots and the Th/Yb vs Nb/Yb plot with no inherited TTG signatures found.
- Magma mixing is a likely possibility for the Meekatharra Formation (Polelle Group) and the Singleton Formation (Norie Group).
- No Komatiites were found in the study area. Samples FFE3 and WR16 fell into the komatiite field in the Pearce and Reagan (2019) plots, however, were considered not a true komatiite.
- Boninites were found in the Meekatharra Formation of the Polelle group and imply a subduction process in the Meso- Neo-Archean.
- Samples were compared to the Abitibi greenstone belt plume-arc LOTI rocks and the Hunter Ridge pre-arc boninites and were considered to more closely resemble the latter, i.e., implying an arc setting.
- Relating the north and south Murchison with comparisons of the Gullewa and Weld Range high-LREE samples with Yalgoo samples. This implies similar processes throughout the Norie and Polelle Groups, with some regional variation mainly seen in the REE concentrations.
- 2 types of metasomatism are identified, sedimentary melts and fluids, with mixed sources in all areas. Sedimentary melts show steep REE trends defined by LREE enrichment and fluid melts show flatter REE patterns.
- Subduction related volcanism is suggested for the Polelle Group.

- There is no evidence for a mantle plume beneath the Yilgarn Craton at ~ 2800 Ma.

## References

- ALS, 2015. Schedule of Services & Fees [WWW Document]. URL <https://www.alsglobal.com/en-au/services-and-products/geochemistry/geochemistry-testing-and-analysis/whole-rock-analysis-and-lithochemisrtry>
- Arndt, N., Leshar, C.M., Barnes, S.J., 2008. Komatiite. Cambridge University Press, New York.
- Ballhaus, C., Fonseca, R.O.C., Münker, C., Kirchenbaur, M., Zirner, A., 2015. Spheroidal textures in igneous rocks - Textural consequences of H<sub>2</sub>O saturation in basaltic melts. *Geochim. Cosmochim. Acta*. <https://doi.org/10.1016/j.gca.2015.07.029>
- Barley, M.E., Brown, S.J.A., Krapež, B., Kositcin, N., 2008. Physical volcanology and geochemistry of a Late Archaean volcanic arc: Kurnalpi and Gindalbie Terranes, Eastern Goldfields Superterrane, Western Australia. *Precambrian Res.* <https://doi.org/10.1016/j.precamres.2007.06.019>
- Barley, M.E., Kerrich, R., Reudavy, I., Xie, Q., 2000. Late Archaean Ti-rich, Al-depleted komatiites and komatiitic volcanoclastic rocks from the Murchison Terrane in Western Australia. *Aust. J. Earth Sci.* <https://doi.org/10.1046/j.1440-0952.2000.00820.x>
- Barnes, S.J., Fiorentini, M.L., 2012. Komatiite magmas and sulfide nickel deposits: A comparison of variably endowed archaean terranes. *Econ. Geol.* <https://doi.org/10.2113/econgeo.107.5.755>
- Barnes, S.J., Van Kranendonk, M.J., 2014. Archaean andesites in the east Yilgarn craton, Australia: Products of plume-crust interaction? *Lithosphere*. <https://doi.org/10.1130/L356.1>
- Barnes, S.J., van Kranendonk, M.J., Sonntag, I., 2012. Geochemistry and tectonic setting of basalts from the Eastern Goldfields Superterrane. *Aust. J. Earth Sci.* <https://doi.org/10.1080/08120099.2012.687398>
- Baziotis, I., Economou-Eliopoulos, M., Asimow, P.D., 2017. Ultramafic lavas and high-Mg basaltic dykes from the Othris ophiolite complex, Greece. *Lithos*. <https://doi.org/10.1016/j.lithos.2017.07.015>
- Bouquain, S., Arndt, N.T., Hellebrand, E., Faure, F., 2009. Crystallochemistry and origin of pyroxenes in komatiites. *Contrib. to Mineral. Petrol.* <https://doi.org/10.1007/s00410-009-0399-0>
- Brown, A.V., Jenner, G.A., 1989. Geological setting, petrology and chemistry of Cambrian boninite and low-Ti tholeiitic lavas in western Tasmania, in: A.J., C. (Ed.), *Boninites and Related Rocks*. Unwin Hyman, London, pp. 233–263.
- Campbell, I.H., Hill, R.I., 1988. A two-stage model for the formation of the granite-greenstone terrains of the Kalgoorlie-Norseman area, Western Australia. *Earth Planet. Sci. Lett.* [https://doi.org/10.1016/0012-821X\(88\)90107-0](https://doi.org/10.1016/0012-821X(88)90107-0)

- Cassidy, K.F., Champion, D.C., Krapez, B., Barley, M., Brown, S.J.A., Blewett, R., Groenewald, B., Tyler, I., 2006. A revised geological framework for the Yilgarn Craton: Western Australia Geological Survey, Record 2006/8.
- Champion, D.C., Cassidy, K.F., 2007. An overview of the Yilgarn craton and its crustal evolution, in Bierlein, F.P., and Knox-Robinson, C.M., eds., Proceedings of Geoconferences (WA) Inc., Kalgoorlie '07 Conference.
- Champion, D.C., Huston, D.L., 2016. Radiogenic isotopes, ore deposits and metallogenic terranes: Novel approaches based on regional isotopic maps and the mineral systems concept. *Ore Geol. Rev.*  
<https://doi.org/10.1016/j.oregeorev.2015.09.025>
- Chandan-Kumar, B., Ugarkar, A.G., 2017. Geochemistry of mafic-ultramafic magmatism in the Western Ghats belt (Kudremukh greenstone belt), western Dharwar Craton, India: implications for mantle sources and geodynamic setting. *Int. Geol. Rev.* <https://doi.org/10.1080/00206814.2017.1278623>
- Chen, S.F., Riganti, A., Wyche, S., Greenfield, J.E., Nelson, D.R., 2003. Lithostratigraphy and tectonic evolution of contrasting greenstone successions in the central Yilgarn Craton, Western Australia, in: *Precambrian Research*.  
[https://doi.org/10.1016/S0301-9268\(03\)00190-6](https://doi.org/10.1016/S0301-9268(03)00190-6)
- Condie, K.C., 2008. Mantle Plumes: A Multidisciplinary Approach. *Eos, Trans. Am. Geophys. Union* 89, 112. <https://doi.org/10.1029/2008EO110011>
- Cooper, A.F., Reid, D.L., 1991. Textural evidence for calcite carbonatite magmas, Dicker Willem, southwest Namibia. *Geology*. [https://doi.org/10.1130/0091-7613\(1991\)019<1193:TEFCCM>2.3.CO;2](https://doi.org/10.1130/0091-7613(1991)019<1193:TEFCCM>2.3.CO;2)
- Czarnota, K., Champion, D.C., Goscombe, B., Blewett, R.S., Cassidy, K.F., Henson, P.A., Groenewald, P.B., 2010. Geodynamics of the eastern Yilgarn Craton. *Precambrian Res.* 183, 175–202. <https://doi.org/10.1016/j.precamres.2010.08.004>
- Dhuime, B., Hawkesworth, C.J., Cawood, P.A., Storey, C.D., 2012. A change in the geodynamics of continental growth 3 billion years ago. *Science* (80-. ).  
<https://doi.org/10.1126/science.1216066>
- Duuring, P., Hassan, L., Zelic, M., Gessner, K., 2016. Geochemical and spectral footprint of metamorphosed and deformed VMS-style mineralization in the Quinns district, Yilgarn craton, Western Australia. *Econ. Geol.*  
<https://doi.org/10.2113/econgeo.111.6.1411>
- Foley, S.F., Buhre, S., Jacob, D.E., 2003. Evolution of the Archaean crust by delamination and shallow subduction. *Nature*.  
<https://doi.org/10.1038/nature01319>
- Fowler, A.D., Berger, B., Shore, M., Jones, M.I., Ropchan, J., 2002. Supercooled rocks: Development and significance of varioles, spherulites, dendrites and spinifex in Archaean volcanic rocks, Abitibi Greenstone belt, Canada. *Precambrian Res.*  
[https://doi.org/10.1016/S0301-9268\(02\)00014-1](https://doi.org/10.1016/S0301-9268(02)00014-1)
- Gee, D., Baxter, J.L., Wilde, S.A., Williams, I.R., 1981. Crustal development in the Archaean Yilgarn block, western Australia.
- Government of Western Australia, 2019. GeoVIEW.WA [WWW Document]. URL

- <https://www.dmp.wa.gov.au/GeoView-WA-Interactive-1467.aspx>  
GSWA, 1983. Perenjori. WA Sheet SH50-06 Geol. Surv. West. Aust.
- Hawkesworth, C.J., Turner, S.P., McDermott, F., Peate, D.W., Van Calsteren, P., 1997. U-Th isotopes in arc magmas: Implications for element transfer from the subducted crust. *Science* (80-. ). <https://doi.org/10.1126/science.276.5312.551>
- Hayman, P.C., Thébaud, N., Pawley, M.J., Barnes, S.J., Cas, R.A.F., Amelin, Y., Sapkota, J., Squire, R.J., Campbell, I.H., Pegg, I., 2015. Evolution of a ~2.7Ga large igneous province: A volcanological, geochemical and geochronological study of the Agnew Greenstone Belt, and new regional correlations for the Kalgoorlie Terrane (Yilgarn Craton, Western Australia). *Precambrian Res.* <https://doi.org/10.1016/j.precamres.2015.09.016>
- Hermann, J., Rubatto, D., 2009. Accessory phase control on the trace element signature of sediment melts in subduction zones. *Chem. Geol.* <https://doi.org/10.1016/j.chemgeo.2009.05.018>
- Hill, R.I., Chappell, B.W., Campbell, I.H., 1992. Late Archaean granites of the southeastern Yilgarn Block, Western Australia: Age, geochemistry, and origin, in: *Special Paper of the Geological Society of America.* <https://doi.org/10.1130/SPE272-p211>
- Hollings, P., Wyman, D., Kerrich, R., 1999. Komatiite-basalt-rhyolite volcanic associations in Northern Superior Province greenstone belts: Significance of plume-arc interaction in the generation of the proto continental Superior Province. *Lithos.* [https://doi.org/10.1016/s0024-4937\(98\)00058-9](https://doi.org/10.1016/s0024-4937(98)00058-9)
- Hollis, S.P., Mole, D.R., Gillespie, P., Barnes, S.J., Tessalina, S., Cas, R.A.F., Hildrew, C., Pumphrey, A., Goodz, M.D., Caruso, S., Yeats, C.J., Verbeeten, A., Belford, S.M., Wyche, S., Martin, L.A.J., 2017. 2.7 Ga plume associated VHMS mineralization in the Eastern Goldfields Superterrane, Yilgarn Craton: Insights from the low temperature and shallow water, Ag-Zn-(Au) Nimbus deposit. *Precambrian Res.* <https://doi.org/10.1016/j.precamres.2017.01.002>
- Humbert, F., Elburg, M.A., Ossa, F.O., de Kock, M.O., Robion, P., 2018. Variolites of the Paleoproterozoic Hekpoort Formation (Transvaal sub-basin, Kaapvaal craton): Multistage undercooling textures?(Report). *LITHOS* 316–317, 48. <https://doi.org/10.1016/j.lithos.2018.07.005>
- Ivanic, T., 2019. Mafic–ultramafic intrusions of the Youanmi Terrane, Yilgarn Craton. *Geol. Surv. West. Aust. Report* 192, 121p.
- Ivanic, T., 2018. Ninghan. WA Sheet 2339 Geol. Surv. West. Aust.
- Ivanic, T., Li, J., Meng, Y., Guo, L., Yu, J., Chen, S., Wyche, S., I, Z., 2015. Yalgoo. WA Sheet 2241 Geol. Surv. West. Aust.
- Ivanic, T.J., Van Kranendonk, M.J., Kirkland, C.L., Wyche, S., Wingate, M.T.D., Belousova, E.A., 2012. Zircon Lu–Hf isotopes and granite geochemistry of the Murchison Domain of the Yilgarn Craton: Evidence for reworking of Eoarchean crust during Meso-Neoarchean plume-driven magmatism. *LITHOS* 148, 112–127. <https://doi.org/10.1016/j.lithos.2012.06.006>
- Ivanic, T.J., Wingate, M.T.D., Kirkland, C.L., Van Kranendonk, M.J., Wyche, S., 2010.

- Age and significance of voluminous mafic–ultramafic magmatic events in the Murchison Domain, Yilgarn Craton. *Aust. J. Earth Sci.* 57, 597–614.  
<https://doi.org/10.1080/08120099.2010.494765>
- Kisters, A.F.M., van Hinsberg, V.J., Szilas, K., 2012. Geology of an Archaean accretionary complex – The structural record of burial and return flow in the Tartoq Group of South West Greenland. *Precambrian Res.* 220–221, 107–122.  
<https://doi.org/10.1016/j.precamres.2012.07.008>
- Le Bas, M.J., 2000. IUGS Reclassification of the High-Mg and Picritic Volcanic Rocks. *J. Petrol.* 41.10.1467.
- Leshner, C.M., Arndt, N.T., 1995. REE and Nd isotope geochemistry, petrogenesis and volcanic evolution of contaminated komatiites at Kambalda, Western Australia. *LITHOS*. [https://doi.org/10.1016/0024-4937\(95\)90017-9](https://doi.org/10.1016/0024-4937(95)90017-9)
- Lowrey, J., Ivanic, T., 2018. Platy pyroxene spinifex: re-evaluating the distribution of komatiite across Western Australia’s Archean cratons 19, 39–42.
- Lowrey, J., Wyman, D.A., Ivanic, T.J., Smithies, R.H., Maas, R., 2019. Archean boninite-like rocks of the NorthWest Youanmi Terrane, Yilgarn Craton: geochemistry and genesis.
- Lowrey, J.R., Ivanic, T.J., Wyman, D.A., Roberts, M.P., 2017. Platy pyroxene: New insights into spinifex texture. *J. Petrol.* <https://doi.org/10.1093/petrology/egx069>
- Martin, H., Smithies, R.H., Rapp, R., Moyen, J.F., Champion, D., 2005. An overview of adakite, tonalite-trondhjemite-granodiorite (TTG), and sanukitoid: Relationships and some implications for crustal evolution. *Lithos*.  
<https://doi.org/10.1016/j.lithos.2004.04.048>
- Mole, D.R., Fiorentini, M.L., Cassidy, K.F., Kirkland, C.L., Thebaud, N., Mccuaig, T.C., Doublier, M.P., Durning, P., Romano, S.S., Maas, R., Belousova, E.A., Barnes, S.J., Miller, J., 2014. Crustal evolution, intra-cratonic architecture and the metallogeny of an Archaean craton. *Geol. Soc. Spec. Publ.*  
<https://doi.org/10.1144/SP393.8>
- Mole, D.R., Kirkland, C.L., Fiorentini, M.L., Barnes, S.J., Cassidy, K.F., Isaac, C., Belousova, E.A., Hartnady, M., Thebaud, N., 2019. Time-space evolution of an Archaean craton: A Hf-isotope window into continent formation. *Earth-Science Rev.* <https://doi.org/10.1016/j.earscirev.2019.04.003>
- Moroni, M., Caruso, S., Barnes, S.J., Fiorentini, M.L., 2017. Primary stratigraphic controls on ore mineral assemblages in the Wannaway komatiite-hosted nickel-sulfide deposit, Kambalda camp, Western Australia. *Ore Geol. Rev.*  
<https://doi.org/10.1016/j.oregeorev.2017.05.031>
- Mottana, A., Crespi, R., Liborio, G., Prinz, M., Harlow, G.E., 1978. *Simon and Schuster’s Guide to Rocks and Minerals*, A Fireside book. Simon and Schuster.
- Moyen, J.F., van Hunen, J., 2012. Short-term episodicity of Archaean plate tectonics. *Geology*. <https://doi.org/10.1130/G322894.1>
- Myers, J.S., 1995. The generation and assembly of an Archaean supercontinent: evidence from the Yilgarn craton, Western Australia. *Early Precambrian*

- Process. <https://doi.org/10.1144/GSL.SP.1995.095.01.09>
- Myers, J.S., 1993. Precambrian History of the West Australian Craton and Adjacent Orogens. *Annu. Rev. Earth Planet. Sci.* 21, 453–485.  
<https://doi.org/10.1146/annurev.ea.21.050193.002321>
- Myers, J.S., 1990. Precambrian tectonic evolution of part of Gondwana, southwestern Australia. [https://doi.org/10.1130/0091-7613\(1990\)018<0537:PTEOPO>2.3.CO;2](https://doi.org/10.1130/0091-7613(1990)018<0537:PTEOPO>2.3.CO;2)
- Ohnenstetter, D., Brown, W.L., 1992. Overgrowth textures, disequilibrium zoning, and cooling history of a glassy four-pyroxene boninite dyke from New Caledonia. *J. Petrol.* <https://doi.org/10.1093/petrology/33.1.231>
- Patriat, M., Falloon, T., Danyushevsky, L., Collot, J., Jean, M.M., Hoernle, K., Hauff, F., Maas, R., Woodhead, J.D., Feig, S.T., 2019. Subduction initiation terranes exposed at the front of a 2 Ma volcanically-active subduction zone. *Earth Planet. Sci. Lett.* <https://doi.org/10.1016/j.epsl.2018.12.011>
- Pawley, M., Romano, S., Hall, C., Wingate, M.T.D., 2009. The Yamarna Shear Zone: a new terrane boundary in the northeastern Yilgarn Craton? pp. 27–32.
- Pawley, M., T. D. Wingate, M., Kirkland, C.L., Wyche, S., Hall, C., Romano, S., Doublier, M., 2012. Adding pieces to the puzzle: Episodic crustal growth and a new terrane in the northeast Yilgarn Craton, Western Australia.  
<https://doi.org/10.1080/08120099.2012.696555>
- Pearce, J.A., 2008. Geochemical fingerprinting of oceanic basalts with applications to ophiolite classification and the search for Archean oceanic crust. *Lithos.* <https://doi.org/10.1016/j.lithos.2007.06.016>
- Pearce, J.A., Reagan, M.K., 2019. Identification, classification, and interpretation of boninites from Anthropocene to Eoarchean using Si-Mg-Ti systematics. *Geosphere.* <https://doi.org/10.1130/ges01661.1>
- Pearce, J.A., Robinson, P.T., 2010. The Troodos ophiolitic complex probably formed in a subduction initiation, slab edge setting. *Gondwana Res.* <https://doi.org/10.1016/j.gr.2009.12.003>
- Pearce, J.A., Stern, R.J., 2006. Origin of back-arc basin magmas: Trace element and isotope perspectives, in: *Geophysical Monograph Series.*  
<https://doi.org/10.1029/166GM06>
- Pearson, G., Wittig, N., 2008. Formation of Archaean continental lithosphere and its diamonds: The root of the problem. *J. Geol. Soc. - J GEOL SOC* 165, 895–914.  
<https://doi.org/10.1144/0016-76492008-003>
- Pidgeon, R., Hallberg, A.J., 2000. Age relationships in supracrustal sequences of the northern part of the Murchison Terrane, Archaean Yilgarn Craton, Western Australia: A combined field and zircon U-Pb study.  
<https://doi.org/10.1046/j.1440-0952.2000.00772.x>
- Piercey, S.J., Murphy, D.C., Mortensen, J.K., Paradis, S., 2001. Boninitic magmatism in a continental margin setting, Yukon-Tanana terrane, southeastern Yukon, Canada. *Geology.* [https://doi.org/10.1130/0091-7613\(2001\)029<0731:BMIACM>2.0.CO;2](https://doi.org/10.1130/0091-7613(2001)029<0731:BMIACM>2.0.CO;2)
- R.G. Cawthorn, G.M. Biggar, C.M. Graham, A. Graham, C.E. Ford, M.R. Sharpe,

- G.D., 1979. Experimental petrological data on the parental magmas to the Bushveld Complex.
- Redman, B.A., Keays, R.R., 1985. Archaean basic volcanism in the Eastern Goldfields Province, Yilgarn Block, Western Australia. *Precambrian Res.*  
[https://doi.org/10.1016/0301-9268\(85\)90048-8](https://doi.org/10.1016/0301-9268(85)90048-8)
- Rollinson, H.R., 1993. Using geochemical data: Evaluation, presentation, interpretation. Longman Scientific and Technical, New York.
- Smithies, R.H., 2000. The Archaean tonalite-trondhjemite-granodiorite (TTG) series is not an analogue of Cenozoic adakite. *Earth Planet. Sci. Lett.* 182, 115–125.  
[https://doi.org/10.1016/S0012-821X\(00\)00236-3](https://doi.org/10.1016/S0012-821X(00)00236-3)
- Smithies, R.H., Champion, D.C., 2000. The Archaean High-Mg Diorite Suite: Links to Tonalite-Trondhjemite-Granodiorite Magmatism and Implications for Early Archaean Crustal Growth. *J. Petrol.* <https://doi.org/10.1093/petrology/41.12.1653>
- Smithies, R.H., Champion, D.C., Cassidy, K.F., 2003. Formation of Earth's early Archaean continental crust, in: *Precambrian Research*.  
[https://doi.org/10.1016/S0301-9268\(03\)00182-7](https://doi.org/10.1016/S0301-9268(03)00182-7)
- Smithies, R.H., Howard, H.M., Evins, P.M., Kirkland, C.L., Kelsey, D.E., Hand, M., Wingate, M.T.D., Collins, A.S., Belousova, E., 2011. High-temperature granite magmatism, crust-mantle interaction and the mesoproterozoic intracontinental evolution of the Musgrave Province, Central Australia. *J. Petrol.*  
<https://doi.org/10.1093/petrology/egr010>
- Smithies, R.H., Ivanic, T.J., Lowrey, J.R., Morris, P.A., Barnes, S.J., Wyche, S., Lu, Y.-J., 2018. Two distinct origins for Archean greenstone belts. *Earth Planet. Sci. Lett.* 487, 106–116. <https://doi.org/10.1016/j.epsl.2018.01.034>
- Sossi, P.A., Eggins, S.M., Nesbitt, R.W., Nebel, O., Hergt, J.M., Campbell, I.H., O'Neill, H.S.C., Van Kranendonk, M., Davies, D.R., 2016. Petrogenesis and Geochemistry of Archean Komatiites. *J. Petrol.* 57, 147–184.  
<https://doi.org/10.1093/petrology/egw004>
- Sun, S.-S., Nesbitt, R.W., Mcculloch, M.T., 1988. Geochemistry and petrogenesis of archaean and early proterozoic siliceous high-Mg basalts. *Chem. Geol.*  
[https://doi.org/10.1016/0009-2541\(88\)90632-8](https://doi.org/10.1016/0009-2541(88)90632-8)
- Sun, S.S., McDonough, W.F., 1989. Chemical and isotopic systematics of oceanic basalts: Implications for mantle composition and processes. *Geol. Soc. Spec. Publ.* <https://doi.org/10.1144/GSL.SP.1989.042.01.19>
- Swager, C., 1997. Tectono-stratigraphy of late Archaean greenstone terranes in the southern Eastern Goldfields, Western Australia. [https://doi.org/10.1016/S0301-9268\(97\)00003-X](https://doi.org/10.1016/S0301-9268(97)00003-X)
- Tatsumi, Y., Shukuno, H., Sato, K., Shibata, T., Yoshikawa, M., 2003. The Petrology and Geochemistry of High-Magnesium Andesites at the Western Tip of the Setouchi Volcanic Belt, SW Japan. *J. Petrol.*  
<https://doi.org/10.1093/petrology/egg049>
- Turner, S., Rushmer, T., Reagan, M., Moyan, J.F., 2014. Heading down early on? Start of subduction on earth. *Geology.* <https://doi.org/10.1130/G34886.1>

- van Hunen, J., Zhong, S., Shapiro, N.M., Ritzwoller, M.H., 2005. New evidence for dislocation creep from 3-D geodynamic modeling of the Pacific upper mantle structure. *Earth Planet. Sci. Lett.* <https://doi.org/10.1016/j.epsl.2005.07.006>
- Van Kranendonk, M.J., Ivanic, T.J., 2009. A new lithostratigraphic scheme for the northeastern Murchison Domain, Yilgarn Craton. *Geol. Surv. West. Aust. Perth* 35–53.
- Van Kranendonk, M.J., Ivanic, T.J., Wingate, M.T.D., Kirkland, C.L., Wyche, S., 2013. Long-lived, autochthonous development of the Archean Murchison Domain, and implications for Yilgarn Craton tectonics. *Precambrian Res.* 229. <https://doi.org/10.1016/j.precamres.2012.08.009>
- Watkins, K.P., Hickman, A.H., 1990. *Geological Evolution and Mineralization of the Murchison Province, Western Australia.* Department of Mines, Western Australia.
- Wilde, S.A., Middleton, M.F., Evans, B.J., 1996. Terrane accretion in the southwestern Yilgarn Craton: Evidence from a deep seismic crustal profile. *Precambrian Res.* [https://doi.org/10.1016/0301-9268\(95\)00077-1](https://doi.org/10.1016/0301-9268(95)00077-1)
- Winter, J.D., 2014. *Principles of igneous and metamorphic petrology*, Second. ed. Pearson Education Limited, Harlow.
- Wood, C.P., 1980. Boninite at a continental margin. *Nature.* <https://doi.org/10.1038/288692a0>
- Wyche, S., Nelson, D.R., Riganti, A., 2004. 4350–3130 Ma detrital zircons in the Southern Cross Granite-Greenstone Terrane, Western Australia: Implications for the early evolution of the Yilgarn Craton. *Aust. J. Earth Sci.* <https://doi.org/10.1046/j.1400-0952.2003.01042.x>
- Wyman, D., Kerrich, R., 2009. Plume and arc magmatism in the Abitibi subprovince: Implications for the origin of Archean continental lithospheric mantle. *Precambrian Res.* <https://doi.org/10.1016/j.precamres.2008.07.008>
- Wyman, D.A., 2019. 2.8 Ga Subduction-related magmatism in the Youanmi Terrane and a revised geodynamic model for the Yilgarn Craton. *Precambrian Res.* 327, 14–33. <https://doi.org/10.1016/j.precamres.2019.02.008>
- Wyman, D.A., Kerrich, R., 2012. Geochemical and isotopic characteristics of Youanmi terrane volcanism: the role of mantle plumes and subduction tectonics in the western Yilgarn Craton. *Aust. J. Earth Sci.* 59, 671–694. <https://doi.org/10.1080/08120099.2012.702684>

Appendix 1:  
Whole Rock  
Geochemistry Data

## Whole Rock Data: Major Elements

LOCATION	SAMPLE #	GROUP	SiO2	TiO2	Al2O3	Fe2O3	MnO	MgO	CaO	K2O	Na2O	P2O5	LOI	Mg#
Yalgoo	<b>225150</b>	Polelle	55.89	0.68	12.87	9.41	0.15	9.19	8.92	0.68	2.14	0.07	1.07	68.23
Yalgoo	<b>225159</b>	Polelle	56.36	0.62	12.74	9.71	0.15	9.43	8.00	0.96	1.95	0.07	1.00	68.13
Yalgoo	<b>225152</b>	Polelle	51.30	0.34	6.58	9.64	0.16	27.71	4.16	0.01	0.05	0.04	5.82	86.35
Yalgoo	<b>225145</b>	Polelle	52.05	1.01	12.32	12.27	0.20	8.45	12.37	0.13	1.12	0.08	0.55	60.25
Yalgoo	<b>YL1</b>	Polelle	57.10	0.62	12.50	8.24	0.13	9.86	6.52	0.79	4.16	0.08	1.81	72.47
Yalgoo	<b>YL11</b>	Polelle	57.41	0.64	13.25	8.27	0.14	8.24	8.50	0.85	2.62	0.08	2.68	68.68
Yalgoo	<b>YL12</b>	Polelle	55.79	0.64	13.03	9.64	0.15	9.45	8.70	0.72	1.81	0.07	2.08	68.35
Yalgoo	<b>YL14</b>	Polelle	56.76	0.87	13.60	8.91	0.13	7.16	7.51	0.24	4.72	0.10	1.18	63.88
Yalgoo	<b>YL15</b>	Polelle	53.43	0.52	8.20	11.28	0.18	16.66	7.85	0.06	1.76	0.04	2.72	76.48
Yalgoo	<b>YL16</b>	Polelle	51.41	0.39	9.28	10.83	0.20	17.72	8.76	0.10	1.24	0.06	3.22	78.27
Yalgoo	<b>YL17</b>	Polelle	51.03	0.39	9.26	10.99	0.20	16.53	10.25	0.02	1.29	0.04	3.01	76.81
Yalgoo	<b>YL18</b>	Polelle	54.79	0.45	10.42	10.37	0.15	14.19	7.33	0.15	2.08	0.05	2.99	75.07
Yalgoo	<b>YL2</b>	Polelle	56.30	0.63	12.51	9.81	0.14	9.72	7.70	1.29	1.82	0.07	2.32	68.55
Yalgoo	<b>YL5</b>	Polelle	55.71	0.48	10.24	10.20	0.17	14.11	7.58	0.36	1.10	0.05	3.31	75.28
Yalgoo	<b>YL6</b>	Polelle	55.53	0.50	10.55	9.95	0.17	14.29	7.21	0.71	1.02	0.06	3.49	75.97
Yalgoo	<b>YL7</b>	Polelle	56.14	0.60	12.50	9.73	0.16	9.67	8.12	0.85	2.15	0.07	1.90	68.62
Yalgoo	<b>YL8</b>	Polelle	55.76	0.61	12.50	9.51	0.15	9.59	8.56	1.22	2.01	0.07	1.67	68.94
Mulgine	<b>225052</b>	Polelle	51.66	0.53	13.49	11.20	0.18	7.93	13.59	0.04	1.34	0.04	0.50	60.92
Mulgine	<b>225051</b>	Polelle	50.31	0.54	14.04	11.67	0.21	9.02	12.53	0.07	1.57	0.04	0.52	62.96
Mulgine	<b>MG1</b>	Polelle	51.25	0.42	15.67	9.10	0.14	8.71	12.54	0.16	2.00	0.02	0.90	67.81
Mulgine	<b>MG11</b>	Polelle	52.84	0.44	13.71	10.66	0.18	9.86	10.41	0.06	1.81	0.03	0.54	67.06
Mulgine	<b>MG12</b>	Polelle	52.33	0.48	15.21	10.86	0.17	8.33	9.52	0.11	2.95	0.04	0.56	62.81
Mulgine	<b>MG14A</b>	Polelle	50.91	0.52	14.95	11.19	0.16	9.45	10.84	0.04	1.91	0.03	0.34	65.01

LOCATION	SAMPLE #	GROUP	SiO2	TiO2	Al2O3	Fe2O3	MnO	MgO	CaO	K2O	Na2O	P2O5	LOI	Mg#
Mulgine	<b>MG17</b>	Polelle	53.04	0.47	14.38	10.14	0.16	8.14	12.19	0.02	1.43	0.03	0.52	63.85
Mulgine	<b>MG18</b>	Polelle	54.21	0.60	14.59	10.02	0.15	7.07	10.49	0.09	2.74	0.04	0.50	60.83
Mulgine	<b>MG22</b>	Polelle	50.33	0.46	12.71	11.81	0.21	11.96	11.51	0.09	0.88	0.05	1.03	69.03
Mulgine	<b>MG24</b>	Polelle	50.92	0.43	13.17	11.01	0.19	12.03	10.11	0.09	2.04	0.02	0.87	70.64
Mulgine	<b>Mg26</b>	Polelle	53.28	0.54	14.30	10.54	0.17	7.26	12.99	0.04	0.82	0.05	0.58	60.28
Mulgine	<b>MG27</b>	Polelle	53.88	0.70	14.41	11.97	0.18	6.96	8.47	0.11	3.25	0.07	0.47	56.13
Mulgine	<b>MG29</b>	Polelle	52.13	0.61	14.92	11.24	0.19	7.71	9.93	0.11	3.11	0.04	0.69	60.15
Mulgine	<b>MG9</b>	Polelle	53.80	0.59	14.00	10.88	0.16	8.84	9.84	0.03	1.81	0.04	0.37	64.12
Warriedar	<b>FFE3</b>	Norie	43.75	0.24	2.55	14.79	0.25	36.72	1.60	0.07		0.03	9.98	84.53
Warriedar	<b>FFE2</b>	Norie	45.30	1.05	7.50	19.42	0.31	10.06	14.78	0.51	0.99	0.07	0.37	53.27
Warriedar	<b>FFE1</b>	Norie	47.78	0.72	4.90	15.89	0.27	17.18	12.95	0.05	0.20	0.05	3.88	70.41
Warriedar	<b>WR10</b>	Polelle	50.02	0.65	15.62	12.15	0.17	7.76	11.02	0.40	2.14	0.06	1.64	58.43
Warriedar	<b>WR11</b>	Polelle	55.69	0.66	6.31	12.05	0.20	11.49	11.34	0.23	1.95	0.07	1.29	67.73
Warriedar	<b>WR12</b>	Polelle	56.59	0.77	7.59	11.58	0.17	10.36	9.95	0.20	2.70	0.08	0.94	66.32
Warriedar	<b>WR15</b>	Norie	48.70	0.44	7.91	11.58	0.19	24.51	5.80	0.01	0.80	0.06	4.65	82.32
Warriedar	<b>WR16</b>	Norie	48.18	0.53	9.37	11.07	0.19	19.17	10.35	0.03	1.04	0.06	2.98	79.21
Warriedar	<b>WR17</b>	Polelle	50.81	0.90	8.99	13.97	0.30	10.09	12.38	0.33	2.16	0.08	0.69	61.39
Warriedar	<b>WR5</b>	Polelle	58.34	0.80	9.53	11.02	0.16	7.58	8.52	0.78	3.18	0.09	0.05	60.22
Warriedar	<b>WR8</b>	Polelle	51.76	1.04	9.61	14.56	0.31	8.60	11.02	0.79	2.20	0.11	0.57	56.51
Warriedar	<b>WR9</b>	Polelle	51.89	0.95	8.42	12.08	0.22	10.30	13.61	0.39	2.07	0.07	0.73	65.23
Yeoh Hills	<b>YH1</b>	Norie	52.33	0.77	10.18	12.20	0.19	12.05	10.44	0.06	1.70	0.07	0.58	68.49
Yeoh Hills	<b>YH10</b>	Norie	53.98	0.91	11.60	11.81	0.18	8.24	11.91	0.06	1.24	0.07	0.72	60.58
Yeoh Hills	<b>YH11</b>	Norie	54.55	0.91	11.83	11.58	0.18	8.09	11.22	0.06	1.49	0.08	0.55	60.58
Yeoh Hills	<b>YH14</b>	Norie	54.00	0.93	11.84	11.17	0.18	8.34	11.99	0.03	1.43	0.08	0.62	62.17
Yeoh Hills	<b>YH15</b>	Norie	50.17	1.38	13.72	12.34	0.23	7.25	12.29	0.26	2.25	0.11	0.60	56.39
Yeoh Hills	<b>YH19</b>	Norie	52.98	0.76	7.46	10.97	0.21	13.09	13.35	0.11	1.00	0.06	1.47	72.43

LOCATION	SAMPLE #	GROUP	SiO2	TiO2	Al2O3	Fe2O3	MnO	MgO	CaO	K2O	Na2O	P2O5	LOI	Mg#
Yeoh Hills	<b>YH20</b>	Norie	49.91	1.35	10.61	16.29	0.25	10.81	8.39	0.06	2.20	0.12	0.42	59.35
Yeoh Hills	<b>YH24</b>	Norie	52.73	1.59	13.46	13.67	0.19	6.13	9.39	0.11	2.57	0.15	0.33	49.68
Yeoh Hills	<b>YH25</b>	Norie	52.78	1.96	12.89	15.38	0.19	5.12	8.23	0.12	3.14	0.18	0.16	42.30
Yeoh Hills	<b>Yh3b</b>	Norie	51.46	1.00	10.73	12.66	0.19	9.87	12.46	0.04	1.51	0.08	0.57	63.19
Yeoh Hills	<b>YH5</b>	Norie	54.56	0.90	12.14	11.24	0.19	7.49	12.29	0.05	1.06	0.08	1.04	59.47

## Whole Rock Data: Trace Elements 1

LOCATION	SAMPLE #	GROUP	Nb	Zr	Hf	Th	U	Y	La	Ce	Pr	Nd	Sm	Eu
Yalgoo	<b>225150</b>	Polelle	5.26	97.05	2.73	5.17	0.68	25.27	18.50	35.28	3.97	15.57	3.51	0.96
Yalgoo	<b>225159</b>	Polelle	5.05	92.94	2.93	5.53	1.36	21.01	19.19	36.77	4.07	15.46	3.40	0.92
Yalgoo	<b>225152</b>	Polelle	2.55	47.83	1.38	2.83	0.49	10.20	8.40	15.84	1.90	7.12	1.58	0.37
Yalgoo	<b>225145</b>	Polelle	3.92	69.39	2.11	2.01	0.44	20.82	3.72	15.69	1.49	7.14	2.55	0.95
Yalgoo	<b>YL1</b>	Polelle	4.99	106.93	2.95	5.58	0.97	22.40	19.25	35.64	4.12	16.70	3.58	1.12
Yalgoo	<b>YL11</b>	Polelle	5.14	115.08	3.29	6.31	1.23	24.45	18.29	39.46	4.25	16.44	3.65	1.00
Yalgoo	<b>YL12</b>	Polelle	4.80	103.13	3.06	5.10	1.24	22.36	17.46	34.00	3.90	15.52	3.26	0.94
Yalgoo	<b>YL14</b>	Polelle	3.34	71.86	2.13	1.94	0.54	18.32	6.88	16.40	2.12	9.41	2.66	0.92
Yalgoo	<b>YL15</b>	Polelle	2.06	43.17	1.34	1.27	0.20	13.67	4.73	10.69	1.41	6.37	1.97	0.85
Yalgoo	<b>YL16</b>	Polelle	1.55	35.13	1.03	0.56	0.11	12.61	2.58	6.51	0.88	4.34	1.33	0.49
Yalgoo	<b>YL17</b>	Polelle	1.55	33.01	0.93	0.53	0.12	11.86	2.17	5.16	0.75	3.82	1.26	0.48
Yalgoo	<b>YL18</b>	Polelle	1.65	38.14	1.24	0.70	0.16	14.02	3.61	8.14	1.20	5.67	1.71	0.62
Yalgoo	<b>YL2</b>	Polelle	5.12	108.52	3.17	5.80	1.10	21.91	14.64	36.04	3.51	14.03	3.20	0.91
Yalgoo	<b>YL5</b>	Polelle	3.83	76.56	2.28	4.31	0.79	19.14	15.31	25.66	3.24	12.52	2.74	0.77
Yalgoo	<b>YL6</b>	Polelle	3.94	68.35	2.07	3.72	0.79	18.64	13.05	26.10	2.94	12.32	2.66	0.72
Yalgoo	<b>YL7</b>	Polelle	5.20	110.10	3.26	5.80	1.46	23.14	18.66	38.13	4.26	16.72	3.56	0.97
Yalgoo	<b>YL8</b>	Polelle	5.08	107.79	3.15	5.89	1.50	23.39	19.22	38.54	4.44	17.69	3.83	0.97
Mulgine	<b>225052</b>	Polelle	1.11	31.15	0.90	0.42	0.08	15.28	2.31	5.33	0.76	3.62	1.11	0.57
Mulgine	<b>225051</b>	Polelle	1.11	30.16	1.01	0.41	0.08	14.78	2.01	4.83	0.72	3.72	1.11	0.52
Mulgine	<b>MG1</b>	Polelle	1.21	27.24	0.71	0.49	0.10	14.23	3.73	5.75	0.91	4.14	1.19	0.57
Mulgine	<b>MG11</b>	Polelle	1.01	27.15	0.80	0.33	0.09	13.57	1.91	4.12	0.63	3.12	1.14	0.42
Mulgine	<b>MG12</b>	Polelle	1.11	30.17	0.80	0.35	0.09	13.27	2.21	4.12	0.65	3.32	1.02	0.47
Mulgine	<b>MG14A</b>	Polelle	1.10	30.10	0.90	0.37	0.10	15.25	2.31	4.82	0.70	3.41	1.22	0.44

LOCATION	SAMPLE #	GROUP	Nb	Zr	Hf	Th	U	Y	La	Ce	Pr	Nd	Sm	Eu
Mulgine	<b>MG17</b>	Polelle	1.01	27.14	0.80	0.38	0.10	13.67	2.41	5.23	0.68	3.32	1.03	0.45
Mulgine	<b>MG18</b>	Polelle	1.21	29.15	0.90	0.43	0.11	14.57	1.71	3.92	0.63	3.12	1.17	0.50
Mulgine	<b>MG22</b>	Polelle	0.91	30.31	0.91	0.34	0.08	13.44	1.92	4.45	0.64	3.13	1.16	0.44
Mulgine	<b>MG24</b>	Polelle	0.81	23.21	0.71	0.24	0.08	11.80	2.22	4.24	0.60	3.03	0.94	0.38
Mulgine	<b>Mg26</b>	Polelle	1.41	33.19	0.91	0.53	0.13	15.29	3.22	7.04	0.96	4.53	1.40	0.57
Mulgine	<b>MG27</b>	Polelle	1.71	39.19	1.21	0.66	0.14	18.49	4.12	8.04	1.25	6.03	1.67	0.55
Mulgine	<b>MG29</b>	Polelle	0.81	31.21	1.01	0.29	0.08	16.81	2.01	3.93	0.63	3.42	1.33	0.53
Mulgine	<b>MG9</b>	Polelle	1.30	35.13	1.00	0.46	0.12	16.06	3.01	6.12	0.86	4.22	1.30	0.51
Warriedar	<b>FFE3</b>	Norie	0.89	15.57	0.33	0.21		6.67	2.67	4.67	0.71	3.23	0.82	0.34
Warriedar	<b>FFE2</b>	Norie	3.31	61.23	1.81	0.42	0.10	17.06	4.72	12.55	2.18	11.04	3.28	1.03
Warriedar	<b>FFE1</b>	Norie	2.29	43.68	1.25	0.27	0.06	12.17	3.54	9.26	1.51	7.70	2.25	0.73
Warriedar	<b>WR10</b>	Polelle	1.53	33.55	0.92	0.27	0.07	17.08	4.27	8.03	1.22	5.80	1.71	0.72
Warriedar	<b>WR11</b>	Polelle	5.47	81.04	2.13	1.70	0.37	28.37	15.70	30.90	3.96	16.41	3.98	1.10
Warriedar	<b>WR12</b>	Polelle	6.76	99.94	2.62	2.06	0.45	30.18	13.93	28.67	3.81	16.35	3.89	1.20
Warriedar	<b>WR15</b>	Norie	1.68	37.72	0.94	0.82	0.22	10.69	4.51	9.22	1.14	5.03	1.37	0.49
Warriedar	<b>WR16</b>	Norie	1.65	40.19	1.03	0.48	0.13	15.25	3.50	7.21	1.08	5.05	1.51	0.55
Warriedar	<b>WR17</b>	Polelle	5.64	60.41	1.61	0.81	0.20	14.20	9.57	21.75	3.05	13.39	3.23	1.05
Warriedar	<b>WR5</b>	Polelle	8.10	133.07	3.50	2.92	0.79	32.92	19.01	39.92	4.73	19.01	4.50	1.19
Warriedar	<b>WR8</b>	Polelle	7.34	97.55	2.72	1.94	0.47	17.70	15.29	33.79	4.32	18.91	4.19	1.32
Warriedar	<b>WR9</b>	Polelle	5.04	55.41	1.71	0.76	0.18	15.31	7.96	19.24	2.80	13.20	3.25	1.20
Yeoh Hills	<b>YH1</b>	Norie	1.91	45.26	1.41	0.37	0.08	14.38	2.11	6.14	0.99	5.33	1.85	0.73
Yeoh Hills	<b>YH10</b>	Norie	2.42	58.42	1.71	0.58	0.15	18.03	3.93	9.97	1.45	7.55	2.38	0.89
Yeoh Hills	<b>YH11</b>	Norie	2.41	59.33	1.81	0.61	0.16	18.30	4.73	11.16	1.67	8.15	2.51	1.15
Yeoh Hills	<b>YH14</b>	Norie	2.42	62.39	1.91	0.67	0.14	18.52	5.13	11.17	1.73	8.76	2.57	0.78
Yeoh Hills	<b>YH15</b>	Norie	3.42	90.55	2.82	0.55	0.15	31.39	5.13	13.38	2.07	10.97	3.63	1.36
Yeoh Hills	<b>YH19</b>	Norie	1.73	40.59	1.22	0.37	0.09	14.41	2.94	7.51	1.15	5.99	1.87	0.68

LOCATION	SAMPLE #	GROUP	Nb	Zr	Hf	Th	U	Y	La	Ce	Pr	Nd	Sm	Eu
Yeoh Hills	<b>YH20</b>	Norie	4.12	98.42	2.81	0.66	0.16	22.50	6.33	16.77	2.47	12.45	3.74	1.57
Yeoh Hills	<b>YH24</b>	Norie	4.92	112.38	3.31	0.93	0.24	28.40	8.43	20.17	3.20	15.95	4.68	1.61
Yeoh Hills	<b>YH25</b>	Norie	5.81	135.22	3.91	1.06	0.24	30.85	7.41	19.73	3.22	16.33	4.90	1.70
Yeoh Hills	<b>Yh3b</b>	Norie	2.62	62.36	1.81	0.58	0.14	18.91	5.33	11.77	1.90	9.45	2.82	1.11
Yeoh Hills	<b>YH5</b>	Norie	2.53	62.64	1.82	0.65	0.16	19.90	4.55	11.01	1.65	8.18	2.65	1.30

## Whole Rock Data: Trace Elements 2

LOCATION	SAMPLE #	Ba	Sc	V	Cr	Ni	Ti	Gd	Tb	Dy	Ho	Er	Tm	Yb	Lu
Yalgoo	<b>225150</b>	369.00	29.32	199.16	606.57	180.96	4000.59	3.42	0.63	3.84	0.80	2.61	0.33	2.29	0.37
Yalgoo	<b>225159</b>	264.68	28.29	181.84	616.23	188.91	3694.81	3.62	0.59	3.64	0.76	2.46	0.32	2.27	0.37
Yalgoo	<b>225152</b>	315.71	17.01	106.30	2721.26	1365.95	1975.79	1.75	0.30	1.71	0.37	1.16	0.16	1.00	0.17
Yalgoo	<b>225145</b>	102.07	33.19	256.44	522.93	130.73	5909.03	3.27	0.56	3.61	0.73	2.20	0.29	1.95	0.32
Yalgoo	<b>YL1</b>	497.98	30.55	235.24	885.97	206.73	3724.59	3.55	0.63	3.88	0.84	2.31	0.36	2.18	0.34
Yalgoo	<b>YL11</b>	416.13	28.77	216.80	585.67	167.48	3819.58	4.05	0.69	4.11	0.88	2.64	0.40	2.50	0.39
Yalgoo	<b>YL12</b>	481.94	28.59	224.63	694.32	190.94	3856.93	3.49	0.61	3.85	0.81	2.40	0.38	2.32	0.38
Yalgoo	<b>YL14</b>	175.09	31.37	273.26	172.05	90.07	5157.88	3.03	0.53	3.41	0.74	1.96	0.32	2.04	0.29
Yalgoo	<b>YL15</b>	30.94	23.64	227.15	2199.53	335.07	3142.92	2.26	0.38	2.43	0.52	1.54	0.23	1.46	0.22
Yalgoo	<b>YL16</b>	96.92	26.86	216.98	2841.45	533.16	2354.17	1.79	0.33	2.14	0.49	1.34	0.22	1.39	0.22
Yalgoo	<b>YL17</b>	46.94	26.82	192.93	2703.02	482.83	2288.74	1.61	0.30	1.94	0.43	1.34	0.20	1.29	0.22
Yalgoo	<b>YL18</b>	150.49	30.92	214.40	1463.71	286.56	2719.36	2.23	0.36	2.55	0.57	1.66	0.26	1.66	0.27
Yalgoo	<b>YL2</b>	347.05	27.64	211.92	798.53	209.87	3744.32	3.43	0.58	3.86	0.80	2.35	0.36	2.29	0.34
Yalgoo	<b>YL5</b>	416.96	25.87	201.76	1655.43	322.81	2853.62	2.98	0.50	3.13	0.68	1.93	0.31	1.95	0.30
Yalgoo	<b>YL6</b>	320.02	26.93	208.17	1563.86	334.52	3042.74	2.89	0.48	3.07	0.64	1.88	0.31	1.93	0.29
Yalgoo	<b>YL7</b>	269.13	28.54	213.06	764.58	199.81	3606.28	3.74	0.63	3.99	0.85	2.42	0.40	2.39	0.38
Yalgoo	<b>YL8</b>	413.87	27.46	214.56	772.82	202.36	3658.18	3.89	0.67	4.19	0.91	2.54	0.40	2.41	0.40
Mulgine	<b>225052</b>	58.19	41.20	242.20	482.39	122.61	3193.58	1.80	0.32	2.31	0.52	1.60	0.24	1.50	0.24
Mulgine	<b>225051</b>	11.86	43.22	239.24	512.67	142.74	3254.66	1.78	0.33	2.35	0.54	1.56	0.23	1.55	0.24
Mulgine	<b>MG1</b>	106.95	33.30	198.76	141.25	83.74	2540.78	1.80	0.30	2.08	0.47	1.36	0.20	1.28	0.20
Mulgine	<b>MG11</b>	37.40	41.22	247.33	663.56	134.72	2652.40	1.54	0.31	2.23	0.54	1.56	0.25	1.70	0.27
Mulgine	<b>MG12</b>	165.91	44.24	263.45	442.43	93.51	2954.18	1.61	0.30	2.22	0.51	1.56	0.25	1.74	0.28
Mulgine	<b>MG14A</b>	16.76	46.15	260.87	521.75	96.32	3128.31	1.83	0.35	2.46	0.57	1.86	0.28	1.90	0.31

LOCATION	SAMPLE #	Ba	Sc	V	Cr	Ni	Ti	Gd	Tb	Dy	Ho	Er	Tm	Yb	Lu
Mulgine	<b>MG17</b>	26.24	44.23	241.27	442.32	88.46	2772.63	1.54	0.30	2.15	0.51	1.57	0.24	1.67	0.27
Mulgine	<b>MG18</b>	30.05	44.22	295.49	80.41	66.33	3555.44	1.74	0.34	2.36	0.55	1.77	0.27	1.91	0.31
Mulgine	<b>MG22</b>	184.38	36.37	340.47	838.54	216.20	2786.46	1.64	0.31	2.28	0.51	1.52	0.24	1.57	0.27
Mulgine	<b>MG24</b>	46.92	40.36	242.15	978.67	207.84	2540.75	1.44	0.26	1.89	0.45	1.40	0.19	1.48	0.22
Mulgine	<b>Mg26</b>	21.02	41.24	240.39	201.16	84.49	3256.57	1.92	0.35	2.44	0.56	1.81	0.25	1.82	0.29
Mulgine	<b>MG27</b>	159.76	41.20	274.30	30.14	55.26	4156.83	2.41	0.45	3.04	0.68	2.14	0.33	2.25	0.35
Mulgine	<b>MG29</b>	25.07	37.25	269.84	60.41	80.55	3682.55	2.10	0.41	2.86	0.64	1.91	0.27	1.86	0.30
Mulgine	<b>MG9</b>	16.76	40.15	261.97	291.08	105.39	3550.70	1.94	0.40	2.81	0.63	1.98	0.30	1.97	0.32
Warriedar	<b>FFE3</b>	74.42	10.01	78.98	4416.43	2313.90	1400.71	1.03	0.17	1.05	0.23	0.62	0.08	0.51	0.08
Warriedar	<b>FFE2</b>	42.16	31.12	276.03	170.63	244.91	6258.91	3.87	0.60	3.80	0.73	1.88	0.26	1.68	0.24
Warriedar	<b>FFE1</b>	38.48	23.92	175.75	1882.29	646.84	4364.68	2.68	0.44	2.60	0.50	1.32	0.18	1.08	0.17
Warriedar	<b>WR10</b>	91.81	35.59	292.82	325.35	163.69	3901.52	2.34	0.43	2.55	0.59	1.80	0.25	1.70	0.26
Warriedar	<b>WR11</b>	242.12	31.40	160.06	871.22	436.62	3948.09	4.30	0.76	4.45	0.99	3.09	0.46	3.00	0.49
Warriedar	<b>WR12</b>	101.46	26.25	163.54	1261.91	426.02	4600.24	4.31	0.75	4.39	1.02	3.20	0.46	3.27	0.49
Warriedar	<b>WR15</b>	57.95	24.10	176.05	3185.60	1330.83	2701.67	1.59	0.30	1.73	0.40	1.17	0.18	1.14	0.19
Warriedar	<b>WR16</b>	15.46	28.85	227.73	2576.14	846.01	3212.78	2.13	0.37	2.36	0.56	1.62	0.25	1.48	0.24
Warriedar	<b>WR17</b>	68.57	33.23	298.03	714.86	211.44	5493.56	3.03	0.46	2.78	0.54	1.45	0.23	1.40	0.21
Warriedar	<b>WR5</b>	570.28	22.01	166.08	680.34	247.12	4799.03	4.73	0.80	4.96	1.15	3.48	0.54	3.62	0.58
Warriedar	<b>WR8</b>	154.37	25.14	232.31	683.86	293.66	6271.04	4.04	0.58	3.54	0.71	1.95	0.27	1.69	0.27
Warriedar	<b>WR9</b>	216.60	44.33	308.28	362.68	188.39	5617.56	3.34	0.51	3.08	0.60	1.67	0.23	1.42	0.22
Yeoh Hills	<b>YH1</b>	18.11	36.21	306.78	1247.24	280.63	4583.41	2.42	0.40	2.67	0.55	1.58	0.24	1.41	0.23
Yeoh Hills	<b>YH10</b>	101.73	38.28	360.60	564.06	169.22	5435.39	2.98	0.51	3.26	0.68	1.93	0.28	1.70	0.28
Yeoh Hills	<b>YH11</b>	112.12	38.21	368.04	593.29	145.81	5426.34	3.16	0.54	3.44	0.68	1.90	0.29	1.78	0.27
Yeoh Hills	<b>YH14</b>	45.49	38.24	344.17	593.75	165.04	5490.82	3.32	0.54	3.34	0.71	2.00	0.29	1.83	0.27
Yeoh Hills	<b>YH15</b>	103.13	38.23	449.75	171.04	117.72	8144.04	4.69	0.85	5.53	1.19	3.41	0.56	3.41	0.54
Yeoh Hills	<b>YH19</b>	38.36	51.76	369.41	537.87	198.91	4563.64	2.46	0.40	2.61	0.53	1.47	0.22	1.31	0.22

LOCATION	SAMPLE #	Ba	Sc	V	Cr	Ni	Ti	Gd	Tb	Dy	Ho	Er	Tm	Yb	Lu
Yeoh Hills	<b>YH20</b>	24.40	32.14	413.77	843.61	286.23	7948.49	4.28	0.72	4.39	0.88	2.31	0.34	1.99	0.29
Yeoh Hills	<b>YH24</b>	262.88	32.11	401.35	80.27	81.27	9384.91	5.46	0.86	5.44	1.06	2.99	0.43	2.52	0.39
Yeoh Hills	<b>YH25</b>	56.29	33.05	454.74	20.03	59.10	11530.70	5.67	0.93	5.82	1.18	3.21	0.48	2.75	0.41
Yeoh Hills	<b>Yh3b</b>	53.21	37.21	368.12	804.63	180.04	5909.91	3.36	0.59	3.57	0.73	2.03	0.30	1.83	0.28
Yeoh Hills	<b>YH5</b>	231.38	37.38	381.92	596.12	138.42	5452.24	3.38	0.57	3.61	0.76	2.05	0.32	1.99	0.30

## Sample Locations

SAMPLE #	Latitude	Longitude		SAMPLE #	Latitude	Longitude		SAMPLE #	Latitude	Longitude
<b>225150</b>	-28.22293319	116.7113419		<b>MG17</b>	-29.14526981	116.9737992		<b>YH14</b>		
<b>225159</b>	-28.2223315	116.7130828		<b>MG18</b>	-29.14524567	116.9748815		<b>YH15</b>	-29.217503	117.262306
<b>225152</b>	-28.2228293	116.7114707		<b>MG22</b>	-29.14665685	116.9788299		<b>YH19</b>	-29.21483215	117.2653518
<b>225145</b>	-28.23520074	116.7351815		<b>MG24</b>	-29.14819162	116.9791253		<b>YH20</b>	-29.21468471	117.2655078
<b>YL1</b>	-28.30290263	116.7013819		<b>Mg26</b>	-29.14981054	116.9810176		<b>YH24</b>	-29.2125262	117.2671041
<b>YL11</b>	-28.30254958	116.7002362		<b>MG27</b>	-29.14991653	116.981449		<b>YH25</b>	-29.21207295	117.2673396
<b>YL12</b>	-28.302464	116.6999945		<b>MG29</b>	-29.15504923	116.9803074		<b>Yh3b</b>	-29.218679	117.261003
<b>YL14</b>	-28.25201144	116.7296466		<b>MG9</b>	-29.14371631	116.969078		<b>YH5</b>	-29.218263	117.261578
<b>YL15</b>	-28.25177616	116.7271934		<b>FEE3</b>						
<b>YL16</b>	-28.33181495	116.6733424		<b>FFE2</b>	-29.022291	117.309169				
<b>YL17</b>	-28.3311522	116.6729699		<b>FFE1</b>	-29.022383	117.308857				
<b>YL18</b>	-28.33311888	116.6744813		<b>WR10</b>	-29.07289862	117.1371285				
<b>YL2</b>	-28.30392882	116.7040221		<b>WR11</b>	-29.07248644	117.137481				
<b>YL5</b>	-28.30338098	116.7026941		<b>WR12</b>	-29.07237064	117.1376212				
<b>YL6</b>	-28.30327876	116.7025148		<b>WR15</b>	-29.06785648	117.1405316				
<b>YL7</b>	-28.30317898	116.701937		<b>WR16</b>	-29.07040969	117.1382747				
<b>YL8</b>	-28.30310203	116.7018072		<b>WR17</b>	-29.0760689	117.1349109				
<b>225052</b>	-29.14319487	117.020432		<b>WR5</b>	-29.07756109	117.1324269				
<b>225051</b>	-29.14374083	117.0208567		<b>WR8</b>	-29.07656679	117.1340903				
<b>MG1</b>	-29.11306587	116.9972835		<b>WR9</b>	-29.07606224	117.13479				
<b>MG11</b>	-29.14462286	116.970279		<b>YH1</b>	-29.218897	117.260551				
<b>MG12</b>	-29.14477608	116.9706109		<b>YH10</b>	-29.217386	117.26245				
<b>MG14A</b>	-29.14488156	116.9711113		<b>YH11</b>						

This Record is published in digital format (PDF) and is available as a free download from the DMIRS website at <[www.dmirs.wa.gov.au/GSWApublications](http://www.dmirs.wa.gov.au/GSWApublications)>.

Further details of geoscience products are available from:

Information Centre  
Department of Mines, Industry Regulation and Safety  
100 Plain Street  
EAST PERTH WESTERN AUSTRALIA 6004  
Phone: +61 8 9222 3459 Fax: +61 8 9222 3444  
[www.dmirs.wa.gov.au/GSWApublications](http://www.dmirs.wa.gov.au/GSWApublications)

